Journal of Advanced Materials and Processing

Islamic Azad University - Najafabad Branch

Journal of Advanced Materials and Processing

Vol.9, **No.3**, Summer 2021.

ISSN: 2322-388X

E-ISSN: 2345-4601

Publisher: Najafabad Branch, Islamic Azad University, Iron and Steel Association of Iran

Production manager: Mostafa Salehi

Executive assistant: Leily Rezaei, Seyedeh Razieh Anvari

Address: Journal of Advanced Materials and Processing

Department of Materials Engineering, Najafabad Branch, Islamic Azad University, Najafabad, Isfahan, Iran

P.O. Box: 517

Tel:+98-31-42292512 **Fax:**+98-31-42291008

Website: www.jmatpro.ir

Email:jmatpro@iaun.ac.ir

Table of Content

JMATPRO	Journal of Advanced Materials and Processing 9 (3): 3-14, Summer 2021 http://jmatpro.iaun.ac.ir 20.1001.1.2322388.2021.9.3.1.1

Research Paper

Delamination Detection in a Laminated Carbon Composite Plate Using Lamb Wave by Lead-Free Piezoceramic Transducers

Mohammad Hossein Ataei[1], Seyed Ali Hassanzadeh-Tabrizi[1*], Mahdi Rafiei[1], Ahmad Monshi[2]

1. Advanced Materials Research Center, Department of Materials Engineering, Najafabad Branch, Islamic Azad University, Najafabad, Iran.

2. Department of Materials Engineering, Isfahan University of Technology, Isfahan 84156-83111, Iran.

ARTICLE INFO

Article history:

Received 8 May 2021
Accepted 6 July 2021
Available online 1 August 2021

Keywords:
Lead-free Piezoceramic
Laminated carbon composite
Delamination detection
Lamb wave

ABSTRACT

The present study develops a semi-instantaneous baseline damage identification approach to identify the delamination damage. An active sensing network with $(Ba_{0.95}Ca_{0.05})(Ti_{0.91}Sn_{0.09})O_3$ (BCTS) lead-free piezoelectric transducers that were mounted on the two undamaged and damaged (with the delamination) plates. The wavelet transform was used for extracting the energy ratio change which is an effective and robust characteristic from the collected time-domain signals. The "identicality coefficient" (IC) was obtained for each sensing path under pristine structural conditions and used to eliminate any inequalities in the signals of each path. The output wave signals of samples were investigated by experiment and the finite element method. The values of the index produced by damages were significant against the threshold value set. The errors were less than 4%, which may be related to the linear relationship considered for the DI and delamination damage. A comparative of sensing paths showed a significant difference between both healthy and damaged samples. The delaminated damage was detected because the delamination phenomenon increased the amplitude of the wave and the wave energy. The comparison of the "damage index" (DI) values of six sensing paths showed that the path with delamination damage had the highest DI value i.e., 0.92 and then the sensing paths closest to the damage showed the highest DI values (DI=0.67). The path with a distance farther from the damage shows DI=0.09. The other DI values of other sensing paths were close to zero (DI=0) due to no damage.

Citation: Bakhtiari, L., Jafari, A., Sharafi, Sh., (2021) The Effect of Reverse Pulse Plating and Lanthanum Addition in Plating Bath on Corrosion Resistance of Austenitic Steel in Chlorine Solution, Journal of Advanced Materials and Processing, 9 (3), 3-14. Dor: 20.1001.1.2322388.2021.9.3.1.1

* **Corresponding Author**
E-mail address: hassanzadeh@pmt.iaun.ac.ir

1. Introduction

Composite materials have been widely used in many high-performance structures due to their high specific strength and stiffness coupled with cost-effectiveness over traditional materials. Internal damages such as microcracks and delaminations are generated; they can eventually cause catastrophic failures of structures during the service life. Delamination in composite structures plays a major role in lowering structural strength and stiffness, consequently downgrading system integrity and reliability. Therefore, composite structures are needed to be examined frequently. There is an increasing interest in SHM of composite structures as composite materials are widely used in structures. However, composite materials are susceptible to damages such as delamination and debonding. Such defects often occur beneath the surface of the composite structures, and they are hardly visible or detectable by the naked eyes. Further damage may also occur in composite laminates in the form of delaminations between plies of dissimilar properties. Such delaminations are promoted by the interfacial shear and normal stresses that appear in the "boundary layer" at the laminate edges and near internal cracks. Composite materials are vulnerable to damages, including debonding and delamination, due to accumulated fatigue loading or abrupt impact. Delaminations are areas of separation between the layers of a laminate composite or between the faces and the core of a composite sandwich. Disbonds are areas in which two adherends have separated at the bondline. Currently, non-destructive testing (NDT) is performed to detect such damages during inspections, and there are ongoing efforts to develop an online SHM, which can perform automated damage diagnosis during the normal operation. Structural health monitoring is evaluating and assuring the performance and safety of structures using sensor data. In the SHM process, an electric signal applied at the transmitter PWAS generates, through piezoelectric transduction, elastic waves that travel into the structure and are captured at the receiver PWAS. As long as the structural region between the transmitter and receiver is in pristine condition, the received signal will be consistently the same; if the structure becomes damaged, then the received signal will be modified. Comparative of the historically stored signals and the currently read signal will indicate when changes (e.g., damage) take place in the structure. There is an increasing need for a valid, cheap, and fast monitoring system to ensure the functionality and safety of a laminated composite structure. Ultrasonic guided waves, especially Lamb waves, because of their favorable features like low attenuation during propagation, propagating in curved panels, and large-distance traveling in a thin-plate structure, received a lot of attention as an efficient tool for damage identification like delaminations and cracks in composite and metallic structures [1-10]. Because damage identification results based on the Lamb waves propagation approach can be influenced by varying environmental and operational conditions, the development of a robust monitoring system with no need for the prior measured data of the structure has gained much attention recently. Many investigations have utilized the Lamb wave-based damage diagnosis for components with simple geometry like plates to successfully detect debonding and delamination [11-15]. Although ultrasonic guided wave attenuation in carbon-fiber-reinforced polymers is greater than metal alloys, many researchers widely study this method in composite materials [16-21]. Gumez et al. investigated the delamination damage detection in wind turbine blades using guided waves. They developed a new approach for disunity detection between layers comparing two real blades. Also, one of them was built with three disbonds introduced in its manufacturing process. The signals are denoised by Daubechies wavelet transform. The threshold for denoising is obtained by a wavelet coefficients selection rule using the Birgé-Massart penalization method. The signals were normalized, and their envelopes were obtained by Hilbert transform. Finally, pattern recognition based on correlations was applied. Damaged and undamaged blades were compared. The three induced disbonds in the "damaged blade" were clearly found [16]. The signals were normalized, Hilbert transform was used to obtain their envelopes, and pattern recognition was applied based on the correlations. A new technique for damage detection was proposed by Yeum et al. [18]. They detected the delamination in composite plates by comparing pitch-catch Lamb wave signals of a piezoelectric transducer (PZT) network without using their baseline signals from the pristine conditions [18]. It was on the basis of the fact that while the fundamental antisymmetric (A0) mode passes through a delamination area, its speed slows down. On the other hand, delamination slightly affects the fundamental symmetric mode (S0). The A_0 modes' relative time delays are instantly compared. Therefore, intense delamination detection is obtained at different temperatures. Kang et al. [22] showed that by using the PZTs, which are embedded in a composite plate, Lamb waves could be generated and used for health monitoring applications. A Lamb wave-based identification method was established to delaminate in vacuum-assisted resin transfer molding (VARTM) composite structures. The finite element method (FEM) experiment was used to propagate Lamb waves in composite plates. The study assessed damage in the plates by fusing information from multiple sensing paths of the embedded network. To eliminate interference, a wavelet transform technique was applied to purify the acquired Lamb wave

signals. The results showed that satisfactory detection of defects could be achieved with the proposed method. Ng et al. [23] for checking the carbon fiber reinforced polymer (CFRP) retrofitted concrete structures debonding, proposed transducers network by sequentially receiving and actuating nonlinear Rayleigh wave. The second harmonic generation nonlinear property was used for debonding due to the Rayleigh wave interaction at the debonding between the concrete interfaces and CFRP. The ultrasonic guided wave propagation technique as a promising method of damage detection utilizes guided waves in the damage detection by the analysis of differences among the signals recorded from sensing paths as baseline data when the structures are in their pristine conditions with no damage. The variations in operational and environmental parameters are a crucial concern with the methods using pristine baseline data, which can make a difference in the structure's currently collected response with that of measured baseline data. Furthermore, the detection of any possible existing initial defect is not possible before installing the sensor. To solve these drawbacks, some techniques have been tried to be developed, which do not require the use of pristine baseline data, such as the time-reversal method. Sohn developed some progress in in-service monitoring of aerospace, automotive, civil, and mechanical systems, which are subject to various operational and environmental. He developed effects of environmental and operational variability on structural health monitoring [24]. A. Marzani, S. Salamo presented a numerical prediction and experimental verification of temperature effect on plate waves generated and received by piezoceramic sensors. This work proposes a numerical approach based on a Semi-Analytical Finite Element (SAFE) model to predict temperature effects on guided waves generated and received by low-profile piezoceramic (PZT) transducers. The proposed model includes the cumulative role of transducer elements (actuator and sensor), substrate structure, and transducer/structure interaction in predicting the full pitch-catch guided wave response under changing temperature. Also, it was presented a novel physics-based temperature compensation model for structural health monitoring using ultrasonic guided waves [25,26]. An analytical and experimental investigation of the Lamb wave-mode tuning with piezoelectric wafer active sensors (PWASs) is presented by G. B. Santoni et al.. The analytical investigation assumes a PWAS transducer bonded to the upper surface of an isotropic flat plate. The PWAS Lamb wave tuning technique described in this paper is used to resolve the side packets problem. Several tuning cases are illustrated [27]. A reference-free scheme was proposed by Kim and Sohn. The proposed NDT technique utilizes the polarization characteristics of the piezoelectric wafers attached on both sides of the thin metal structure. Crack formation creates Lamb wave mode conversion due to a sudden change in the thickness of the structure. Then, the proposed technique instantly detects the appearance of the crack by extracting this mode conversion from the measured Lamb waves, and the threshold value from damage classification is also obtained only from the current dataset [28]. Alem and Abedian proposed a semi-instantaneous baseline approach to detect damage using a guided wave propagation technique with an embedded PZT wafer active sensor [29]. In this method, its introduced IC was obtained and used for all sensing paths in structures' pristine conditions to eliminate any inequalities in the signals of each path. The technique was according to the assumption that the S_0 of Lamb waves is attenuated by passing through the crack damage. The damage was detected on a sample lap joint structure by an active sensing network. FEM is used for wave propagation simulation by the wavelet transform to calculate DI values.

The main idea and novelty of the present study is developing a semi instantaneous baseline damage identification to identify the delamination damage in a laminated carbon composite plate. Because damage identification results based on the Lamb waves propagation approach can be influenced by varying environmental and operational conditions, developing a robust monitoring system with no need for the prior measured data of the structure has gained much attention recently. The instantaneous baseline damage detection technique is one of the promising methods that overcome the mentioned obstacles. This method was proposed by Alem and Abedian that used to detect and characterize fatigue cracks that initiate around the rivet holes of lap joint metal structures [29]. The authors developed a semi-baseline damage identification approach for detecting delamination damage for the first time. The obtained results show that this method can detect delamination. The output wave signals, IC, and DI values of each sensing path for healthy and damaged samples were investigated and evaluated by experimental and FEM.

Another novelty and merit of the study is that for the first time, an active sensing network of lead-free BCTS or $(Ba_{1-x}Ca_x)(Ti_{1-y}Sn_y)O_3$ (designed and manufactured by the same authors) was used to damage detection instead of PZT transducers. In order to detect the delamination damage in laminated composite structures by the method of sending and receiving propagated wave with a high piezoelectric sensors coefficient (d_{33}), a lead-free piezo ceramic $(Ba_{1-x}Ca_x)(Ti_{1-y}Sn_y)O_3$ with high piezoelectric coefficients (d_{33}=752 pC/N) and the corresponding planar electromechanical coupling factor (kp=54.2%)

and inversed piezoelectric coefficient (dS/dE=1248 pm/V) [30]. Also, due to the toxicity of lead, environmental concerns and limitations, there is an immediate demand for lead-free alternatives to PZT transducers and sensors.

2. Experimental

2.1. Materials and Specimen preparation

Two undamaged and damaged laminated composite plate samples containing four layers prepreg woven carbon/epoxy (Japan Toray 100% quality carbon fiber sheet T300) with plies angles "0/90, ±45, Teflon, ±45, 0/90", shaped at 0.001 in×7.36 in×7.36 in, were prepared as experimental specimens. Fig. 1 shows a schematic of the dimension and geometrical information of the samples. In the delaminated region, a thin Teflon tape was used to separate two delamination surfaces in the delamination region with the individual lamina distance. Also, Fig. 2 shows a laminated carbon composite plate with delamination damage. Table 1 shows the mechanical properties of the specimen. Also, the sensors used in this study were BCTS, whose properties are given in Table 2. These designed and manufactured transducer sensors were used for the first time on a composite plate for damage detection [30]. An arrangement of four BCTS transducer sensors was used for the active sensing network, as illustrated in Fig. 3. In order to bond the sensors to the specimens' surface, a conductive silver epoxy adhesive (CW2400) was utilized.

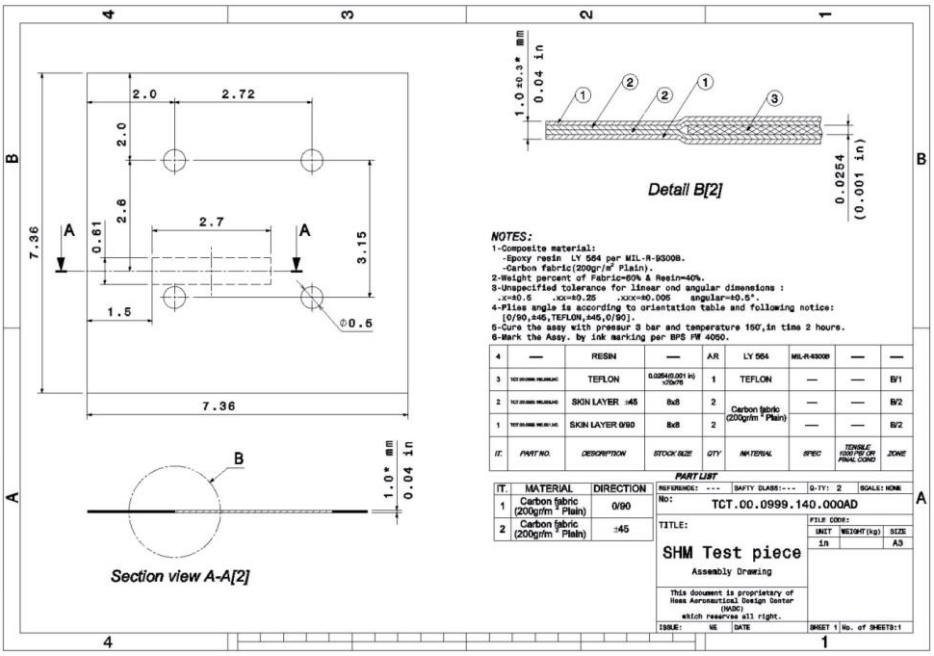

Fig. 1. Schematic of dimension and geometrical information of the samples.

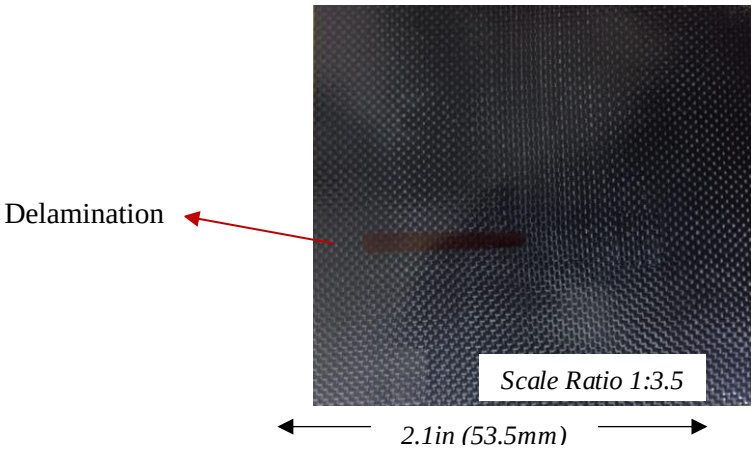

Fig. 2. Laminated carbon composite with delamination damage.

Table 1. Material properties of the specimen [30]

Material	E_{11}(Gpa)	E_{22}(Gpa)	E_{33}(Gpa)	υ_{12}	υ_{13}	υ_{23}	G_{12}(Gpa)	G_{13}(Gpa)	G_{23} (Gpa)	$\rho(kg/m^3)$
	55	55	8.265	0.06	0.437	0.437	4.0	2.407	2.407	**1605**

Table 2. Properties of piezoelectric sensor [30]

Piezoceramic	*tgδ*	*d33 (PC/N)*	*E*	f_r *(hz)*	f_a *(hz)*	K_p *(%)*
$(Ba_{0.95}Ca_{0.05})(Ti_{0.91}Sn_{0.09})O_3$	0.027	752	8100	151200	179990	**54.2**

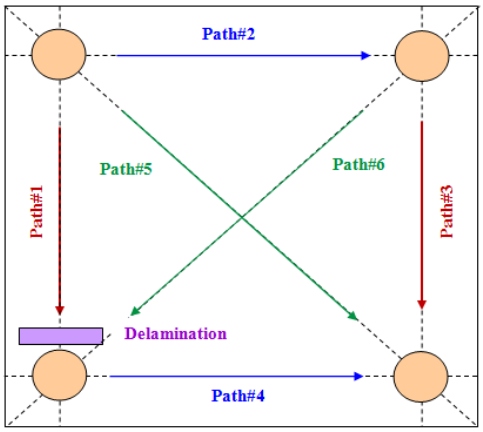

Fig. 3. Model description of delamination with the proposed actuator–sensor arrangement

2.2. Experimental and numerical setup - Model description

The transducers' wave propagation sensing paths and their deployment scheme on the structure are the same as the test model (Fig. 3). The function generator (RIGOL DG1022) generated a 250kHz and 4cycle burst-sine ultrasonic signal with a 10-V peak-to-peak amplitude and was applied to the BCTS actuators for exciting the structure. A digital oscilloscope collected signals from the sensing Paths 1 to 6 sensors. Fig. 4 shows the experimental setup. In this research, the lamb waves propagation in a square carbon/epoxy was laminated composite plate simulated numerically using the full 3D FEM models and dynamic explicit time-step analyzing ability of the ABAQUS software. The explicit solver can make a better trade-off between computational time and accuracy. In the dynamic time-step analysis, the accuracy and stability of the numerical solution are highly dependant on the spatial and temporal resolution of the analysis. In many investigations, a minimum of twenty points/wave cycles at the highest frequency is set for a time-step resolution. The size of the element is limited to 10% of the wavelength propagated in the structure for obtaining spatial accuracy. Three elements are considered through the thickness of each layer of the plate. The BCTS actuators and composite plate were simulated using an 8-node standard solid element C3D8R with 3 degrees of freedom/node from the ABAQUS element library. The layers were attached by defining the 'tie' constraint between the nodes at the interface of two adjacent layers. Two lower surfaces of BCTS actuators were also attached to the upper surface of the composite plate by 'tie' constraint in ABAQUS/explicit.

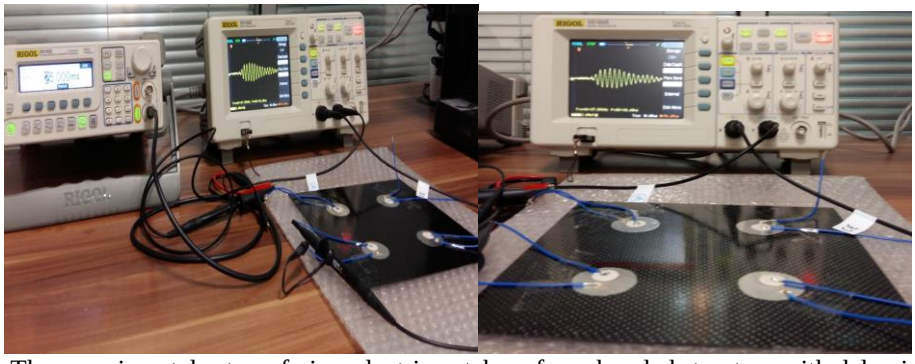

Fig. 4. The experimental setup of piezoelectric patch surfaces bonded structure with delamination.

Several works using conventional FEM have simulated the propagation of Lamb waves in structural components [29,31-37]. The studies have shown that a good discretization through the sample thickness (> 3 or 4 layers of elements) is needed to obtain precise results from simulating the A_0 mode. The explicit solver makes better trade-offs between computational time and accuracy. To accurately simulate the wave propagation, the model was meshed by 8-node 3D brick with 12 elements, with 4 element layers through the plate thickness (3 elements for each layer). At least 10 main nodes were assigned at the Lamb wavelength to show the validity of each simulated dynamic response. A surface contact algorithm [15] was introduced for processing the contact problem caused by delamination. By an element-based deformable surface, both the lower and upper delamination surfaces were defined. This surface allows the 2 surfaces to interact in a normal direction but resisting mutual penetration. The specifications of the simulated transducers, which were designed and built by the same authors, can be found in their most recent article.

Considering the piezo element's elastic effect, the piezoelectric sensor modeling attached to the structure leads to a more realistic simulation. The lower BCTS surface was attached to the composite plate by the tie constraint in ABAQUS. In addition, 2 connected regions were set as equal. In the tie constraint, the sensor surface and the actuator transducer surface were considered as the slave and master regions, respectively. The recorded signals from all sensing paths were compared between the experiment and the FEM simulation. For example, in Fig. 5, sensing path#3 is compared between the FEM and the experiment. As shown in Fig. 5, a great agreement can be seen for the S_0 mode used in detecting damages. Slight differences in amplitude and phase may be due to the adhesive bonding. S_0 mode at a relatively high frequency was used for the detection of the delamination damage. As seen in Fig. 5, the antisymmetric part of the signal recorded in the experiment is different from that of the FEM simulation. Therefore, this simulation could only help to design the structural health monitoring asset when only the first symmetric mode of the received signal is used for damage identification.

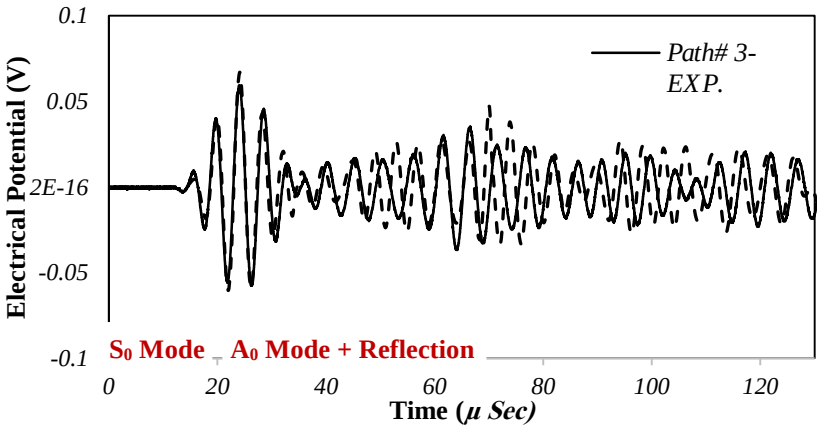

Fig. 5. Comparison of the recorded signals from sensing path#3 between the experiment and FEM at fc=250 kHz

2.3. Frequency selection

The excitation signal frequency should be correctly chosen to detect damages more precisely. The frequency selection range is completely liberal when one deals with the damages characterized by contact nonlinearity such as delamination. The number and frequency of the signals' cycles were calculated based on the output antisymmetric and symmetric signals. This calculation is dependant on the distance between the sensor and actuator transducers and the velocity of antisymmetric and symmetric waves or waves' time flight. The reason is that the contact nonlinearity arises due to relatively large stiffness alterations at the contact interfaces. The authors did five experiments at different frequencies (50-300 kHz) that the fewer Lamb wave modes are excited in the structure. Besides, a 4-cycle Hanning sinusoidal burst excitation wave with 10V amplitude and 250kHz central frequency was selected for the actuator signal.

2.4. Evaluating delamination procedure

The instantaneous baseline damage detection technique requires no pre-recorded data from the pristine structure [38]. It is because the signals recorded from 2 similar or equal paths are the same in the absence of defects near sensing paths. The damage parameters e.g., size, depth, and location of the defect, were extracted by determining the differences between the signals recorded along 2 equal sensing paths with/without damages. In general, signal measurement features response, including phase shift and attenuation, can be utilized to extract damage data of the inspected system due to discontinuities [6]. The output signal feature of similar sensing paths is identical about a simple structure, in the pristine state or health condition.

However, due to the waves reflected from structure edges and material orientation properties in composite and complex structures, their sensing signals are not the same even if equal lengths are considered for all similar sensing paths. Therefore, this study examined the semi-instantaneous baseline damage detection method for damage identification in composite structures [30]. An IC was defined for each of the paths. The "ICi" of the ith sensing path in the pristine conditions is the ratio of the minimum or maximum value of the signal feature content in all paths to the value of the signal energy content in the desired path. The selection of maximum and minimum will be explained in the following. Continuous wavelet transform CWT is a popular signal processing tool to identify the various features of dispersive guided wave signals [9,32,39-41]. The CWT of a guided wave signal is a transformation, which decomposes every such wave into a superposition of both translation and scale of a mother wavelet function ψ(t) given by

$$\psi_{a,\tau}(t) = |a|^{\frac{-1}{2}}\psi\left(\frac{t-\tau}{a}\right) \quad (1)$$

In the above-mentioned equation, the scaling parameter "a" controls the wavelet frequency bandwidth, and the translation parameter "τ" shifts the wavelet in time. The CWT of a time-domain guided wave signal "S(t)" is defined as follows:

$$W_{\psi}(a,\tau) = \frac{1}{\sqrt{a}}\int_{-\infty}^{\infty} s(t)\,\psi^{*}\left(\frac{t-\tau}{a}\right)d(t) \quad (2)$$

where ψ* is the complex conjugate of ψ. The wavelet energy spectrum "Ei(t, f)" for the ith path is:

$$E_i(t,f) = |W_i(t,f)|^2 \quad (3)$$

"Wi(t,f)" is the scalogram related to the ith sensing path. Therefore, the value of feature content (the energy index of each path or the wavelet energy value) related to the ith sensing path "Fi" is defined as

$$F_i = \int_{t_i}^{t_e} E_i\,(t,f^{*})d_t \quad (4)$$

In equation 4, t_e and t_i are the end and initial times of the windowed segment of the signal received, and f* is the frequency or scale where the absolute value of the CWT coefficients ǀWi(t, f)ǀ is maximized [29].

The semi-instantaneous method used here is based on the fact that each sensing feature must be normalized to the healthiest sensing path by the identical coefficient calculated in pristine conditions. For delamination defects, the feature content value of the output signal recorded from a path with delamination through that is higher than from the same path with no damage. This phenomenon will be shown in the result section by comparing the output waveform, output signal recorded from a path in health and damaged condition. This is because, in a composite structure such as a composite plate, the transducers are attached to the upper layer. When a Lamb wave is excited in the structure by the actuator transducer, the wave propagated in the structure through the laminate, attaching the transducer and other lower laminates by transferring the wave energy through the interference between the layers. Therefore, when there is a delamination defect between the layers, lower wave energy transfers to the lower layers. S0, the wave energy content value recorded from sensing the damaged path, contains a delamination defect trough that is higher than that of without delamination. However, the defects such as fatigue cracks cause a discontinuity in structure, and the wave amplitude is decreased when it passes through the fatigue cracks like to the cut trough damages. Therefore, an IC is defined for each path. The IC of each sensing path is equal to the ratio of the highest amount of the signal energy of all paths to the amount of signal energy of the desired path [29] to identify the fatigue cracks in metallic lap-joint structures. In this research, because of the identification of the delamination defects, the "IC_i" of the ith sensing path is as follows:

$$IC_i = \frac{F_{Min}^{P}}{F_i^{P}} \quad (5)$$

where "F_i^{P}" is the value of the wavelet energy content of the ith sensing path in pristine condition and "F_{Min}^{P}" is the minimum value of the wavelet energy content of the signals present in all the existing sensing paths. Then, by multiplying the value of the current energy content "F_i^{C}" of the ith sensing path "F_i^{C}" and its "IC_i" , the value of adjusted energy feature "F_i^{ad}" of the sensing path at the current measurement condition is obtained by F_i^{ad}

$$F_i^{ad} = IC_i \times F_i^{C} \quad (6)$$

This *IC* eliminates the effect of differences in path length and other factors that affect path energy. When there is no damage to the sensing paths, the values of adjusted energy in all sensing paths are identical at any current measurement data. The "DI_i" of the ith sensing path is as follows:

$$DI_i = \left|\frac{F_{Min}^{ad} - F_i^{ad}}{F_{Min}^{ad}}\right| \quad (7)$$

where "F_{Min}^{ad}" is the minimum value in the adjusted energy of all sensing paths.

There is no need to refer to the collected pristine data in future detection procedures due to the difference between this method and baseline methods. S_0, operational and environmental conditions can not affect the results of damage detection. In addition, IC is used to remove errors due to some uncertainties like plate thickness alterations, dimension inaccuracy during assembly and manufacturing procedures, embedded sensor dislocation, orientation layer, and laying up the process in the damage detection results. Even when the structure is in good condition, these

inaccuracies or uncertainties lead to differences in the sensing signals of similar paths. Thus, if IC is not used, the instantaneous baseline damage index may falsely show some damage in undamaged structures, or one may have to set high threshold values for the indices. In this algorithm, it is assumed that there is more than one healthy sensing path among all similar or equal sensing paths for the designed actuator-sensor arrangement. So, it can detect various damaged paths.

3. Results and discussion

3.1. Delamination detection by comparing the output signal of the sensing paths

In this study, the method for identifying semi-instantaneous baseline damage was developed and modified. Experimental tests were conducted to investigate the recorded signal and delamination damage detection. A 250kHz frequency excitation wave was chosen as an exciting wave in the composite plate structure because it provides good separation between the "A_0" and "S_0" modes in all sensing paths. The received signal represents the baseline signal, and shows the response time signal when delamination is within a direct line of the actuator and sensor path. The response signal is composed of several wave modes owing to wave scattering at the boundaries. In Fig. 5, the first mode, which looks like a sine wave modulated by a cosine function, is the first arrival of the A_0 mode associated with the direct path of the wave propagation. The second mode is another A_0 mode that is reflected from the edge of the plate. The observation of Fig. 5 clearly reveals that the first A_0 mode is the most sensitive to delamination damage. Based on these observations, a damage index is defined as the function of a signal's attenuation at a limited time span (a signal portion corresponding to the first A_0 mode) and at a specific frequency (the input frequency of the signal). Considering the necessary conditions that enforce the application of "IC" to the DI of similar sensing paths (i.e., symmetry in placing, geometry, and materials), the collected data for path#2 should be identical to the signals obtained from path#4. In fact, paths 2 and 4 are mirror symmetries of each other, without any damage .The corresponding wave packet consists of the first symmetric mode (S_0), the first antisymmetric mode (A_0), and the reflected wave from the boundaries. The ICs for all sensing paths (i.e., paths 1 to 6 as described in Fig. 3) are obtained. S_0 mode at relatively high frequency was used for the detection of the delamination damage.

Fig. 6 a and b compares the recorded signal of the sensing path#1 and #3, respectively, for two samples (one without any damage and the other having a peeling defect in thought path#1 as shown in Fig. 1). Results of Fig. 6a illustrate that the amplitude of the output recorded signal will be increased due to the existence of delamination defects in sensing path#1. Also, there is no difference in the amplitude of the output recorded signal in sensing path#3 for two samples.

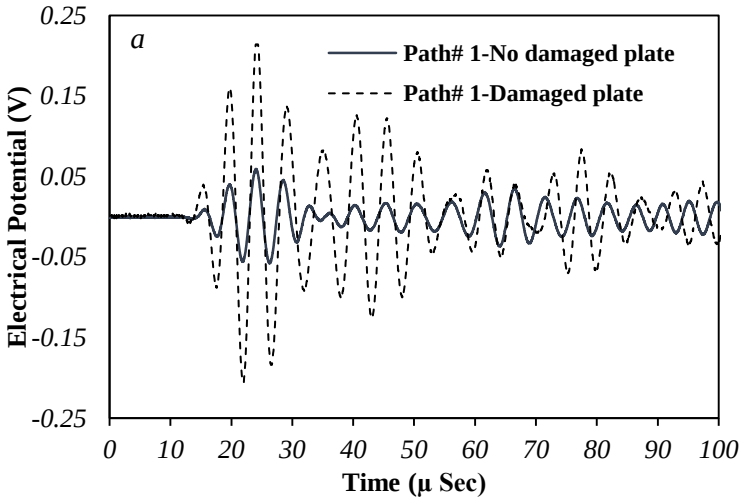

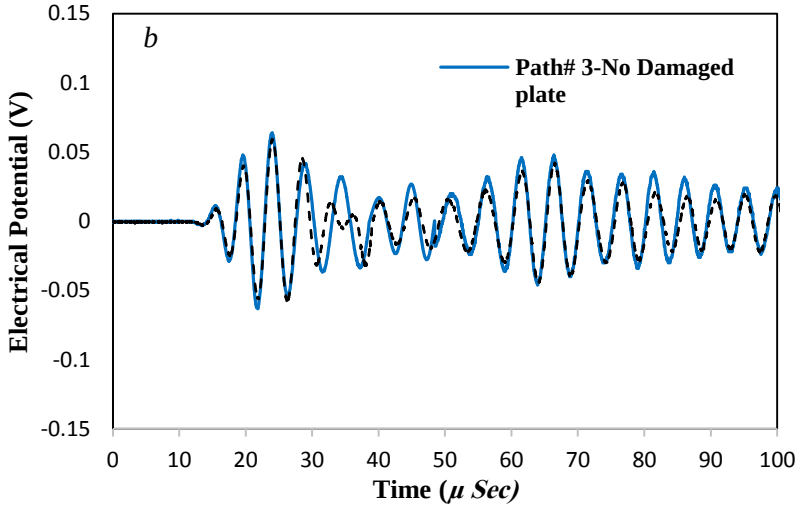

Fig. 6. Comparing the recorded signal of (a) sensing path #1, and (b) sensing path #3 for two un-damaged and damaged composite plate samples.

3.2. Sensing paths ICs

The ICs can eliminate the effect of uncertainty that occurred during production and measurement processes such as geometry, variable thickness, layer arrangement, plies angle, manufacturing, and installation condition. The IC is obtained for all sensing paths in the pristine condition of undamaged samples and reflects the relationship between the signals of the structure used to eliminate any present inequalities in each path. The proposed ICs modify the DI values for all sensing paths to remove the errors due to reflections from structural components and boundaries. ICs are only needed to be calculated once at the design stage of the SHM system. These coefficients that reflect the relationship between the paths are different from the recorded baseline data and are obtained when the structure is in its pristine condition. The ICs for all sensing paths in the pristine condition of the structure is obtained and utilized to eliminate the inequalities that occurred in the signals of each path. In this study, for delamination damage detection in the laminated composite plate, there are three groups of equal sensing paths: group paths 1 (paths#1 and #3), group paths 2 (paths#2 and #4), and group paths 3 (paths#5 and #6). Fig. 7 shows the ICs of all six sensing paths, calculated by the experimental output results of two samples. The standard deviation of ICs difference between paths #1 and #3 in group paths 1, path#2, and #4 in group paths 2, and path#5 and #6 in group paths 3, are 0.004, 0.005, and 0.005, respectively. These differences refer to measurement, equipment, manufacturing errors, etc. The ICs differences between group paths 1, group paths 2, and group paths 3, are due to differences in the length of the measurement paths.

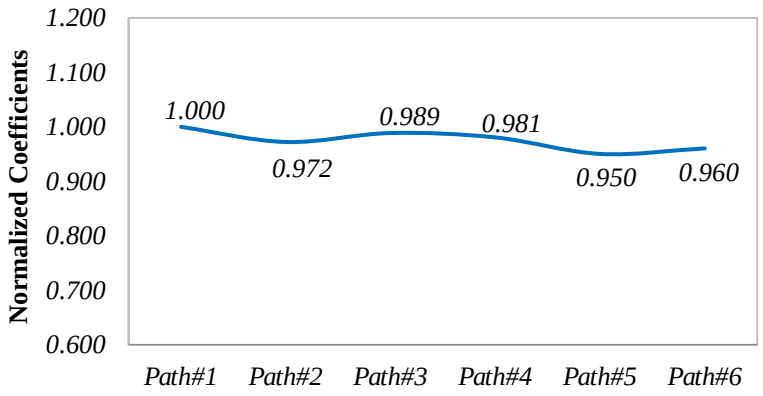

Fig. 7. IC values of Sensing Paths 1 to 6.

3.3. DI values

Fig. 8 shows the DI for six sensing paths. The path with damage (path#1) is identified by its higher index value. Higher threshold values are required because of the presence of some noise signals from the environmental impacts and measuring tools. Here a threshold value of 0.04 is sufficient. So, the values of the index produced by damages were significant against the threshold value set. The errors were less than 4%, which may be related to the linear relationship considered for the DI and delamination damage (Fig. 8). Recognition of the damaged path is difficult, with very low values of DI [29]. However, baseline-free methods play a significant role in removing such drawbacks as noise signals from the manufacturing process, measuring tools, etc. Therefore, with the proposed damage technique, several damaged paths can also be detected if there is a path without any damage. The output wave signals for damaged and undamaged samples (with delamination damage in path#1) were investigated by the experiment. Comparison of the results of recorded signals from sensing path for two healthy and damaged samples using two experimental and FEM analysis methods shows a significant difference between two samples in path#1 (the path with delamination damage). Also, it was not observed any notable difference in path#3 between undamaged and damaged samples. So, the damage was identified, and the performance of the lead-free piezoelectric sensors was verified. The delaminated damage was detected because the delamination phenomenon increased the amplitude of the wave and the wave energy.

A comparison of the DI values for six sensing paths based on the semi instantaneous baseline method shows that path#1 has the highest DI=0.92. In addition, DI of path#4 due to closeness to delamination damage is DI=0.67. Path#6 with a distance farther from the damage shows DI=0.09. Other sensing paths i.e. path#2, #3 and #5 with DI are close to zero due to no damage (Fig. 8).

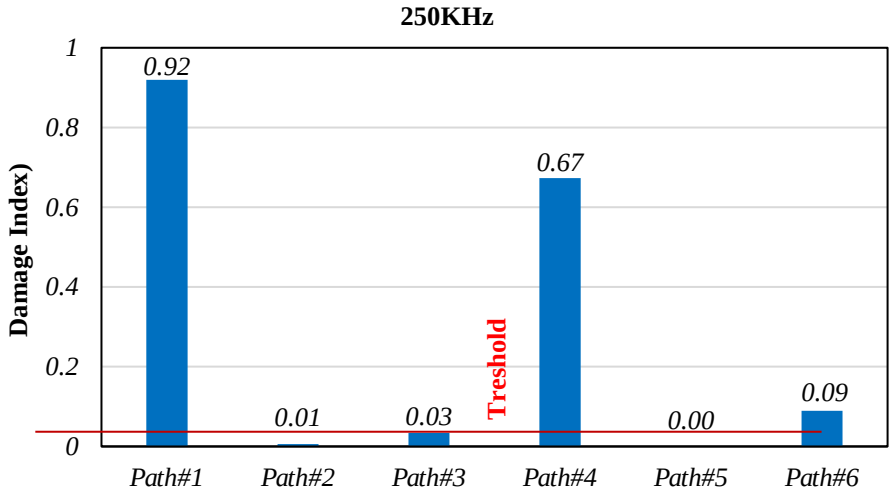

Fig. 8. DI values of Sensing Paths#1 to #6

4. Conclusions

In this paper, a semi-instantaneous baseline algorithm based on the wave propagation technique was developed in a carbon composite plate containing delamination damage by using an active sensing network with four (BCTS) lead-free piezoelectric transducers. The electrical signals' excitation forces applied to the piezoelectric actuators were calculated and entered into the model. The Lamb wave was created by imposing force profiles with time change to the actuator transducer nodes. The IC is obtained for all sensing paths in the pristine condition of undamaged samples and reflects the relationship between the signals of the structure used to eliminate any present inequalities in each path. The proposed ICs modify the DI values for all sensing paths to remove errors due to structural components and boundaries reflections. This can also reduce the uncertainty caused in manufacturing and assembly processes, that is, geometrical asymmetries and length differences in sensing paths. ICs are only needed to be calculated once at the design stage of the SHM system. These coefficients that reflect the relationship between the paths are different from the recorded baseline data and are obtained when the structure is in its pristine condition. The values of the index produced by damages were significant against the threshold value set. The errors were less than 4%, which may be related to the linear relationship considered for the DI and delamination damage. The output wave signals of samples were investigated by experiment and FEM (using Abaqus software). A comparison of the results of recorded signals from sensing paths shows a significant difference between the two healthy and damaged samples. The delaminated damage was detected because the

delamination phenomenon increased the amplitude of the wave and the wave energy. S_0 mode at a relatively high frequency was used for the detection of the delamination damage. A comparison of the DI values of six sensing paths shows that the path with delamination damage (path#1) has the highest DI value i.e., 0.92 and then the sensing paths closest to the damage show the highest DI values. The DI values of other sensing paths are close to zero due to no damage. So, the damage was identified, and the performance of the BCTS sensors was verified.

Data Availability

All data, models, and code generated or used during the study appear in the submitted article.

References

[1] D. Alleyne, P. Cawley, "A two-dimensional Fourier transform method for the measurement of propagating multi mode signals", Acoust. Soc. Am. J., Vol. 89, 1991, pp. 1159-1168.

[2] Clarke TF. Simonetti, P. Cawley, "Guided wave health monitoring of complex structures by sparse array systems: Influence of temperature changes on performance", Sound Vib. J., Vol. 329, 2010, pp. 2306-2322.

[3]] K. Diamanti, J. Hodgkinson, C. Soutis, "Detection of Low-velocity Impact Damage in Composite Plates using Lamb Waves", Struct. Health Monit. J., Vol. 3, 2004, pp. 33-41.

[4] V. Giurgiutiu, "Tuned Lamb Wave Excitation and Detection with Piezoelectric Wafer Active Sensors for Structural Health Monitoring", Intell. Mater. Syst. Struct. J., Vol. 16, 2005, pp. 291-305.

[5] H. W. Park, H. Sohn, "Time reversal active sensing for health monitoring of a composite plate", Sound Vib. J., Vol. 302, 2007, pp. 50-66.

[6] A. Raghavan, C. E. Cesnik, "Review of Guided-Wave Structural Health Monitoring", Shock Vibr. J., Vol. 39, 2007, pp. 91-114.

[7] P. Rizzo, E. Sorrivi, F. Lanza di Scalea, E. Viola, "Wavelet-based outlier analysis for guided wave structural monitoring: Application to multi-wire strands", Sound Vib. J., Vol. 307, 2007, pp. 52-68.

[8] Z. Su, X. Wang, Z. Chen, L. Ye, D. Wang, "A built-in active sensor network for health monitoring of composite structures", Smart Mater. Struct. J., Vol. 15, 2006, pp. 1939-1947.

[9] G. Yan, "A Bayesian approach for damage localization in plate-like structures using Lamb waves", Smart Mater. Struct. J., Vol. 22, 2013, pp. 12-35.

[10] H. Sohn, H. W. Park, K. H. Law, C. R. Farrar, "Combination of a Time Reversal Process and a Consecutiv Outlier Analysis for Baseline-free Damage Diagnosis", Intell. Mater. Syst. Struct. J., Vol. 18, 2007, pp. 335-346.

[11]] D. W. Greve, J. J. Neumann, J. H. Nieuwenhuis, I. J. Oppenheim, N. L. Tyson, "Use of Lamb waves to monitor plates: experiments and simulations", Proc. SPIE, Vol. 5765, Smart Struct. and Mater. , Sensors and Smart Struct., Technologies for Civil, Mechanical, and Aerospace Systems, Vol. 3, 2005, pp. 117-129.

[12] M. Lowe, O. Diligent, "Low-frequency reflection characteristics of the S_0 Lamb wave from a rectangular notch in a plate", Acoust. Soc. Am. J., Vol. 111, 2002, pp. 64-76.

[13] J. Rajagopalan, K. Balasubramaniam, C. Krishnamurthy, "A single transmitter multi receiver (STMR) PZT array for guided ultrasonic wave based structural health monitoring of large isotropic plate structures", Smart Mater. Struct. J., Vol. 15, 2006, pp. 1190-1198.

[14] P. Malinowski, T. Wandowski, I. Trendafilova, W. Ostachowicz, "Optimization of sensor placement for structural health monitoring: a review", Struct. Health Monitor. J., Vol. 18, 2019, pp. 963-988.

[15] B. Alem, A. Abedian, K. Nasrollahi-Nasab, "Reference-Free Damage Identification in Plate-Like Structures Using Lamb-Wave Propagation with Embedded Piezoelectric Sensors", Aerosp. Eng. J., Vol. 29, 2016, pp. 04016062-1 - 04016062-13.

[16] C. Q. Gómez Muñoz, F. P. García Marquez, B. H. Crespo, K. Makaya, "Structural health monitoring for delamination detection and location in wind turbine blades employing guided waves", Wind Energy J. , Vol. 22, 2019, pp. 698-711.

[17] M. Gresil V. Giurgiutiu, "Guided wave propagation in carbon composite laminate using piezoelectric wafer active sensors", Smart Mater. Struct. J., Vol. 16, 2013, pp. 75-88.

[18] C. M. Yeum, H. Sohn, J. B. Ihn, H. J. Lim, "Instantaneous delamination detection in a composite plate using a dual piezoelectric transducer network", Compos. Struct. J., Vol. 94, 2012, pp. 3490-3499.

[19] V. Giurgiutiu and G. Santoni-Bottai, "Structural health monitoring of composite structures with piezoelectric wafer active sensors", AIAA J., Vol.49, 2011, pp. 565-581.

[20] H. W. Park, H. Sohn, K. H. Law, C. R. Farrar, "Time reversal active sensing for health monitoring of a composite plate", Sound Vib. J., Vol. 302, 2007, pp. 50-66.

[21] H. Sohn, H. W. Park, K. H. Law, C. R. Farrar, "Damage detection in composite plates by using an enhanced time-reversal method", Aerosp. Eng. J., Vol. 20, 2007, pp. 141-154.

[22] K. Kyoung-Tak, C. Heoung-Jae, S. Joo-Hyun, L. Jin-Ah, B. Joon-Hyung, U. Moon-Kwang, L. Sang-Kwan, J. Ju-Woong, "Quantitative

Accessibility of Delamination in Composite Using Lamb Wave by Experiments and FEA", Adv. Compos. Mater. J., Vol. 20, 2011, pp. 361-373.
[23] CT Ng, H. Mohseni, HF Lam, "Debonding detection in CFRP-retrofitted reinforced concrete structures using nonlinear Rayleigh wave", Mech. Syst. Sig. Proc. J., pp. 245-256.
[24] H. Sohn, "Effects of environmental and operational variability on structural healthmonitoring" , Philosophical Trans. R. Soc. A: Proc. Math., Phys. Eng. Sci. J., Vol. 365, 2007, pp. 539-560.
[25] A. Marzani, S. Salamone, "Numerical prediction and experimental verification of temperature effect on plate waves generated and received by piezoceramic sensors", Mech. Syst. Sig. Proc. J., Vol. 30, 2012, pp. 204-217.
[26] S. Roy, K. Lonkar, V. Janapati, F. K. Chang, "A novel physics-based temperature compensation model for structural health monitoring using ultrasonic guided waves", Struct. Health Monitor. J., Vol. 13, 2014, pp. 321-342.
[27] G. B. Santoni, L. Yu, B. Xu, V. Giurgiutiu, "Lamb Wave-Mode Tuning of Piezoelectric Wafer Active Sensors for Structural Health Monitoring", Vib. Acoust. Trans. ASME J., Vol. 129, 2007, pp. 752-762.
[28] S. B. Kim, H. Sohn, "Instantaneous reference-free crack detection based on polarization characteristics of piezoelectric materials", Smart Mater. Struct. J., Vol. 16, 2007, pp. 2375-2384.
[29] B. Alem, A. Abedian, "A semi-baseline damage identification approach for complex structures using energy ratio correction technique", Struct. Cont. Health Monitor. J., Vol. 25, 2018.
[30] M.H. Ataei, S.A Hassanzadeh-Tabrizi, M.Rafiei, A. Monshi, "Design development of $(Ba_{1-x}Ca_x)(Ti_{1-y}Sn_y)O_3$ lead-free piezo ceramic by two manufacturing methods of CSS and SPS, promising for delamination damage detection", Alloys Compd. J., Vol. 795, 2019, pp. 197-206.
[31] H. Cho, C. J. Lissenden, "Structural health monitoring of fatigue crack growth in plate structures with ultrasonic guided waves", Struct. Health Monitor. J., Vol. 11, 2012, pp. 393-404.
[32] A. Bagheri, K. Li, P. Rizzo, "Reference-free damage detection by means of wavelet transform and empirical mode decomposition applied to Lamb waves", Intell. Mater. Syst. Struct. J., Vol. 24, 2013, pp. 194-208.
[33] F. Moser, L. J. Jacobs, "Modeling elastic wave propagation in waveguides with the finite element method", NDT Int. J., Vol. 32, 1999, pp. 225-234.
[34] I. Bartoli, F. L. di Scalea, M. Fateh, E. Viola, "Modeling guided wave propagation with application to the long-range defect detection in railroad tracks", NDT Int. J., Vol. 38, 2005, pp. 325-334.
[35] L. De Marchi, A. Marzani, N. Speciale, E. Viola, "A dispersion compensation procedure to extend pulse-echo defects location to irregular waveguides", NDT Int. J., Vol. 54, 2013, pp. 115-122.
[36] M. Sale, P. Rizzo, A. Marzani, "Semi-analytical formulation for the guided waves-based reconstruction of elastic moduli", Mech. Syst. Sign. Process J., Vol. 25, 2011, pp. 2241-2256.
[37] H. W. Park, S. B. Kim, H. Sohn, "Understanding a time-reversal process in Lamb wave propagation", Wave Motion J., Vol. 46, 2009, pp. 451-467.
[38] S. R. Anton, D. J. Inman, G. Park, "Reference-free damage detection using instantaneous baseline measurements", AIAA J., Vol. 47, 2009, pp. 1952-1964.
[39] H. Sohn, G. Park, J. R. Wait, N. P. Limback, C. R. Farrar, "Wavelet-based active sensing for delamination detection in composite structures", Smart Mater. Struct. J., Vol. 13, 2004, pp. 153-164.
[40] S. A. Atashipour, H. R. Mirdamadi, M. H. Hemasian-Etefagh, "An effective damage identification approach in thick steel beams based on guided ultrasonic waves for structural health monitoring applications", Intell. Mater. Syst. Struct. J., Vol. 24, 2013, pp. 584-597.
[41] X. Zhao, H. Gao, G. Zhang, B. Ayhan, F. Yan, C. Kwan, J. L. Rose, "Active health monitoring of an aircraft wing with embedded piezoelectric sensor/actuator network: I. Defect detection, localization and growth monitoring", Smart Mater. Struct. J., Vol. 16, 2007, pp. 1208-1219.

JMATPRO	Journal of Advanced Materials and Processing 9 (3): 15-22, Summer 2021 http://jmatpro.iaun.ac.ir 20.1001.1.2322388.2021.9.2.6.4

Research Paper

Effects of Active Material Particles Size Distribution on the Fabrication of $TiNb_2O_7$ Electrode Used in Lithium-Ion Batteries

Touraj Adhami[1], Reza Ebrahimi-Kahrizsangi[1*], Hamid Reza Bakhsheshi-Rad[1*], Somayeh Majidi[2], Milad Ghorbanzadeh[3]

1. Advanced Materials Research Center, Materials Engineering Department, Najafabad Branch, Islamic Azad University, Najafabad, Iran

2. Department of Chemistry, Najafabad Branch, Islamic Azad University, Najafabad, Iran

3. Materials and Energy Research Center, Karaj, Iran

ARTICLE INFO

Article history:

Received 5 October 2020
Accepted 2 February 2021
Available online 1 May 2021

Keywords:
Anode materials
particle size
uniform distribution
Li ion battery
electrode

ABSTRACT

In this study effect of active material particle size distribution (PSD) on $TiNb_2O_7$ electrodes and their performance were evaluated. To determine the effect of PSD, have focused on the performance of the electrode, which is mainly affected by the performance of individual particles and their interaction. For this purpose, $TiNb_2O_7$ was successfully synthesized by mechanochemical method and post-annealing, as an anode material for lithium-ion batteries. Phase identifications and microstructure characterization was carried out by X-ray diffraction (XRD) and field emission scanning electron microscopy (FESEM) to identify the phases and evaluate the morphology of the synthesized samples. The charging and discharging tests were conducted using a battery-analyzing device for evaluating the electrochemical properties of the fabricated anodes. Eventually, at faster charging rates, the electrochemical performance was found to be improved when smaller active material particle size distribution was used. Differences in particles size distributions resulted in variable discharge capacities so that the sample with particle size higher than 25 microns (>25 μm) showed a capacity of 19 mAh/g after 179 cycles, which had a lower capacity than their sample with particle size less than 25 microns (<25 μm). The final capacity of the sample with a particle size less than 25 microns is 72 mAh/g.

Citation: Bakhtiari, L., Jafari, A., Sharafi, Sh., (2021) The Effect of Reverse Pulse Plating and Lanthanum Addition in Plating Bath on Corrosion Resistance of Austenitic Steel in Chlorine Solution, Journal of Advanced Materials and Processing, 9 (3), 15-22. Dor: 20.1001.1.2322388.2021.9.2.6.4

*** Corresponding Authors**:
E-mail: rezaebrahimi@iaun.ac.ir, rezabakhsheshi@gmail.com

1. Introduction

Nowadays, intermediate metal oxides with high specific capacity and good cyclability in the anode materials development used in lithium-ion batteries have been extensively studied [1,2]. Among these, $TiNb_2O_7$ chemical composition was considered by many researchers [3,4] due to their unique characteristics such as high theoretical capacities of 387 mAh/g (much more than $Li_4Ti_5O_{12}$: 175 mAh/g), the process of rapid insertion and extraction of lithium-ion owing to rapid reaction kinetics, and high operating voltage (~1.6 sv, Li/Li^+) which can prevent the formation of solid electrolyte interface (SEI) layer. However, the operating discharge of these materials is not quite satisfactory due to their weak electric conductivity and the slow rate of ion transfer [3-5]. Various approaches and strategies, including reducing the particles size and improving the specific area, and designing the porous structures, were investigated to address this issue since a higher specific area shortens the distance for penetration of lithium ions, improves the electric conductivity, and will consequently improve the lithium ions storage performance [4,6]. However, an important fact that is often overlooked in electrode fabrication is the electrode particle size and the narrow distribution of particle size at the electrode surface. The broad and dissimilar particle sizes, active material particles are not similar in terms of morphology and size, and therefore have a heterogeneous system at its highest level. The degradation of Li-ion batteries is related to the particle size distribution (PSD) of the active material. In graphite anodes, solvent co-intercalation can cause particles to crack, and gas evolution leads to the same thing as well [7,8]. Moreover, in case of any changes in the volume of particles, contact loss will happen between particles [9]. Various materials show the agglomeration of particles in Li-ion batteries [6-8], and this is particularly significant and critical for those materials with considerable variations in their volumes [10] or use nanosized particles [8]. Therefore, although it has been proven in the discussion of making lithium-ion batteries that reducing the particle size improves its performance, while the actual shape and size distribution effect is often not examined. The PSD of the active material is a well-known property in Li-ion batteries and can be adjusted during the manufacture of battery electrodes [11,12]. Therefore, in order to better and more accurately understand the subject, the particle size distribution of active materials at the electrode surface and its effect on the performance of $TiNb_2O_7$ anode will be investigated in this research.

2. Experimental Procedure

$TiNb_2O_7$ ceramic powder was produced as the following reaction:

$$TiO_2 + Nb_2O_5 \rightarrow TiNb_2O_7 \quad (1)$$

N_2O_5 (99. 5% purity, particles size 25 μm) and TiO_2 (99% purity, < 2 μm) were the raw materials used to reach this goal. The purchase of the whole chemical was from Merk, and none of them were purified. To perform the MA process, a high-energy planetary ball mill was used with hardened chromium steel vials (vol. 125 ml) and balls (15 and 20 mm in diameter) while the purity of the argon atmosphere under which the process was performed was high. The speed of rotation was set up to 600 rpm. The ball-to-powder weight ratio (BRP) was considered 15:1, where the total mass of the powder was 7 g. Every 45 minutes, the milling planetary is stopped for 15 minutes so that the temperature will not be rising. The milling time was equal to 5 hours. In the next step to complete the chemical reactions and remove the raw materials, Samples were annealed in a tube furnace under an oxygen atmosphere for 2 hours at 900 °C. Evaluating the phase and crystallographic structural properties of the nano-powder; the X-ray diffraction was used. The collection of the XRD patterns was performed over the 2θ angular range between 20 and 60 at a scan rate of 1°/min. XRD data was needed to be analyzed, the PANalytical X'Pert High Score software can be used. We can compare the XRD patterns and standards to those standards which are compiled by the Joint Committee on Powder Diffraction and Standards (JCPDS), #01-070-2009 for $TiNb_2O_7$, #01-072-0158 for $Ti_2Nb_{10}O_{29}$, #01-071-1168 for TiO_2, and #01-030-0873 for Nb_2O_5. The morphological features of $TiNb_2O_7$ nano-powders were examined on a Field emission scanning electron microscope (FESEM; Vega©-Tescan, Brno, Czech Republic) that operated at the acceleration voltage of 15 kV. Energy-dispersive X-ray spectrometry (EDS) attached to the FESEM was also utilized for semi-quantitative examination of the samples. To determine the volume fraction of grain boundary of the nano-powders, the edge-mode of the FESEM images was employed. After the production of $TiNb_2O_7$ nano-powder, the synthesized powder was divided into two parts to investigate the uniform particle size distribution effect of active materials on the electrochemical performance of the anode (Table 1). Then a group of samples passed through a screen with 500 mesh (< 25 μm) and then entered the electrode manufacturing stage. While the other group entered the slurry and electrode production stage directly without passing through the screen.

Table 1. Specifications of the applied parameters in the experimental process.

Sample No.	Stoichiometric reaction	Milling time (h)	Furnace/annealing atmosphere	Annealing time (h)	Annealing temperature (°C)	Screen
N1	$TiNb_2O_7$	5	Tube/oxygen	2	900	Yes
N2	$TiNb_2O_7$	5	Tube/oxygen	2	900	No

Lithium-ion storage performance in the compositions of $TiNb_2O_7$ was investigated using the $Li/TiNb_2O_7$ half-cells. When each of the synthesized materials is mixed with polyvinylidene fluoride (PVDF), and black carbon, which acts like the adhesive and conductor, weight ratio 70:15:15 inside N-Methyl-2-pyrrolidone (MNP), the electrodes that are used at practical work can be produced. The slurry we gained covered a copper foil, and this was then dried for 12 hours under the temperature of 120 °C inside an oven under vacuum condition. In each half-cell, the ande material was loaded at a rate of 1 mg/cm^2 in accordance with the previously performed work [13,14]. The separator used in this study was a thin layer (film) of polypropylene (Celgard 2400). A standard vacuum glovebox with a pure lithium foil as a cathode/ counter in the coin cells was used to mount each of the prepared anodes inside it (CR 2032). Combining one molar LiPF6 in ethylene carbonate (EC), diethyl carbonate (DEC), and dimethyl carbonate (DMC), the preparation of the used electrolytes took place. A battery analyzer (BTS4000 5V) device by galvanostatic cycles in the voltage range of 0 to 3 volts at room temperature was used to perform charging and discharging tests. Then, an electrochemical impedance test was used to calculate the diffusion coefficient of lithium-ion in each half cell. The equation used to calculate the diffusion coefficient is as follows [14]:

$$D = R^2T^2/2A^2n^4F^4C^2\sigma_w^2 \quad (2)$$

where R is the gas constant (8.314 J/mol K), T is the absolute temperature, n is the number of electrons exchanged in each molecule during the redox process, A is the surface area of the electrode (1.77 cm^2), C is the lithium-ion concentration (7.69×10^{-13} mol.cm^{-3}), F is the Faraday constant (96486 C/mol), and σ_w is a Warburg factor that is directly related to Z', as follows:

$$Z' = R_e + R_{ct} + \sigma_w^{-1/2} \quad (3)$$

where Z' is the real part of the electrochemical impedance test, indicating the general resistance of the cell, R_e represents the resistances due to the electrode and electrolyte, and R_{ct} is the charge transfer resistance.

3. Results and Discussion:

3.1. Phase analysis and structural features

Fig. 1 shows the X-ray diffraction pattern of the powder sample synthesized before and after the annealing process. According to Fig. 1a, the un-annealed sample was composed of TiO_2 and Nb_2O_5 [13]. Besides, several product peaks corresponding to $TiNb_2O_7$, $Ti_2Nb_{10}O_{29}$, and $TiNb_{24}O_{62}$ were detected. Compounds of $TiNb_2O_7$, $Ti_2Nb_{10}O_{29}$, and $TiNb_{24}O_{62}$ all belong to the same family, which are obtained by reacting between TiO_2 and Nb_2O_5 with different stoichiometry. Therefore, phase overlap is strongly observed between these three compounds. The XRD patterns of the annealed products are shown in Fig. 1b [13]. It can be seen that the characteristic peaks of TiO_2 and Nb_2O_5 were completely removed in the annealing process. Based on clearly defined X-ray patterns, annealing operations lead to the completion of the chemical reaction and the removal of raw materials peaks.

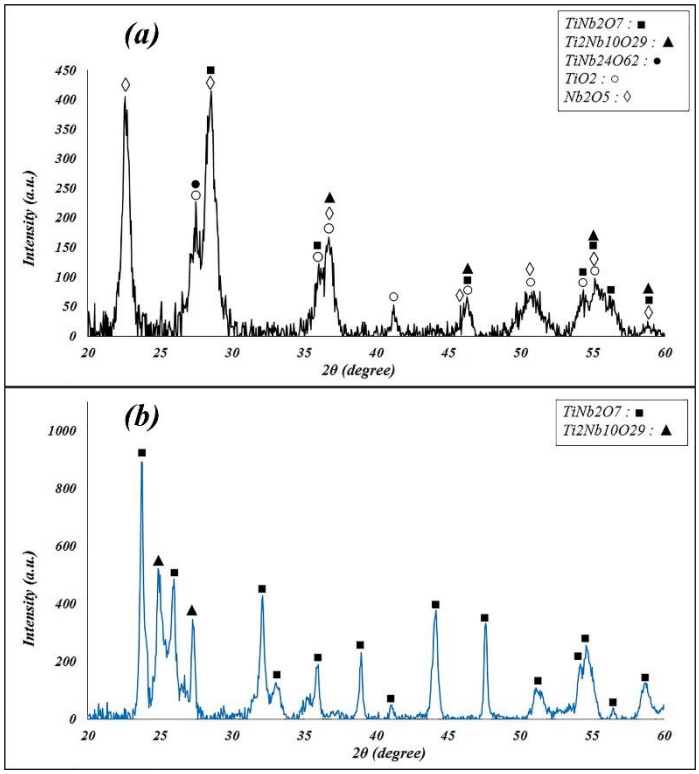

Fig. 1. Diffracted X-ray patterns of the compounds $TiNb_2O_7$: (a) before annealing (b) after annealing [13].

3.2. Morphological evaluations characteristics

Fig. 2 shows an image of the synthesized $TiNb_2O_7$ powder before the electrode was made. In this figure, the agglomeration of particles is observed. The agglomeration phenomenon has occurred due to the reduction of particle size caused by milling and the increase in the surface defects, which results in an unstable surface, and with a longer milling time, the system will reach a stable state. The surface diameter size of the synthesized particles is in the range of 13 to 24 nm. The EDS analysis and elemental mapping were used to understand the XRD results better, as shown in Fig. 3. According to the EDS spectrum (Fig. 3a), the main components of the nano-powder in terms of the element were oxygen, niobium, and titanium. From elemental mapping analysis (Fig. 3b), the nano-powder showed a homogenous distribution of O, Nb, and Ti elements which confirmed the formation of a uniform microstructure after annealing.

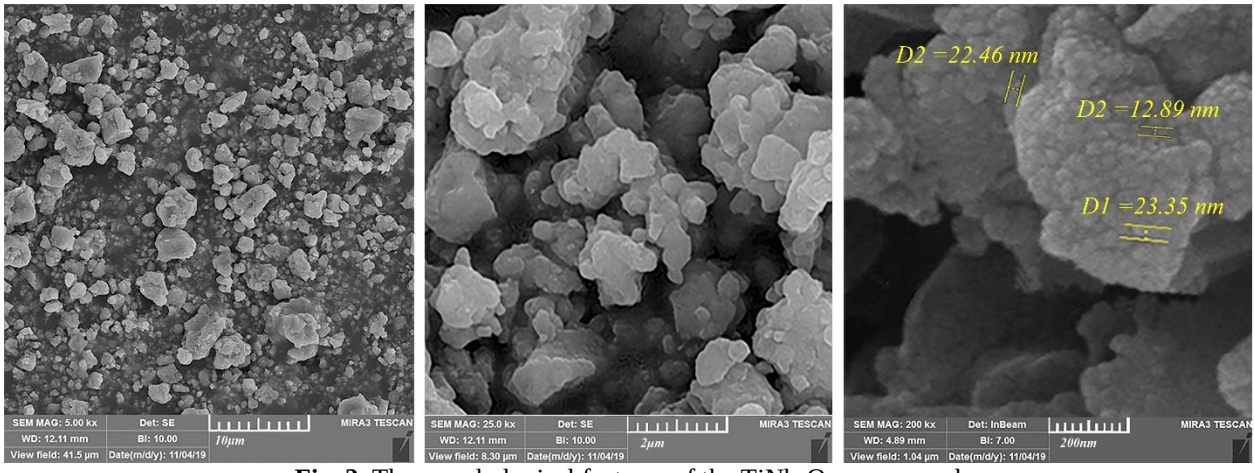

Fig. 2. The morphological features of the $TiNb_2O_7$ nano-powders.

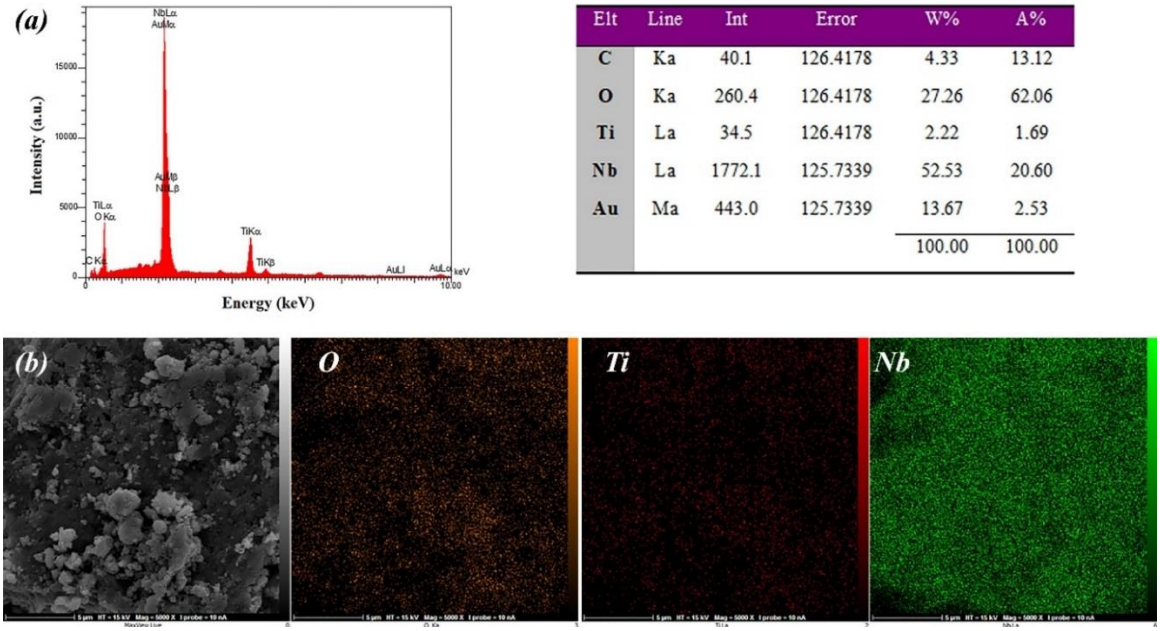

Elt	Line	Int	Error	W%	A%
C	Ka	40.1	126.4178	4.33	13.12
O	Ka	260.4	126.4178	27.26	62.06
Ti	La	34.5	126.4178	2.22	1.69
Nb	La	1772.1	125.7339	52.53	20.60
Au	Ma	443.0	125.7339	13.67	2.53
				100.00	100.00

Fig. 3. (a) EDS analysis and (b) elemental mapping images of $TiNb_2O_7$ sample

3.3. Charging and discharging curves

To investigate the effect of particle size distribution on the electrochemical performance of $TiNb_2O_7$ anodes, the made electrodes were charged and discharged during 179 cycles at different C rates (Table 2). Fig. 4 shows a comparison graph of the discharge diagrams of the two samples N1 and N2. As can be seen at all C rates, the performance of the sample (with uniform particle size distribution) is much better than that of the sample containing non-uniform particle distribution, so that the difference in the final capacity at the end of each C rate, including 0.1C, 0.2C, 0.5C, 1C, 2C, and 4C is equal to 45, 50, 73, 73, 62 and 53 mAh/g, respectively. In other words, the yield of a heterogeneous sample (N2) is on average 50% of a homogeneous sample (N1). Fig. 5 shows the FESEM images of the two samples N1 and N2, after being placed in the charge and discharge cycles and completion of the work process. As can be seen in the figure, the N1 sample (sample with particle size less than 25 microns) has a more uniform appearance and morphology than the N2 sample. Heterogeneous distribution of particles will reduce battery life and cyclability. Even in practical conditions, after the electrode slurry made on the copper foil is coated, the coating obtained from the sample with particle size less than 25 microns is much softer and more uniform. In comparison, the sample with a particle size higher than 25 microns has a rough coating, which causes a potential difference, reducing the contact surface between the particles and the loss of the separator during the assembly process or the charge and discharge cycles.

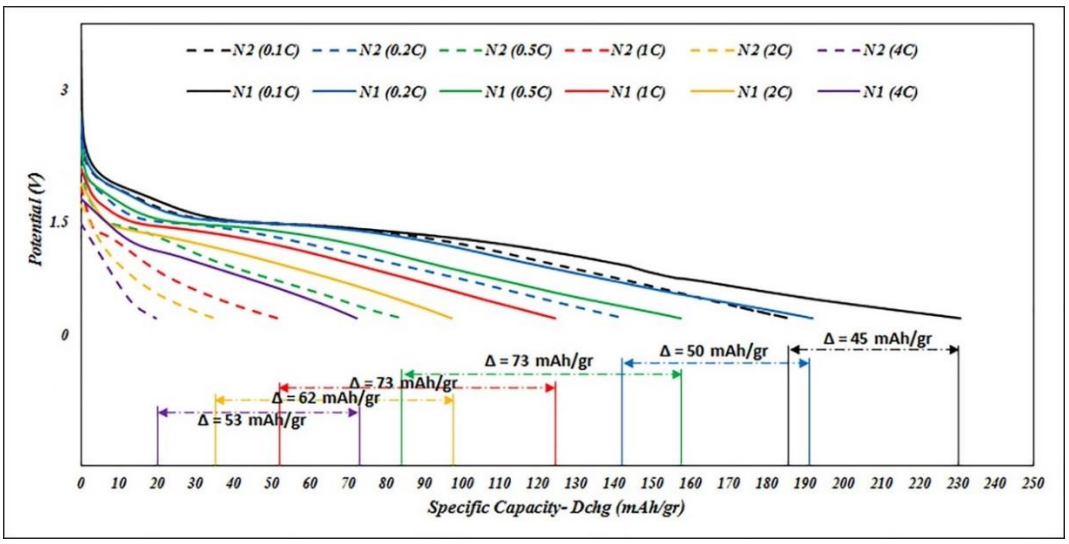

Fig. 4. Comparison of discharge diagrams of two samples N1 and N2.

Table 2. Electrochemical performance of the produced electrodes.

		No. of cycles per each crate						Capacity (mAh/g)					
Sample No.	Cycle No.	0.1C	0.2C	0.5C	1C	2C	4C	0.1C	0.2C	0.5C	1C	2C	4C
N1	179	4	8	23	48	48	48	231	192	157	124	97	72
N2	179	4	8	23	48	48	48	186	142	84	51	35	19

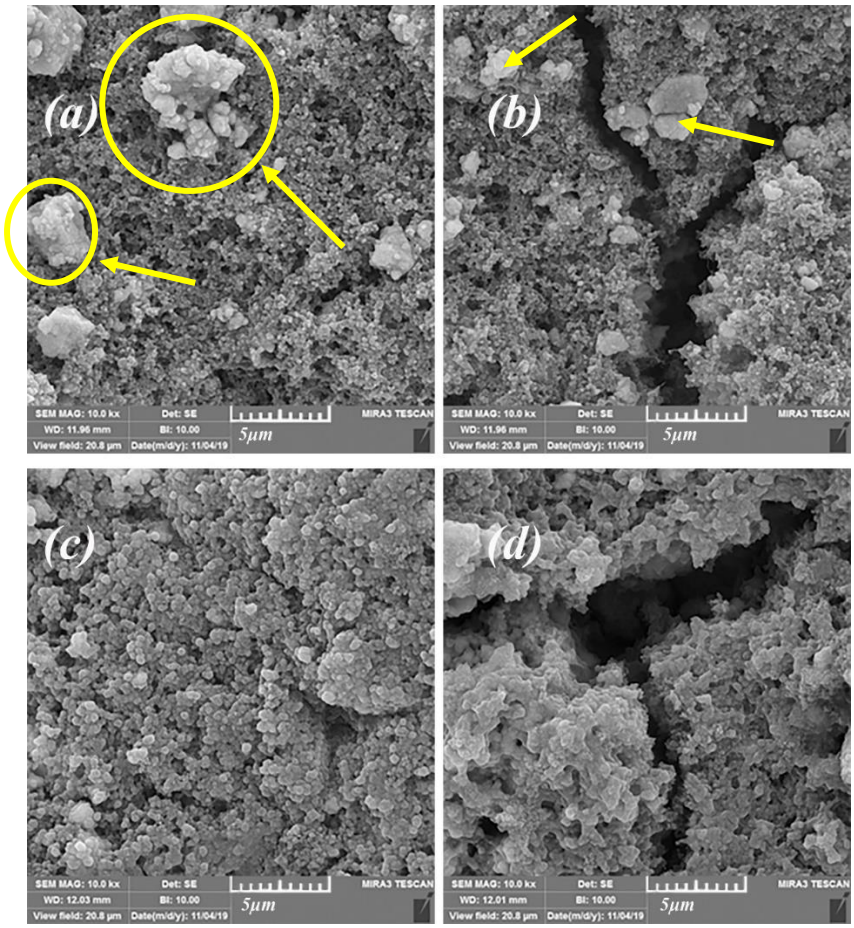

Fig. 5 (a, b) The morphological features of the N2, (c, d) The morphological features of the N1.

Figure 6 is a diagram of the cyclability of the two samples N1 and N2, which shows the difference in the capacity retention and cyclability of both samples and confirms the poor performance of sample N2.

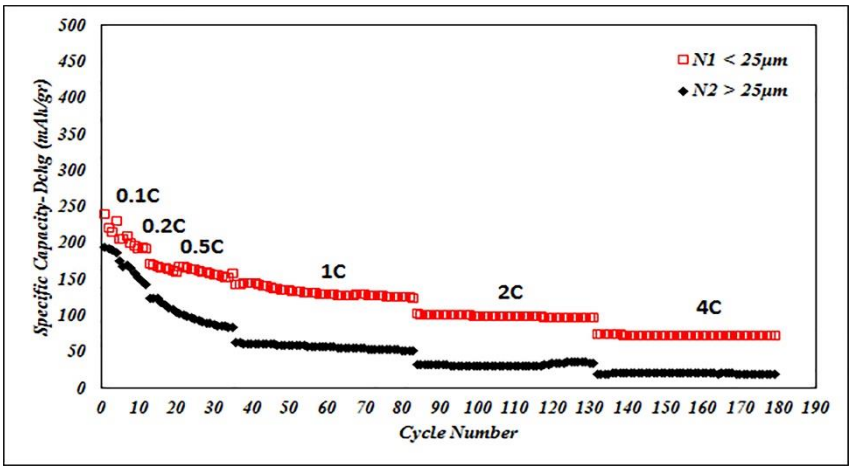

Fig. 6. Cyclic stability or cyclability of N1 and N2.

3.4. Electrochemical Properties

The electrochemical impedance (EIS) test is performed when the cell is totally discharged. Figure 7 shows the Nyquist diagrams of the sample with particle size less than 25 microns [13] and sample with a particle size of more than 25 microns (the corresponding curve is placed in the figure for performing the fitting process of lab data for the EIS test). An intercept is observed at high frequencies, followed by a semicircle in the medium frequency region and a straight line at a low frequency. Ohmic resistors (R_e) include electrolyte and electrode resistors seen as the intercept impedance in the Z' axis. The charging transfer resistors (R_{ct}), available between the anodic material and electrolyte, are in conformity with the diameter of the semicircle on the Z' axis. The tailbone or the straight line is connected with the emission of lithium ions in the electrode bulk, known as the Warburg diffusion (Z_w). Double layer strength and capacitive surface film are shown as the fixed phase element (CPE) [14,15].

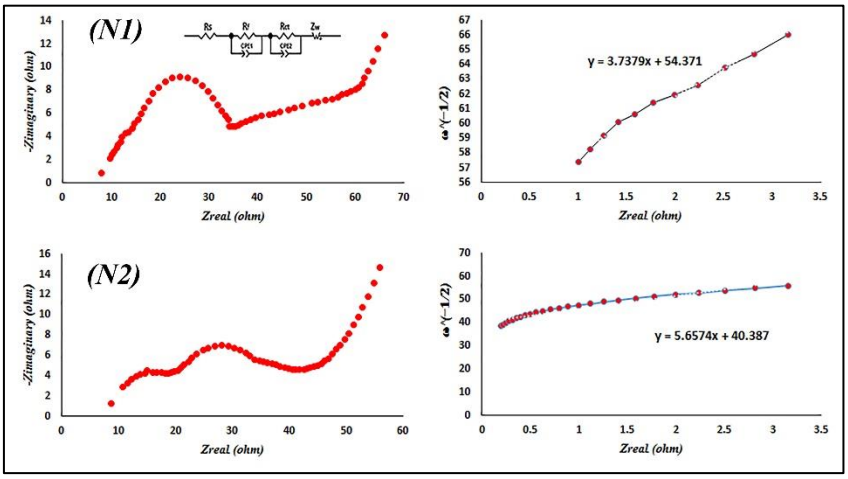

Fig. 7. EIS spectra of the sample with particle size less than 25 microns (N1) [13] and the sample with particle size more than 25 microns (N2)

Table 3 appears the fitting comes about of the impedance test of the tests. In this table, the Rct values of the sample with particle size less than 25 microns and the sample with particle size more than 25 microns are presented, which in N1 and N2 are equal to 29 and 51 $\Omega\ cm^2$, separately. Therefore, using Equation 2, the diffusion coefficient of lithium ions in each sample was calculated. According to the results, the emission rate of lithium-ion in the sample with particle size less than 25 microns is higher than the sample with a particle size of more than 25 microns, so that the diffusion coefficient in the N1 is equal to 1.24×10^{-11} cm^2/s, which is approximately 2.3 times the sample N2 with a diffusion coefficient of 5.42×10^{-12} cm^2/s.

Table 3. EIS parameters of the produced electrodes

Sample	R_e ($\Omega\ cm^2$)	R_{ct} ($\Omega\ cm^2$)	i_0 (mA cm^2)	σ_w ($\Omega\ cm^2\ s^{1/2}$)	D_c (cm^2/s)
N1	16.19	29	8.85×10^{-4}	3.74	1.24×10^{-11}
N2	8.76	51	5.03×10^{-4}	5.65	5.42×10^{-12}

4. Conclusion

In this study, we investigated the particle size distribution as an essential parameter in the performance of the $TiNb_2O_7$ anode. The presented results show the effect of shape and scale of particle size distribution on the performance of electrodes. In general, the smaller and more uniform the particle size distribution, the correlation and contact surface between the particles increase, and the faster displacement of lithium ions. Hence, the ability to maintain capacity at higher C rates will be better. Differences in particles size distributions resulted in variable discharge capacities so that the sample with a particle size of more than 25 microns showed a capacity of 19 mAh/g after 179 cycles, which had a lower capacity than their sample with particle size less than 25 microns. The final capacity of the sample with a particle size less than 25 microns is 72 mAh/g.

References

[1] Y. Liu, Y. Yang, "Recent progress of TiO_2-based anodes for Li ion batteries", Journal of Nanomaterials, vol. 2016, 2016, pp. 1-15.

[2] S. K. Balasingam, M. Kundu, B. Balakrishnan, H. Kim, A. M. Sevensson, K. Jayasayee, "Hematite microdisks as an alternative anode material for

lithium-ion batteries", Materials Letters, vol. 247, 2019, pp. 163-166.
[3] S. Li, X. Cao, C. N. Schmidt, Q. Xu, E. Uchaker, Y. Pei, G. Cao, "$TiNb_2O_7$/graphene composites as high-rate anode materials for lithium/sodium ion batteries", Journal of Materials Chemistry A, vol. 4, 2016, pp. 4242-4251.
[4] X. Xia, Sh. Deng, Sh. Feng, J. Wu, J. Tu, "Hierarchical porous $Ti_2Nb_{10}O_{29}$ Nanospheres as superior anode materials for lithium-ion storage", Journal of Materials Chemistry A, vol. 5 2017, pp. 21134-21139.
[5] D. Pham-cong, J. Kim, V. T. Tran, S.J. Kim, S. Jeong, J. Choi, Ch. Cho, "Electrochemical behavior of interconnected $Ti_2Nb_{10}O_{29}$ nanoparticles for high-power Li-ion battery anodes", Electrochimica Acta, vol. 236, 2017, pp. 451-459.
[6] G. Zhu, Y. Wang, Y. Xia, "Ti-based compounds as anode materials for Li-ion batteries", Energy & Environmental Science, vol. 5, 2012, pp. 6652-6667.
[7] D. Aurbach, B. Markovsky, I. Weissman, E. Levi, Y. Ein-Eli, "On the correlation between surface chemistry and performance of graphite negative electrodes for Li ion batteries", Electrochimica Acta, vol. 45, 1999, pp. 67-86.
[8] B. Michalak, H. Sommer, D. Mannes, A. Kaestner, T. Brezesinski, J. Janek, "Gas Evolution in Operating Lithium-Ion Batteries Studied in Situ by Neutron Imaging", Scientific Reports, vol. 5, 2015, pp. 1-9.
[9] F. Rçder, S. Sonntag, D. Schrçder, U. Krewer, "Simulating the Impact of Particle Size Distribution on the Performance of Graphite Electrodes in Lithium-Ion Batteries", Energy Technology, vol. 4, 2016, pp. 1-11.
[10] Zh. Wu, W. Ren, L. Wen, L. Gao, J. Zhao, Z. Chen, G. Zhou, F. Li, H. Cheng, "Graphene Anchored with Co_3O_4 Nanoparticles as Anode of Lithium-Ion Batteries with Enhanced Reversible Capacity and Cyclic Performance", ACS Nano, vol. 4, 2010, pp. 3187-3194.
[11] G. T. Feya, Y. G. Chen, H. Kao, "Electrochemical properties of $LiFePO_4$ prepared via ball-milling", Journal of Power Sources, vol. 189, 2009, pp. 169-178.
[12] Th. Drezen, N. Kwon, P. Bowen, I. Teerlinck, M. Isono, I. Exnar, "Effect of particle size on $LiMnPO_4$ cathodes", Journal of Power Sources, vol. 189, 2009, pp. 169-178.
[13] T. Adhami, R. Ebrahimi-Kahrizsangi, H. R. Bakhsheshi-Rad, S. Majidi, M. Ghorbanzadeh, F. Berto, "Synthesis and electrochemical properties of $TiNb_2O_7$ and $Ti_2Nb_{10}O_{29}$ anodes under various annealing atmospheres", Metals, vol. 11, 2021, pp. 1-12.
[14] A. R. Madram, R. Daneshtalab, M. R. Sovizi, "Effect of Na^+ and K^+ co-doping on the structure and electrochemical behaviors of $LiFePO_4$/C cathode material for lithium-ion batteries", Royal Society of Chemistry, 2016, pp. 101477-101484.
[15] L. Buannic, J. Colin, Lise Daniel, S. Patoux, "Effect of syntheses and post synthetic treatments on mixed titanium niobium oxides for use as negative electrode in high power Li-ion batteries", Electrochemical Society, 2013.

JMATPRO	Journal of Advanced Materials and Processing 9 (3): 23-34, Summer 2021 http://jmatpro.iaun.ac.ir 20.1001.1.2322388.2021.9.3.2.2

Research Paper

The Effect of Reverse Pulse Plating and Lanthanum Addition in Plating Bath on Corrosion Resistance of Austenitic Steel in Chlorine Solution

Leila Bakhtiari[1], Abdolhamid Jafari[2*], Shahriyar Sharafi[3]

1. Ph.D. student, Materials Science and Engineering Dept., Shahid Bahonar University, Jomhori-e-Eslami Blvd., Kerman, Iran

2. Associate Professor, Materials Science and Engineering Dept., Shahid Bahonar University, Jomhori-e-Eslami Blvd., Kerman, Iran

3. Professor, Materials Science and Engineering Dept., Shahid Bahonar University, Jomhori-e-Eslami Blvd., Kerman, Iran

ARTICLE INFO

Article history:

Received 10 November 2020
Accepted 16 December 2020
Available online 1 May 2021

Keywords:
Coating
Stainless steel
Lanthanum
Pulse reverse plating
Corrosion

ABSTRACT

The 316L nickel-chrome molybdenum austenitic stainless steel is commonly employed in various industries. This type of steel is particularly of interest in chemical industries, especially in harsh and corrosive environmental conditions. Although 316L stainless steel has good mechanical and corrosive characteristics, it fails to perform well in chlorine-containing aqueous environments. To overcome this issue, a Ni-La-Cr-Fe layer is applied to the 316L steel using the electroplating method. In addition, the reverse pulse plating method is used to control the ion deposition kinetics. The plating current application duration (on-time), the current disruption duration (off-time), and (TRev) are the control parameters of the duration and polarity of the pulse. Finally, the coated layer acquires an average thickness of 6.83 after applying on-time and off-time repeatedly and performing SEM and polarization tests in 1.5% solution at 50 Celcius degrees. Furthermore, the desired surface morphology is achieved, and corrosion resistance is 160 times higher than 316 bare steel. Applying the reverse pulse plating method, adding beneficial compounds of saccharin and SDS, and using lanthanum chloride in the plating bath are the essential reasons to successfully add a coating layer on the 316 bare steel.

Citation: Bakhtiari, L., Jafari, A., Sharafi, Sh., (2021) The Effect of Reverse Pulse Plating and Lanthanum Addition in Plating Bath on Corrosion Resistance of Austenitic Steel in Chlorine Solution, Journal of Advanced Materials and Processing, 9 (3), 23-34. Dor: 20.1001.1.2322388.2021.9.3.2.2

[*] **Corresponding Author**:
E-mail: jafham2020@gmail.com

1. Introduction

The SS316L nickel-based stainless steel is less prone to intergranular corrosion than SS316 steel due to its lower carbon contents. Plate heat exchangers are usually made of SS316L steel. Despite the appropriate corrosion properties of this kind of steel, it suffers from local corrosion. This kind of corrosion possibly stems from the water-soluble industrial salt flowing among the plates. Therefore, numerous studies are conducted on the effects of chlorine ion, which is one of the most crucial ions in cavitation and local corrosion. A combination of water, heat, and chloride-containing salt causes pitting corrosion of the stainless steel. Surface contamination by hygroscopic salt can result in very deep pits over several months. When corrosion occurs under thin moisture layers, pit extension results in shallow pits [1]. The primary reason for chloride influence is attributed to the behavior of passive film on stainless steel in wet and atmospheric conditions. Numerous studies on the effects of environmental variables on the corrosion resistance of stainless steel against pitting corrosion in the presence of chloride demonstrated an inverse linear dependence of the corrosion potential on the temperature in the 25~100ºC interval. Therefore, E_{pit} decreases as the temperature is raised. When the temperature is risen from 25°C to 88°C, the potential decreases four times. The temperature effect on the morphology of the pits in such environments becomes more noticeable at higher temperatures, and shallow spread ones at higher temperatures replace the deep localized pits at temperatures lower than 150°C [1-4].

The density of the pits is inversely dependent on the temperature. In addition, the number of pits decreases at temperatures higher than 100°C, while their diameters are increased [5]. The relationship between the chloride concentration and corrosion resistance in stainless steel is investigated. The studies revealed that the pitting tendency is reduced due to higher positive potentials at lower levels of concentration. In fact, the threshold temperature and amount of chloride for the pitting to have a steady-state corrosion form are shown to be 50°C and 0.5 mol, respectively [5-9]. Heat-resistant steels are used in heat exchangers due to their appropriate mechanical properties and corrosion resistance that is characterized by the composition change of the surface steel [10-13]. A continuous dense coating prevents the diffusion of anions into the alloys. Therefore, generating these kinds of coating naturally or technically on the surfaces is the key to the corrosion resistance of an alloy. Researches demonstrated that the Reverse Pulse Electroplating (RPE) method is influential in forming composite layers and high entropy alloys that are dense and stable and present excellent corrosion resistance [14-17]. Pulse Plating (PP) is used to form a wide range of compositions and properties through effective alteration of the catholyte/cathode interfaces [18-20]. The effects of the rare earth elements on the corrosion (particularly pitting corrosion) and high-temperature oxidation of steels (due to their unique electronic structures and chemical activity) are reported [21-26]. Rare earth salt can improve the Throwing Power (TP) of a plating solution, reduce the grain size of the plating alloy, and make the microstructure of the coating more uniform [27-31]. Electrochemical Impedance Spectroscopy (EIS) is often used to characterize the quality of barrier coating systems. The EIS response is stable, and Kramers-Kronig consistency requirements are met when the three parameters of saturated water volume fraction of the coating, diffusion rate, and the electrical response are low. Higher rates of diffusion, water volume fractions, or electrical impedance responses to the composite system can influence the resonance frequency and consequently the relative impact on the real and imaginary parts of the coating impedance [32]. High hardnesses and a slight increase in corrosion resistance are studied and reported by applying Direct Current Plating (DCP) methods or conventional pulsed plating methods [27-30]. The latter is achieved by including some rare earth metals in nickel plating baths for mild steel. However, according to this study, no research has been conducted on enhancing mechanical performance and high-temperature corrosion by combining lanthanum with the RPE technique.

2. Experiments

2.1. Materials and Research Methods

It is demonstrated in this research that the best possible way to increase the corrosion resistance of 316L steel is to use the Pulsed Electroplating (PE) method and rare earth elements in the plating bath (according to the articles in the field [18-28]. Lanthanum is selected among the rare earth elements because of its results in previous researches [28,29]. In all previous studies, the bath-plating method consists of rare-earth elements, direct-flow plating, or pulsed plating. During the almost three-year period of this study, none of these two methods are shown to be suitable. Finally, the experiments continue until reaching the surface since the produced coating by the reverse pulse plating (RPP) method has a finer grain size, more density than the PP and Direct Flow (DF) methods, and higher quality. The RPP method is applied in this regard [33, 34]. The first thing to be noted in the case of plating ranges is that the TOff is selected in every plating time if the off-time (TOff) is greater than on-time (Ton) since the unstable buds and impurities have more time to peel off the surface, leading to better coating quality, compression, and

adhesion. Multiple TOn and TOff times are tested for the three ranges listed in Table 3. Finally, the best results among all of the tested times are listed. It is observed that range 1 satisfies the objective of the present study among the three ranges.

Experiments are performed using double distilled-deionized water. 3.5% NaCl is added to the water, so the specimens are tested without a calcareous scale on the surface. The SS316L stainless steel specimens of Table 1 are polished with 2000 abrasive papers with one side coated by a thermoset resin.

Table 1. Elemental analysis of SS 316 L austenitic stainless steel

Element	C	Si	S	P	Mn	Ni
Quantity (%)	0.018	0.70	0.002	0.03	1.17	10.22
Element	Cr	Mo	Fe	Cu	W	Co
Quantity (%)	16.71	2.03	68.5	0.36	0.02	0.18

The plating anode is made of 99.9% nickel, and the constituents of the electroplating bath are all Merck's laboratory-grade reagents, as shown in Table 2. Table 3 summarizes various electrical pulse ranges used for the electroplating process.

Table 2. Chemical composition of Ni-La-Cr-Fe plating bath

Constituents	Concentration (gL^{-1})
$NiSO_4.6H_2O$	250
H_3BO_3	35
$C_{12}H_{25}SO_4Na$	0.35
Saccharin	1
$Na_3C_6H_2O.2H_2O$	60
AlCl3.6H20	100
CrNO3.6H2O	100
$LaCl_3.7H_2O$	1
Plating Parameters	
Current Type	Pulse
Plating Time (min)	40
Temperature ($^{\circ}C$)	40
Current Density (Acm^{-2})	1

Table 3. Pulsing ranges employed for Ni-La-Cr-Fe layer plating

No.	On-Time (TOn) /µs	Off-Time (TOff) /µs	Reverse Pulse Time (TRev) /µs
range-1	400	700	100
range-2	1000	1000	100
range-3	10000	10000	100

Fig. 1 shows the represented pulse sequence of table 3 graphically. The current density and TRev are selected to be 1 Acm^{-2} and 100µs, respectively. These values ensure that a fine grain structure and smooth morphology are used throughout the experiment. The plating bath contains $0.35gL^{-1}$ of $C_{12}H_{25}SO_4Na$ to raise the over-potential of the hydrogen evolution reaction (HER). This, in turn, cuts hydrogen produced at cathodic points, eliminates the embrittlement and pinhole formation, and consequently improves coating integrity.

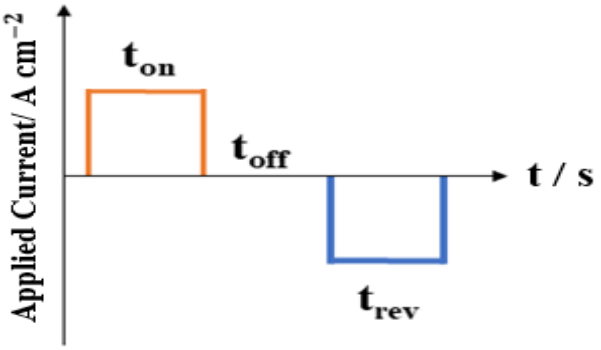

Fig. 1. Schematic representation of PRP plating range used in this study.

2.2. Characterization Method

The XRD, SEM, Potentio-dynamic polarization experiments are performed to characterize the structure and corrosion properties. Moreover, the Tofel polarization is performed at a scan rate of 1mVS-1 using Model PARSTAT-2273 EG&G potentiostat with saturated Ag/AgCl and Pt gauze as a reference and a counter electrode, respectively. The potentials of the electroplated specimens are allowed to stabilize in a 3.5wt% NaCl solution in the potentiostat's three-electrode cells for one hour before each test. The tests are also repeated three times to ensure reproducibility, and the results are analyzed using the Powersuite software. The elemental composition of the compounds formed on the surface and crystallography and morphology of the constituents are studied using SEM Model TeScan Mira III, with EDS for point and linear element analysis and element-distribution mapping. The X-Ray Diffraction (XRD) technique is implemented using Philips Xpert and Cu-kα radiation to evaluate the phase patterns.

3. Results and Discussion

The XRD results of lanthanum-doped coatings for Ni_3La_7, NiFe, and CrFeNi are shown in Fig. 2. Ni_3La_7 indicates a well-developed crystalline structure and clearly demonstrates the coating's preferred growth for 200 planes. Its peak has an intensity three times greater than that of (020) and (022) planes that are the characteristics of nickel. As a rule, the sharp XRD peaks indicate a well-developed polycrystalline structure, and the low, wide peaks obtained from range-1 coatings (represented in Table3) confirm the microstructure is fine. Therefore, these peaks become wider and shorter in range-1 sample as the conditions tend to promote finer grains. This is validated by the SEM images represented in Fig. 3.

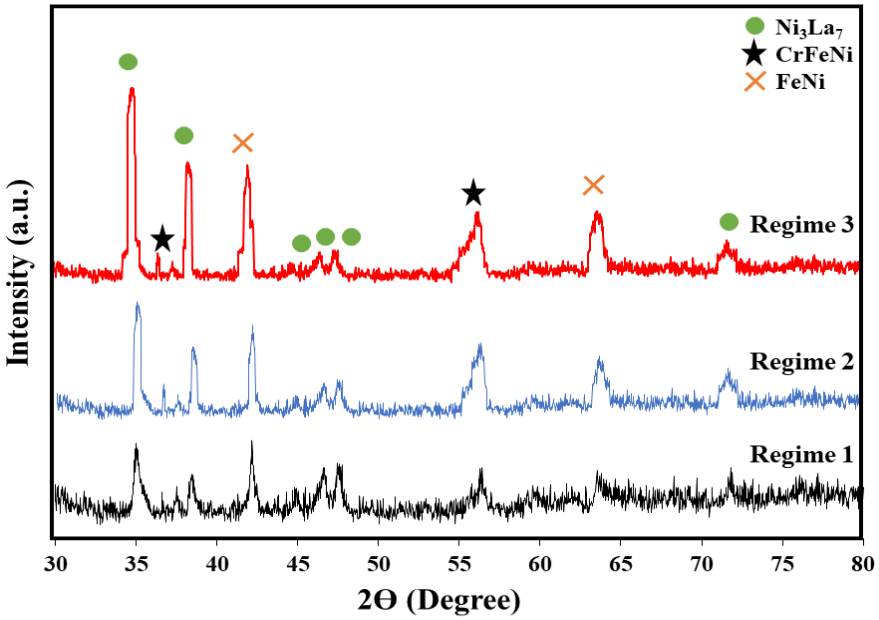

Fig. 2. XRD patterns of coatings formed under plating ranges 1, 2, and 3 of Table 3

The morphology of the specimen coated under the range-1 plating is shown in SEM pictures in Fig. 3. A uniform refined grain structure is often associated with enhanced mechanical properties and better

corrosion resistance, as demonstrated in Fig. 3. This culminates in directional deposit colonies comprising smaller spherical sub-sets. The range-1 samples are composed of closely packed 200nm spheres forming a homogenous surface. In contrast, range-2 samples have grains that clump together, forming coarse granules. This issue is more significant in range-3 coatings where tubular structures with diameters more than 500nm are produced. Some researchers observed this phenomenon and attributed it to the dominant effect of plating current [25]. However, this could be mainly true in DC or one-sided pulse plating, as shown later in this paper.

Rare-earth metals are posited with effects on the electrochemical depositing process and grain refining ability [21]. Lanthanum is a surface-active element with a large atomic radius of 0.1877nm and a valence state of La^{3+} [21, 26]. Thus, its outermost electron-deficient orbital is believed to cause physical adsorption on the surface of a cathode alongside any other cation. However, Ni^{2+} must be chemisorbed first on the basis of its overwhelming activity. Therefore, the nickel content of the electric double-layer falls, leading to a slight positive charge imbalance as La^{3+} concentration increases [26-28]. A rise in cathodic potential is required to provide the necessary energy reduction by deposition current that controls both the supply and subsequent reduction of Ni^{2+} and consequently, prevent the mentioned issue through migration of new cations [29]. It is discussed that a higher over-potential needed for nickel reduction helps to refine grains as the nucleation is sped up and the growth is reduced [28-30]. However, this mechanism is inadequate to explain the significant variation in the grain size in this work. Furthermore, the directional growth patterns observed as the PRP parameters are altered without changing the plating current. In contrast, the plating current frequency of on/off times is found to be particularly relevant. Compared with the effect of this parameter, the range-1 specimens with a shorter current-on time of 400 s (that is almost 2.5 times lower than that for range-2) acquire the most structural uniformity. This is due to the fact that this off-time prevents fast grain growth. The same holds for their current-off time of 700 s, which is enough to initiate nucleation. This time interval is enough to avoid the diffusion layer being formed on the cathode surface with undesirable concentration polarization effects. Finally, this research revealed that the ratio of "off" and "on" periods effectively achieves the desired metallurgical properties. A 2:1 ratio for samples formed under range-1 prevents excessive grain growth. However, as it tends to unity, both nucleation and growth patterns become irregular as this specific PRP function fails. The reverse current step decelerates deposition during the PRP process by removing some of the nascent nuclei. Therefore, according to the present study, it has to be kept within a tight range that falls within the 100~200 ms. Similar time ranges are suggested by other researchers [25]. This helps remove the boundary layer formed due to the diffusion of ions from the solution to the interface of a specimen without affecting the nucleation inordinately.

The linear cross-sectional scan shown in Fig. 4 (a) demonstrates that nickel is the dominant coating element considered for both the plating bath and the substrate containing Ni. It also demonstrates outwards declining concentration of iron that is only a constituent of the substrate, which contains nearly 68.5% Fe as shown in tables 1 and 2. This is in contrast to the observed behavior of nickel. The mechanism of alloy formation during plating by employing the modified nickel bath with appropriate additives is to first remove a thin layer of the stainless steel so that the constituents are incorporated in the converted surface layer. The film's iron content concentration is translated from the substrate towards the top of the coating. This confirms the source of the iron. It is accomplished by controlling the gradual diminishing concentration of Fe through the PRP parameters. Therefore, the common problem of separate phase forming that could jeopardize coating adhesion is tackled. Similarly, chromium is mainly concentrated around the substrate. It originates from this region and participates in forming quaternary Ni-Fe-Cr-Ta high entropy alloy. It also contributes to the coating's good corrosion resistance [31, 35]. The reverse pulse technique allows the dissolution of the nascent nuclei. It also provides conditions similar to the conversion coating (coupled with electroplating) and the Toff duration that prevents the diffusion layer from being generated. Fig. 4 represents the EDS linear scanning to analyze 30 points elementally starting from below the interface to the top of the coating. If the concentration of the main elements Fe, Cr, Ni at the interface is the same as those represented in Table 1, the conversion nature of the coating layer on 316 L steel is confirmed. These values are 73 wt.%, ~17 wt.%, and 9 wt.% for iron, chromium, and nickel, respectively, and shift towards those in the plating bath composition at distances away from the interface. The concentration profiles are produced inside the coating with clear inflection points. It is noteworthy that the inflection points in the three concentration profiles correspond to the same distances from the interface. This is due to the interactions between these elements when they dissolve in the substrate and fill holes in the

conversion/plated coating. The iron content is decreased rapidly so that the concentration at the inflection point drops by three times to 20 wt.%. In contrast, Ni content is increased to reach 8 the value of 0 wt.%. Chromium also follows a similar pattern and, at its inflection point, reaches almost 0.2 wt.%. The study on Cr as an alloying element during the PP approach revealed the need for high currents to enable Cr deposition [36-40]. The current off-time to on-time ratio and the current off-time is not constant, while our work's current density is constant. It is demonstrated that the controlling role of the current could be replaced by that ratio and the current off times. If there is no cathodic current, an acidic bath with surfactant additions can attack the substrate. Range-1 samples with the off-time to the on-time ratio of 2 show a tendency for restrained dissolution of Fe and Cr from the substrate at a constant reserve time. As explained before, it leads to moderate grain growth without hindering nucleation. The mentioned ratio for ranges 2 and 3 tends to unity with noticeable high Cr content extending further inside the coating due to long current-off time. Extremely long current-off times of nearly 10ms (e.g., in range-3) enable the electrolyte to attack and dissolve the constituents.

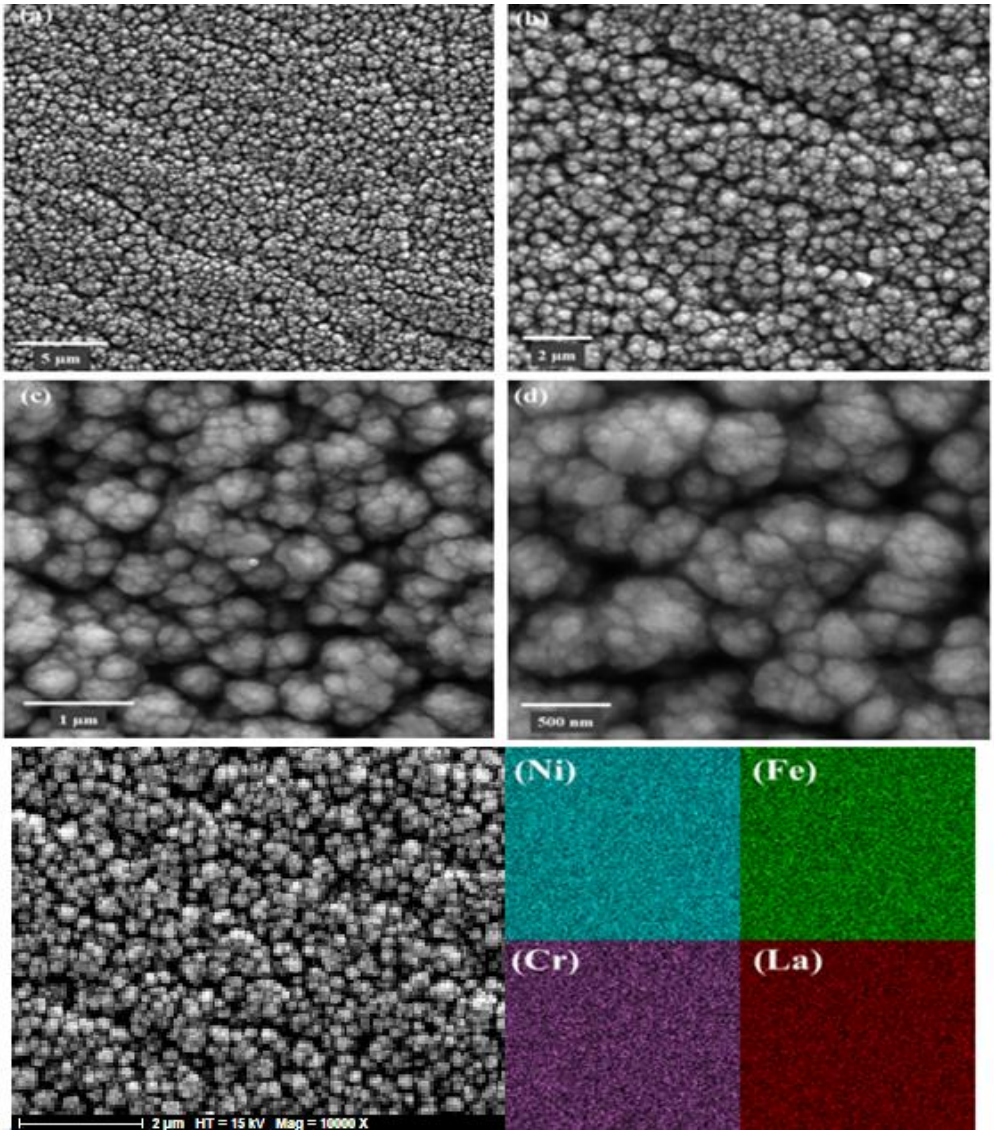

Fig. 3. (a)-(d) SEM images of the coated sample under the range-1 conditions as described in table 3, and (e) the uniformity of element distribution shown in the mapping of the same range

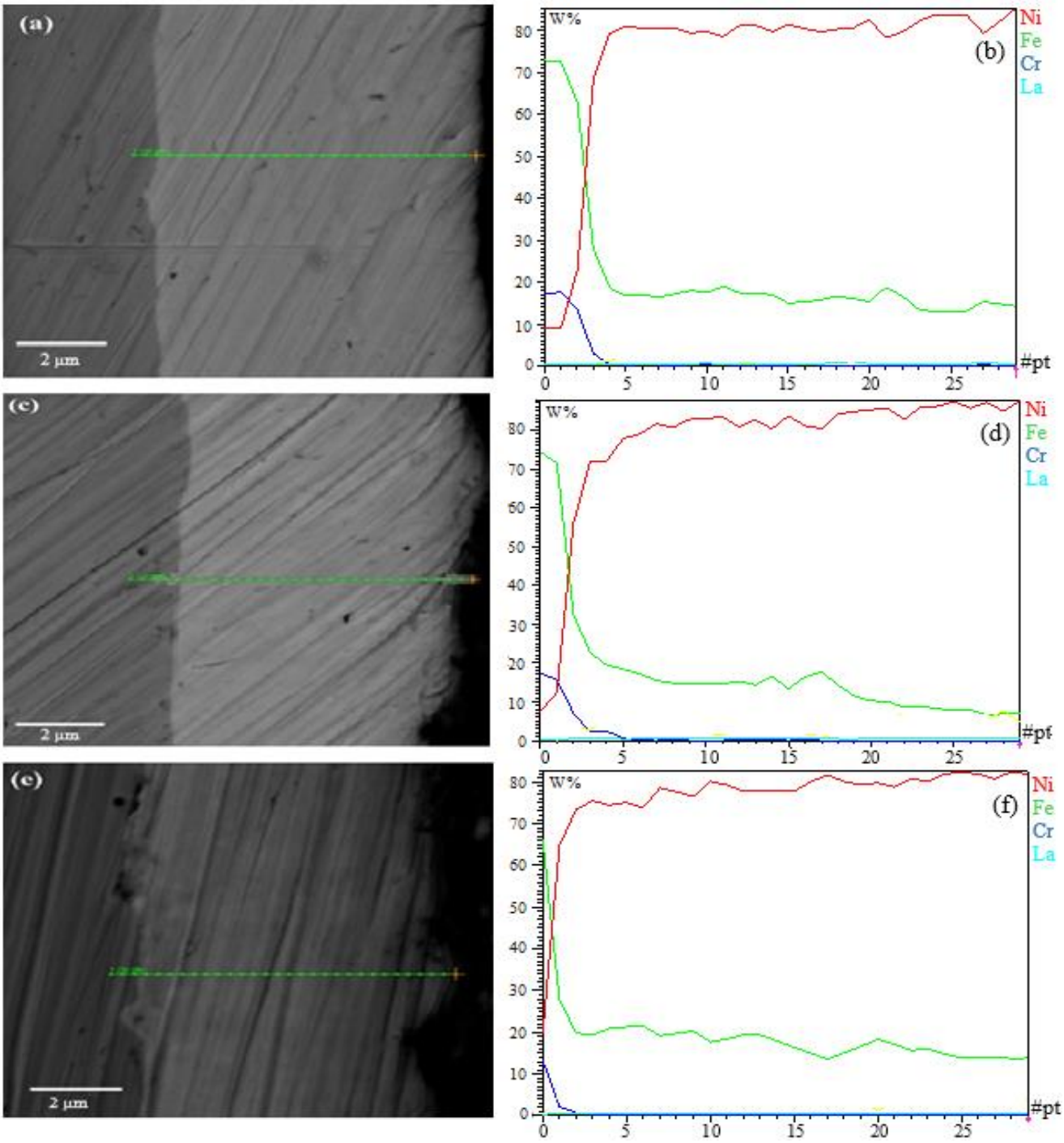

Fig. 4. SEM images of plated coating and the elemental linear scan analysis of the coating thickness. (a) and (b) are samples from range-1, (c) and (d) are samples from range-2, and (e) and (f) are samples from range-3

The experimental conditions, additives such as $LaCl_3.7H_2O$, and complexing agents positively shift the potential of the transition ions and depress the co-deposition of rare-earth elements that affect the deposition mechanism of the coating [28]. SEM images in Fig. 5 reveal that the coating thickness in the three samples created under the ranges 1, 2, and 3 are 6.83, 5.83, and 7.09µm, respectively. The interface of samples formed under range-1 shows no discontinuity and porosity. Therefore, the interface attains excellent adhesion. The range-2 samples demonstrate an acceptable coating quality but less adhesion and cohesion. However, samples of the range-3 plating suffer from a lack of cohesion and adhesion, with a noticeable porosity-filled coating interface. This reflects the poor corrosion performance, particularly when compared with bare SS316L.

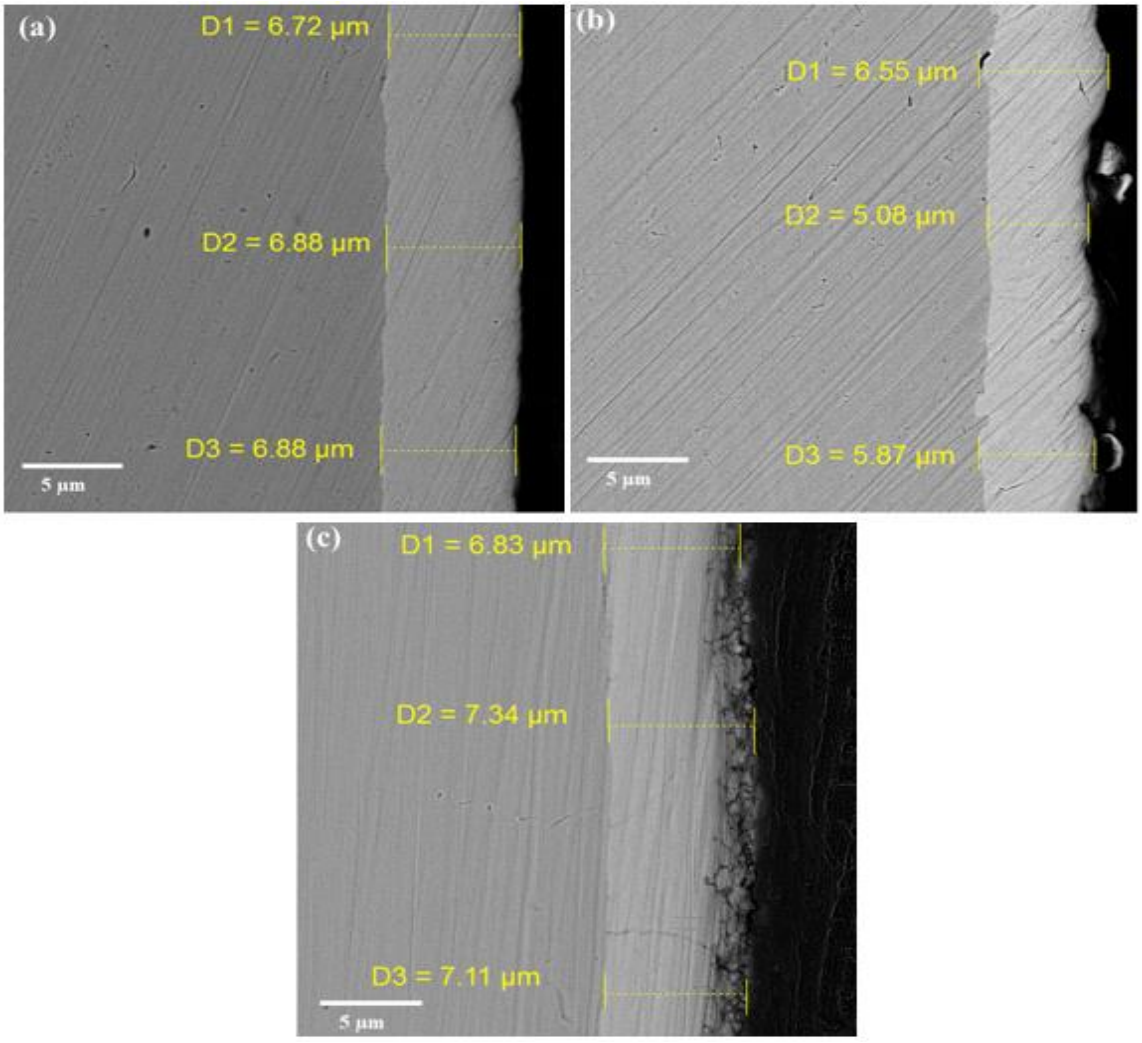

Fig. 5. SEM images of the cross-sections of the coating for samples created under (a) range-1, (b) range-2, and (c) range-3

The Tafel plots of the uncoated and plated sample 1 are shown in Fig. 6, and the numerical results of the polarization curves in Fig. 6 are shown in Table 4. The corrosion currents of the range-1 coated specimen are decreased compared with the bare SS316 indicating an improved resistance to corrosion. The comparative bar chart shown in Fig. 7 contrasts the corrosion current of these samples. It illustrates that the range-1 confers the highest corrosion resistance reducing the corrosion rate by almost 160 times compared to an uncoated sample. The overall improvement in corrosion resistance is attributed to the surface integrity of the passive layer due to chromium oxide formation, surface texture, and grain structure of the coating.

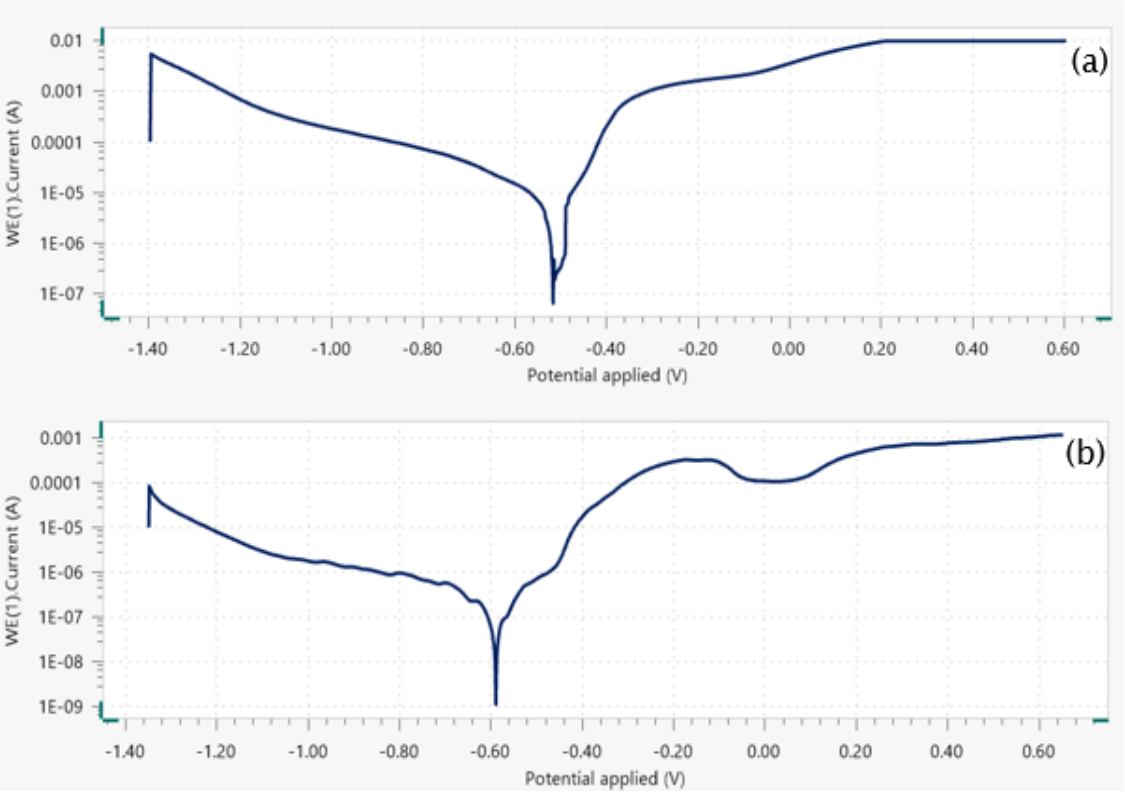

Fig. 6. Polarization diagrams of (a) 316 L steel without coating and (b) coated sample according to range-1 plating, Table 3, and plating specifications of Table 2, for a 1.5% NaCl solution at 50°C.

Table 4. Electrochemical parameters of specimens in 1.5% NaCl solution attained from the polarization test..

β_c(mV/decade)	β_a(mV/decade)	R_p(KΩ.cm^2)	E_{cor}(mV)	I_{cor}(μA.cm^{-2})	Sample
24.285	59.741	250	-580-	0.03	Range-1
25.031	58.170	1.68	-520	4.8	SS.316L

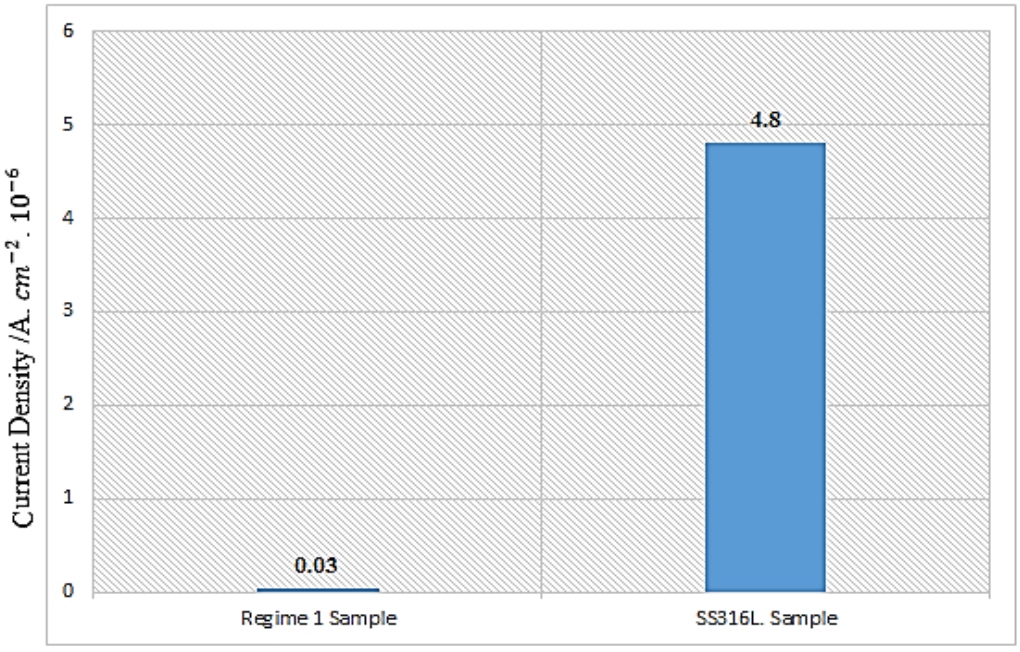

Fig. 7. Comparison between the polarization test results in 1.5% NaCl solution at 50°C from the plated sample under range-1 and bare SS316L.

High corrosion resistance results from Cr-dopped nickel matrix using reverse pulse frequencies with La. It has a pronounced effect on the structure at less than 1g.L^{-1} concentration by enhancing the nucleation

process so that it creates a coherent chloride-resistant structure. Lanthanum dissolves as La^{+3} cations (with their electronic structures) are favorably adsorbed on the surface of the cathode. It disturbs the positive charge balance of the catholyte, which is rebalanced by more Ni^{+2} migration. In fact, the initial adsorption of La^{+3} increases the cathodic current to facilitate the process of nickel ions reduction. The discharge of Ni^{+2} by employing reverse pulse range increases over-potential, which in turn enhances the nucleation of nickel grains. Finally, it results in a fine grain structure [31, 41]. As indicated by the linear scan results of Fig. 4, the amount of lanthanum taken up in the surface layer is very low due to its relatively low concentration in the bath and also its difficult deposition nature. Lanthanum sources like $LaCl_3.7H_2O$ and the reverse pulse condition provide optimal co-deposition to this element within the Ni matrix. The pulse electroplating with the possibility of reverse currents with varying frequency enables the controllability of discharge time and removal time of initial nuclei to achieve desired adhesion, as shown in Fig. 5(a). In fact, a cohesive and adhesive Ni coating with appropriate grain size and capable of forming Cr_2O_3 will exhibit the desired corrosion resistance properties. In contrast to the SS316L and other samples, it is demonstrated in the wide passive region formed in the range-1 sample polarization diagram (Fig. 6).

Excellent properties of lanthanum-dopped nickel coating can mainly be attributed to the three effects of rare-earth elements on the electrochemical depositing process: Firstly, the process of deposition is adsorbing the cation on the surface of a cathode. La is a surface-active element with a rather large atomic radius of 0.1877nm. La^{3+} is more easily adsorbed on the surface of a cathode due to the outer layer of lanthanum's electronic structure. When the plating process begins, Ni^{2+} is reduced on the surface of the cathode. However, La^{3+} does not participate in the reaction. The positive charge loss should be compensated by the new cations (La^{3+}, Ni^{2+}). Therefore, the Ni^{2+} content in the electric double layer decreases while the content of La^{3+} increases. It avoids the provisioning process and reduces Ni^{2+} in the bath. The schematic diagram of this process is demonstrated in Fig. 8. It requires a high over-potential to provide the energy of Ni^{2+} reduction, thus altering the deposition of Ni^{2+} and refining the grain size. Secondly, the over-potential also reduces the hydrogen evolution of Fig. 8, the schematic diagram of the cathode reaction, and the cathode surface. Therefore it reduces the hydrogen embrittlement and pinholes and makes perfect surface integrity. Thirdly, the outermost electronic structure of rare-earth lanthanum makes lanthanum ion adsorbed on the surface of the cathode. The cathodic potential needs to be increased to supply the Ni^{2+} energy reduction, increase the speed of the new crystal nuclei's formation, and then refine the grains [27, 28, 41].

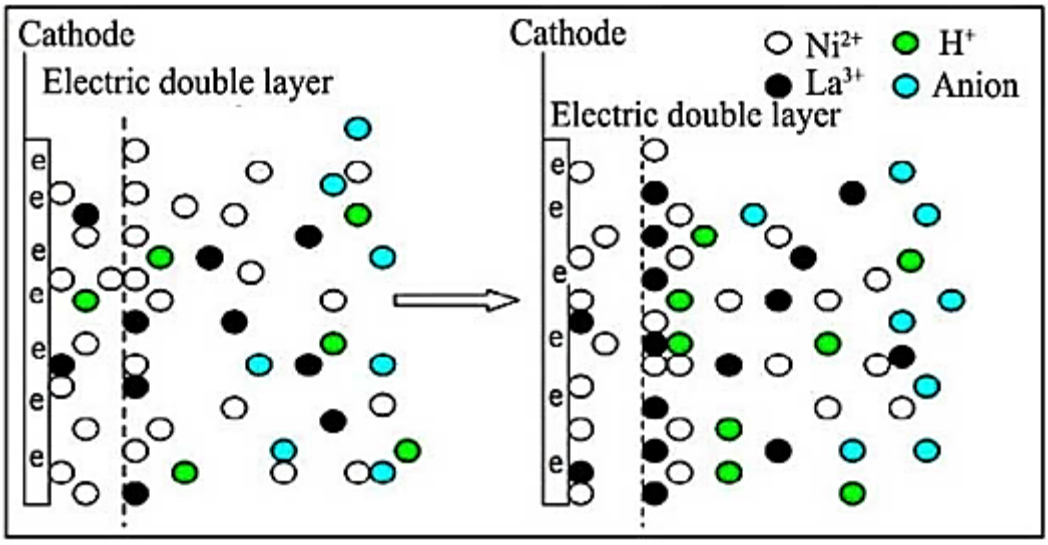

Fig. 8. Schematic diagram of the cathode reaction.

4. Conclusion

- Tertiary high entropy coatings composed of Ni-Fe-Cr-La with controlled metallurgical properties are coated on an SS316L substrate using a hybrid PRP electroplating technique and compounds of lanthanum as modifiers.
- Optimizing the Watts plating bath significantly improves the morphology and corrosion resistance properties of the resulting coating. This is performed by adding useful compounds of saccharin and SDS to increase the quality and fineness of the coating and use the combination of AlCl3 that leads to an increase in the electrical conductivity of the plating bath.

- The polarization test result indicated that the coated sample exhibits ~160 times lower corrosion current than the uncoated SS316L steel when attacked by chloride.
- The final result is a conversion coating with an adhesion due to the penetration zone. This penetration is due to the dissolution and redeposition of the substrate constituents during different phases of PRP electroplating.

References

[1] D. Krouse, N. Laycock, C. Padovani, "Modelling pitting corrosion of stainless steel in atmospheric exposures to chloride containing environments", Corrosion Engineering, Science and Technology, Vol. 49, No. 6, 2014, pp. 521-528.

[2] B. Lorsbach, E. Schmitz, "Influence of test parameters of potentiodynamic current density measurements on the determination of the pitting corrosion resistance of austenitic stainless steels", Materials and Corrosion, Vol. 69, No. 1, 2018, pp. 37-43.

[3] G. Bai, S. Lu, D. Li, Y. Li, "Influences of niobium and solution treatment temperature on pitting corrosion behaviour of stabilised austenitic stainless steels", Corrosion Science, Vol. 108, 2016, pp. 111-124.

[4] N.T Nga, T. Shinohara, T.H. Le, "Effects of Environment Factors on Stress Corrosion Cracking of Austenitic Stainless Steels in Atmospheric Environments", Zairyo-to-Kankyo, Vol. 66, No. 6, 2017, pp. 209-213.

[5] H.S Klapper, J. Stevens, G. Wiese, "Pitting Corrosion Resistance of CrMn Austenitic Stainless Steel in Simulated Drilling Conditions—Role of pH, Temperature, and Chloride Concentration", Corrosion, Vol. 69, No. 11, pp. 1095-1102.

[6] B. R. Tzaneva, M. H. Loukaycheva, L. B. Fachikov, L. Ts. Jekova, " Effect of chloride ions on corrosion behaviour of austenitic nickel and nickel free stainless steels in phosphoric acid solutions", Corrosion Engineering, Science and Technology, Vol. 50, No. 8, 2015, pp. 568-578.

[7] H.S Klapper, C. Menendez, S. Jesse, "Pitting Corrosion Resistance Influencing Corrosion Fatigue Behavior of an Austenitic Stainless Steel in Chloride-Containing Environments", Corrosion, Vol. 76, No. 4, 2020, pp. 398-410.

[8] R. Yamanoglu, E. Fazakas, F. Ahnia, D. Alontseva, F. Khoshnaw, "Pitting Corrosion behaviour of Austenitic Stainless-Steel Coated on $Ti_6A_{l4}V$ Alloy in Chloride Solutions", Advances in Materials Science, Vol. 21, No. 2, 2021, pp. 5-15.

[9] R. T. Loto, "Data on the Corrosion Resistance and Polarization Behaviour of Lean Austenitic and Ferritic Stainless Steels in Neutral Chloride Media", Oriental Journal of Chemistry, Vol. 35, No. 3, 2019, pp. 1138-1142.

[10] M.H. Jang, J.Y. Kang, J.H. Jang, T.H. Lee, C. Lee, "Hot deformation behavior and microstructural evolution of alumina-forming austenitic heat-resistant steels during hot compression", Materials Characterization, Vol. 123, 2017, pp. 207-217.

[11] D.B Park, S.M Hong, K.H Lee, M.Y Huh, J.Y Suh, S.C Lee, WS Jung, "High-temperature creep behavior and microstructural evolution of an $18Cr_9Ni_3CuNbVN$ austenitic stainless Steel", Materials Characterization, Vol. 93, 2014, pp. 52-61.

[12] L. Liu, S. Wu, Y. Chen, et al, "Oxidation behavior of RE-modified nickel-based superalloy between 952℃ and 1150℃ in air. Transactions of Nonferrous", Metals Society of China, Vol. 26, 2016, pp. 1163-1169.

[13] H.T Mallikarjuna, W.F Caley, N.L Richards, "Oxidation Kinetics and Oxide Scale Characterization of Nickel-Based Superalloy IN738LC at 900°C", Journal of Materials Engineering & Performance, Vol. 26, 2017, pp. 1-9.

[14] Z. Zheng, S. Wang, J. Long, J. Wang, K. Zheng, "Effect of Rare Earth Elements on High Temperature Oxidation Behavior of Austenitic Steel", Corrosion Science, Vol. 164, 2020, pp. 108-155.

[15] S. R. J Saunders, J. R. Nicholls, "Coatings and surface treatments for high temperature oxidation resistance", Metal Science Journal, Vol. 5, 2013, pp. 780-798.

[16] A. Karimi, R. Soltani, M. Ghambari, et al, "High temperature oxidation resistance of plasma sprayed and surface treated YSZ coating on Hastelloy X", Surface & Coatings Technology, Vol. 321, 2017, pp. 378-385.

[17] H. Liu, X. Zhang, Y. Jiang, et al, "Microstructure and high temperature oxidation resistance of in-situ synthesized TiN/Ti_3Al intermetallic composite coatings on Ti_6Al_4V alloy by laser cladding process", Journal of Alloys & Compounds, Vol. 670, 2016, pp. 268-274.

[18] W. Hansal, "Pulse plating as a core technology of surface finishing in the twenty-first century: review of the Eighth European Pulse Plating Seminar", Transactions of the IMF, Vol. 96, No. 3, 2018, pp. 115-117.

[19] J.-C. Puippe, "Unconventional pulse plating parameters for surface area measurement applications", Transactions of the IMF, Vol. 99, No. 1, 2021, pp. 17-22.

[20] C. Y. Chen, C. C. Hsu, U. W. Liu, C. A. Huang, "Characterization of Cr-Ni Multilayers from Chromium(III)-Nickel(II) Baths Using Pulse-Current Plating", ECS Transactions, Vol. 2, No. 3, 2019, pp. 413-418.

[21] J. Zhang, C. Su, X. Chen, H. Liu, L. Zhang, "First-principles study on pitting corrosion of Al deoxidation stainless steel with rare earth element (La) treatment", Materials Today Communications, Vol. 27, 2021, pp. 102-114.
[22] Y. C. Yu, S. H. Zhang, S. B. Wang, "Effects of Cerium on the Inclusions and Pitting Corrosion Behavior of 434 Ferritic Stainless Steel", High Temperature Materials and Processe, Vol. 37, No. 9, 2018, pp. 807-814.
[23] W. Zheng, X. Yan, S. Xiong, G. Wang, G. Li, "Pitting corrosion behavior of cerium treated HSLA steel induced by sulfide inclusions in 3.5 wt% NaCl solution", Journal of Rare Earths, Vol. 39, No. 3, 2021, pp. 348-356.
[24] N. Yin, C.L. Jing, H.B Li, R.S Chu, B. Chen, "Effect of Rare Earth Elements on the Inclusion Behavior in Low Alloy Structural Steel", Materials Science Forum, Vol. 944, 2019, pp. 364-372.
[25] X. Cheng, Z. Jiang, D. Wei, et al, "Characteristics of oxide scale formed on ferritic stainless steels in simulated reheating atmosphere", Surface & Coatings Technology, Vol. 258, 2014, pp. 257-267.
[26] Q. Wang, Q. Yao, Y. Wang, et al, "Research on the oxidation behavior of novel γ/γ'-strengthened Co-9Al-10W alloys combined with chromium and rare earth elements", Journal of Materials Research, Vol. 31, 2016, pp. 3332-3344.
[27] X. Xing, H. Wang, P. Lu, Z. Han, "Influence of rare earths on electrochemical corrosion and wear resistance of RE–Cr/Ti pack coatings on cemented 304 stainless steel", Surface And Coating Technology, Vol. 291, 2016, pp. 151-160.
[28] C. Liu, R.I Revilla, Z. Liu, D. Zhang, X. Li, H. Terryn, "Effect of inclusions modified by rare earth elements (Ce, La) on localized marine corrosion in Q460NH weathering steel", Corrosion Science, Vol. 129, 2017, pp. 82-90.
[29] D. Xueliang, W. Deren, Z. Yangqing, " Effect of mechanical attrition on microstructure and properties of electro-deposition coatings on NdFeB", Journal of Rare Earths, Vol. 32, No. 9, 2014, pp. 867-873.
[30] J. Guo, L. Bingwen, H. Dingding, C. Xiufang, et al, "Influence of rare earths addition on residual stress of Fe-based coating prepared by brush plating technology", Journal of Rare Earths, Vol. 34, 2016, pp. 336-345.
[31] M.A.M. Ibrahim, R.S. Bakdash, "New non-cyanide acidic copper electroplating bath based on glutamate complexing agent", Surface Coating Technology, Vol. 282, 2015, pp. 139–148.
[32] Brian Hinderliter, "Response of Electrochemical Impedance Spectroscopy to Evolving Coating Systems", ECS. Transactions, Vol. 41, No. 15, 2019, pp. 39-51.
[33] N. Imaz, M. Ostra, M. Vidal, J.A. Díez, M. Sarret, E. García-Lecina, "Corrosion behaviour of chromium coatings obtained by direct and reverse pulse plating electrodeposition in NaCl aqueous solution", Corrosion Science, Vol. 78, 2014, pp. 251-259.
[34] M.S. Chandrasekar, Malathy Pushpavanam, "Pulse and pulse reverse plating—Conceptual, advantages and applications", Electrochimica Acta, Vol. 53, No. 8, 2008, pp. 3313-3322.
[35] G. Wang, D. Li, Y. Zuo, Y. Tang, X. Zhang, X. Zhao, "The Improvement of Hardness and Corrosion Resistance of Electroplated Pd-Ni Film on 316L Stainless Steel by $CeCl_3$", Coatings, Vol. 10, No. 2, 2020, pp. 161-171.
[36] R. Gupta, A. Sharma, U. Pandel, L. Ratke, "Effect of stirring speed on microstructure of A356 alloy cast through rheometal process", International Journal of Materials Research, Vol. 108, No. 8, 2017, pp. 648-655.
[37] P. Marcolin, M. Longhi, L. P. Zini, B. Proença, et al, " Influence of the pH and Stirring Speed of the Electrodeposition Bath in the Performance of Zinc and Zinc-Nanocomposite Coatings", Materials Science Forum, Vol. 899, 2017, pp. 283-288.
[38] S. An, Y.I Kim, H.S Jo, M.W Kim, M.W Lee, A.L Yarin, et al, "Silver-decorated and palladium-coated copper electroplated fibers derived from electrospun polymer nanofibers", Chem. Eng. J., Vol. 327, 2017, pp. 336–342.
[39] Y. Kamimoto, S. Okura, T. Hagio, T. Wada, H. Tanaka, et al, "Nickel–carbon composite plating using a Watts nickel electroplating bath. SN Applied Sciences", Vol. 2, No. 2, 2020, pp. 1-6.
[40] M. Mohammadi, M. Ghorbani, "Wear and corrosion proper- ties of electroless nickel composite coatings with PTFE and/or MoS2 particles", J. Coat Technol Res, Vol. 8, 2011, pp. 527–533
[41] W. Dan, Y. Cheng, J. Huiming, J. Zhang, J. Gao, "Influence of LaCl3 addition on microstructure and properties of nickel-electroplating coating", Journal of Rare Earths, Vol. 31, No. 2, 2013, pp. 209-214.

JMATPRO	Journal of Advanced Materials and Processing 9 (3): 35-46, Summer 2021 http://jmatpro.iaun.ac.ir 20.1001.1.2322388.2021.9.3.3.3

Research Paper

Palladium-Cobalt on Reduced Graphene Oxide as an Electro-catalyst for Ethylene Glycol Oxidation in Alkaline Medium: Synthesis and Electrochemical Performance

Hamid Reza Asgari[1], Somayeh Majidi[2*]

1. Department of Chemical Engineering, Health, Safety and Environment, Najafabad Branch, Islamic Azad University, Najafabad, Iran.

2. Department of Chemistry, Najafabad Branch, Islamic Azad University, Najafabad, Iran.

ARTICLE INFO

Article history:

Received 2 May 2021
Accepted 6 July 2021
Available online 1 August 2021

Keywords:
Alkaline Medium, Catalyst Activity
Electro-oxidation Reaction
Ethylene Glycol
Graphene Oxide
Pd-Co/rGO Electro-catalyst

ABSTRACT

In this study, Pd-Co alloying nanoparticles supported on reduced graphene oxide (rGO) were synthesized and characterized by various techniques such as field emission scanning electron microscopy (FE-SEM), energy-dispersive X-ray (EDX), X-ray diffraction (XRD), and Raman spectra. The prepared Pd-Co/rGO nanoparticle was used as the electro-catalyst for the ethylene glycol (EG) oxidation reaction in the alkaline medium. The activity of Pd-Co/rGO was evaluated in the half-cell by cyclic voltammetry (CV) technique. Results demonstrate that Pd-Co/rGO electro-catalyst has higher performance compared to simple alloyed-based Pd electro-catalysts for EG electro-oxidation in alkaline media. Pd-Co/rGO catalyst showed well-defined peaks for the EG oxidation reaction after 150 CV cycle. This result indicated that Pd-Co/rGO electro-catalyst is still active in EG oxidation reaction even after 150 CV cycles, suggesting high poisoning toleration of Pd-Co/rGO electro-catalyst in the EG oxidation reaction. The results of electrochemical experiments indicated that Pd-Co/rGO could be practically used as the high-efficiency anode electro-catalyst for the EG oxidation reaction in alkaline media.

Citation: Asgari, H.R., Majidi, S., (2021), Palladium-Cobalt on Reduced Graphene Oxide as an Electro-catalyst for Ethylene Glycol Oxidation in Alkaline Medium: Synthesis and Electrochemical Performance, 9 (3), 35-46. Dor: 20.1001.1.2322388.2021.9.3.3.3

* **Corresponding Author**
E-mail address: s.majidi@pmt.iaun.ac.ir

1. Introduction

Direct alcohol fuel cells (DAFCs) represent one of the most promising renewable and clean energy devices found in portable, stationary, and mobile applications. DAFCs employ a wide range of liquid fuels such as mono-valent alcohols and aliphatic diols. Ethylene glycol (EG) as an alcoholic fuel has the following advantages: 1) renewable bio-fuel from the biomass fermentation, 2) low toxicity compared to methanol, 3) high theoretical mass-energy density (EG: 5.2 kWh kg^{-1}), 4) high-efficiency energy conversion, 5) easy to store and carry and 6) cheap and wide sources [1-3]. Therefore, developing such green, low-cost, and high-efficiency anodic fuel is desirable for direct EG fuel cells (DEGFCs).

The development of catalysts with high electro-catalytic activity for DEGFCs application is a central issue to accelerate the clean energy technology in an affordable manner [4, 5]. Due to the unique chemical, physical and electronic properties of Pt, it is one of the most common catalysts used for alcohol oxidation in DEGFCs. However, Pt and Pt-based catalysts easily adsorb intermediates of alcohols oxidation (e.g., CO), and their electro-catalytic activity is reduced rapidly [6]. Moreover, Pt is a precious metal with limited global reserves, resulting in considerable efforts to lower the Pt loading or even replace it with less expensive materials [7].

In general, three kinds of electro-catalyst (i.e., Pt-based, Pd-based and Au-based catalysts) have been regarded as electro-catalysts for the electro-oxidation of EG in alkaline media as follow: (i) Pt-based catalysts such as Pt-Ag nanotubes [8], Pt-CeO_2/C [9, 10], Pt-Co/rGO [11], Pt-Pd/rGO [12], Au-Pt deposited on Ni nano-particles [13], (ii) Pd-based catalysts such as Pd-M bimetallic electro-catalysts (M: Ni or Sn) supported on sulfonated multi-walled carbon nanotubes [14], Pd-In [15], Pd-Ni decorated manganite [16], Pd-(Ni-Zn)/C [17], FeCo-Fe-Pd/C [18], oxide (CeO_2, NiO, Co_3O_4 and Mn_3O_4)-promoted Pd/C [19, 20], (iii) Au-based catalysts such as oxide (CeO_2, Fe_2O_3 and RuO_2)-promoted Au/C [21], Pt-Au [22], Au-Bi/C, Pd-Au/C and Pd-Au-Bi/C [23]. The past studies on the electro-catalysts for EG electro-oxidation indicated that the electro-catalytic activity, stability, and durability of electro-catalysts could be further improved with binary alloy catalysts. The addition of the second transition non-precious metals, such as Co, forms a binary alloy with Pd, resulting in altering the electronic structures of the two metals (by shifts in the binding energy in X-ray photoelectron spectroscopy (XPS)). Furthermore, the surface segregation phenomenon of alloying leads to the suitable arrangement of the Co next to the Pd surface atoms [24, 25]. Apart from electro-catalyst alloying, the employment of reduced graphene oxide (rGO) as electro-catalyst support helps the effective dispersion of nano-catalyst and reduction in CO poisoning, this activates the functional sites of the catalyst due to its hydrophilic nature. In addition, rGO has many merits of a large theoretical specific surface area, high intrinsic mobility, and high thermal and electrical conductivity [26, 27].

To the best of our knowledge, Pd-Co/rGO electro-catalyst applied for EG oxidation reaction has not been reported so far. However, it is presented in the following articles that Pd-Co/rGO exhibits higher electro-catalytic activity in the oxidation of ethanol, formic acid, and methanol compared with the Pd electrocatalyst. Rostami et al. [28] synthesized the Pd-Co/rGO electrocatalyst, which had electrochemical catalytic ability toward the ethanol electro-oxidation in the alkaline medium. For Pd-Co/rGO, it was evidenced that the onset potential (E_s) and the peak current density (j_P) are 160 mV lower and 2.5 times higher than that of the Pd/C electrocatalyst, respectively. Results determined that the anti-poisoning ability of Pd-Co is improved by rGO as a catalyst support.

Duck et al. [29] prepared Pd-Co nano-structures decorated on graphene (Gr) as an electrocatalyst toward the formic acid electro-oxidation. The Pd-Co/Gr increased j_P to 7 times more than Pd/C. In addition, the E_s and peak potential (E_P) for Pd-Co/Gr electrocatalyst indicated a negative shift in comparison to Pd/C. The chronoamperometry (CA) experiment showed that the stability of the Pd-Co/Gr catalyst was significantly upgraded. Wang et al. [30] described a method for synthesizing carbon-supported Pd–Co core-shell nano-particles. PdxCo@Pd/C had a high activity comparable to Pt/C, exhibiting a high tolerance of PdxCo@Pd/C toward methanol in the oxygen reduction reaction. Wang et al. [30] also described a method for synthesizing carbon-supported Pd–Co core-shell nanoparticles. PdxCo@Pd/C had a high activity comparable to Pt/C, exhibiting a high tolerance of PdxCo@Pd/C toward methanol in the oxygen reduction reaction. Wang et al. [31] provided Pd-Co nano-particles supported on rGO sheets. Electrochemical measurements confirmed that the Pd-Co/rGO exhibits excellent performance for ethanol and methanol electro-oxidation in the alkaline medium with slightly decreased activity but significantly improved stability compared to Pd/rGO.

In this paper, Pd-Co alloy nanoparticles based on rGO were synthesized and employed as a promising candidate for the electrocatalyst toward EG oxidation in the alkaline medium. This electrocatalyst was prepared through a simple co-reduction process and characterized using field emission scanning electron

microscope (FE-SEM), energy-dispersive X-ray (EDX), X-ray diffraction (XRD) technique, and Raman spectra. Then, Pd-Co/rGO nanoparticles were employed as the electrocatalyst for EG electro-oxidation in the alkaline electrolyte. The electrochemical performance of the Pd-Co/rGO electrocatalyst was evaluated by CV and CA techniques. Since the Pd-Co/rGO electrocatalyst showed high electro-catalytic activity in EG electro-oxidation, it would have more promising applications in DEGFCs.

2. Experimental

2.1. Materials Required

To synthesized the Pd-Co/rGO electrocatalyst, the used chemicals were powdered graphite, $PdCl_4$ (99.9%, Merck), $NaNO_3$ (Indian), H_2O_2 (30 wt.%, Merck), $Co(CH_3COO).5H_2O$ (98%, Alfa Aesar,), H_2SO_4 (98%, Merck), HCl (98%, Merck) $KMnO_4$ (98%, Merck), NaOH (Indian, ~98%), N_2H_4 (5 wt.%, Merck), ethanol (98%, Merck) and EG (98%, Merck). To prepare the catalyst ink, nafion 117 (10 wt.%, Aldrich) and isopropyl alcohol (20 v.%, Merck) were used. All the experiments were performed using de-ionized (DI) water.

2.2. Graphene Oxide (GO) and Pd-Co/rGO Synthesis

GO was synthesized through modified Hummer's method [32]. In summary, 1g of graphite powder, 1 g $NaNO_3$ was added in 40 mL H_2SO_4 while stirring. After 2 h, the mixture was placed into ice bath and 6 g of $KMnO_4$ was gradually added to it. Then, the mixture was kept at 35°C under stirring for 24 h. 10 mL of H_2O_2 was added instantly to terminate the reaction. Finally, the suspension was filtered and washed with HCl (5 v.%) followed by washing with DI water for several times until reaching the neutral pH.

Pd-Co/rGO nano-particles with 1:1 Pd to Co metal ratio were synthesized using an in situ procedure as follows: 25 mg of synthesized GO was mixed in 25 mL of EG and ultra-sonicated for 30 min to obtain highly exfoliated GO homogenous dispersion. The calculated amount of $PdCl_4$ and $Co(CH_3COO)_2.5H_2O$ were dissolved in a few amount of ethanol and EG solvents, respectively. After that the metal salts were gradually added into the GO solution followed by stirring for 12 h. 0.25 g of NaOH was dissolved in 5 mL of N_2H_4 and added drop wise to the mixture followed by stirring for 1 h under N_2 atmosphere. Then the mixture was put in an oven at 200 °C for 3 h. After self-cooling to the room temperature, the resulting sample was collected by super magnet and washed several times with DI water and ethanol until reaching the neutral pH. Then, the synthesized catalyst was dried in an oven at 45 °C.

2.3. Morphological and Electrochemical Characterization

The surface morphology of GO and Pd-Co/rGO was investigated by FE-SEM (Mira III, TE-Scan, Czech Republic) in EDX mode. Raman spectrum was recorded between 500 and 3000 cm^{-1} on a Raman spectrometer (Takram P50C0R10, Teksan, Iran), using a 532 nm Nd: YAG laser at 10 mW power. XRD analysis was done to record the structural information by calculating crystallite size and lattice parameters in the range of 20 to 80 at the rate of 3 per minute. A diffractometer (PW3040, Philips, Netherlands) with a Cu K_α X-ray source was used for XRD. The electrochemical performance of the synthesized electrocatalyst was investigated through a conventional three-electrode electrochemical cell with a potentiostat–galvanostat workstation (SAMA, Iran) at room temperature. A glassy carbon (GC), platinum foil and Ag/AgCl in saturated KCl were used as the working electrode, counter electrode and reference electrode, respectively.

In order to prepare the working electrode, the GC electrode surface (area: 0.0314 cm^2) was carefully polished with the alumina powder on a polishing cloth, cleaned by sonication in ethanol and DI water, and allowed to dry at room condition. The catalyst ink was prepared by well-dispersing 1 mg of powdered catalyst in a solution of 0.05 mL of nafion solution in isopropyl alcohol (5 wt.%), 0.5 mL of DI water and 0.5 mL of ethanol. The required amount of the catalyst ink was pipetted on the pre-polished GC electrode surface and dried at room temperature. The catalyst loading on the pre-polished GC electrode was 0.033 mg cm^{-2}. All electrochemical measurements were carried out in the basic solution containing 1M KOH and 1M EG. For the electrochemical measurements, CV and CA were performed. CV test was carried out by scanning the potential between -0.7 and 0.4 V *vs.* Ag/AgCl electrode with the scan rate of 50 mV s^{-1}. CA test was also carried out at the potential of -0.1 V. All potential values in this article have been reported *vs.* Ag/AgCl potential.

3. Results and Discussions

3.1. Morphological Investigation of Synthesized GO

The prepared GO was characterized by the Raman spectrum (Fig. 1) and FE-SEM images (Fig. 2). The Raman Spectrum of GO is determined by a G band at ca. 1605 cm^{-1} and a D band at 1353 cm^{-1} which correspond to the E_{2g} phonon mode of the sp^2 C atoms and breathing mode of κ point phonons of A_{1g} symmetry, respectively [33]. In other words, the D band is an indication of disorder, resulting from

certain defects such as vacancies, grain boundaries and amorphous carbon species [34]. As shown in Fig. 1, D and G bands of GO were observed at 1371 cm^{-1} and 1597 cm^{-1}, respectively. The I_D/I_G ratio of the Raman spectrum of GO indicates the degree of structural defects. This ratio of synthesized GO was 0.85 indicating that synthesized GO contains little defects. The band was observed in the range of 2500 cm^{-1} to 3000 cm^{-1} is known as the 2D band, which is an indicator of the number of GO layers [34]. As shown in Fig. 1, the 2D band is observed to be broadened, attributed to the fact that the prepared GO contains few layers.

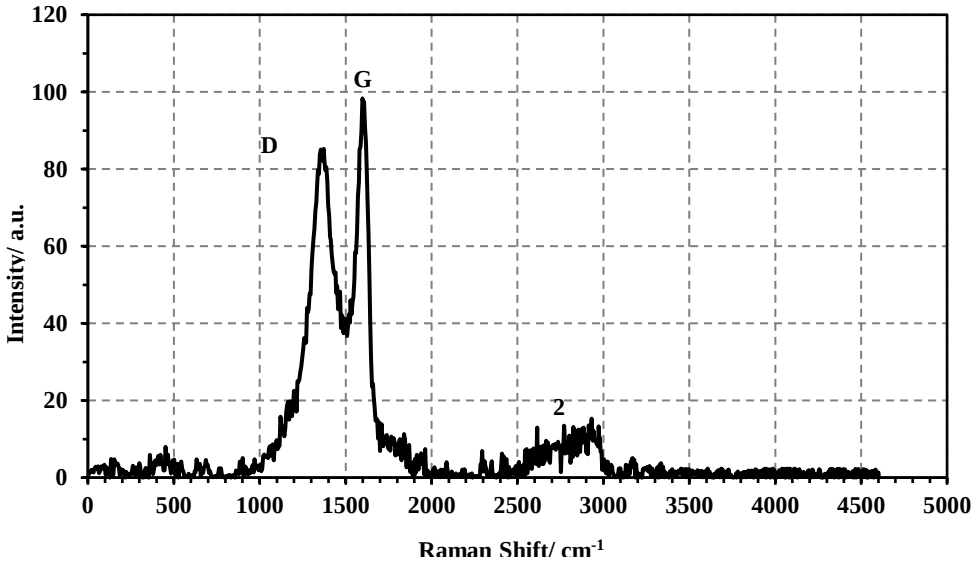

Fig. 1. Raman spectrum of GO (Graphene oxide)

Fig. 2 shows FE-SEM images of GO with different scales. These images have well defined three-dimensional GO sheets, forming a network that resembles a loose sponge-like structure.

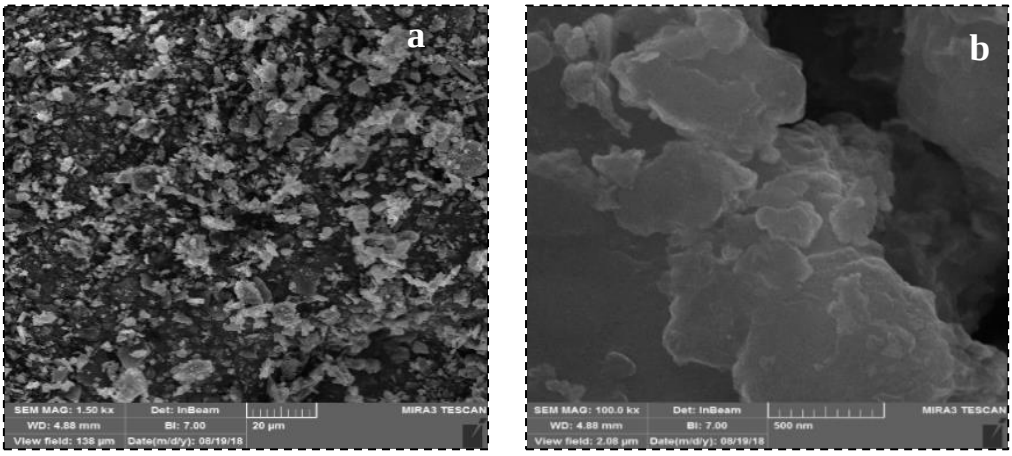

Fig. 2. FE-SEM images of GO with different scales a (20 μm and b) 500 nm

3.2. Structural Investigation of Synthesized Pd-Co/rGO Electrocatalyst

The XRD pattern of Pd-Co/rGO is shown in Fig. 3. The XRD pattern shows the peaks at 2θ of 40°, 46.86°, 67.73°, 82.36° and 86.4° are associated with the (111), (200), (220), (311) and (222) crystal planes of Pd, respectively, featuring a cubic phase with a= 0.39 nm). Compared to the cubic phase of pure Pd (JCPDS 01-087-0643), each peak of the XRD pattern (Fig. 3) are shifted to higher angles, suggesting the alloying of Pd and Co in the bimetallic Pd-Co/rGO electrocatalyst, and indicating a lattice contraction, which is caused by the incorporation of the small Co into the Pd structure [35].

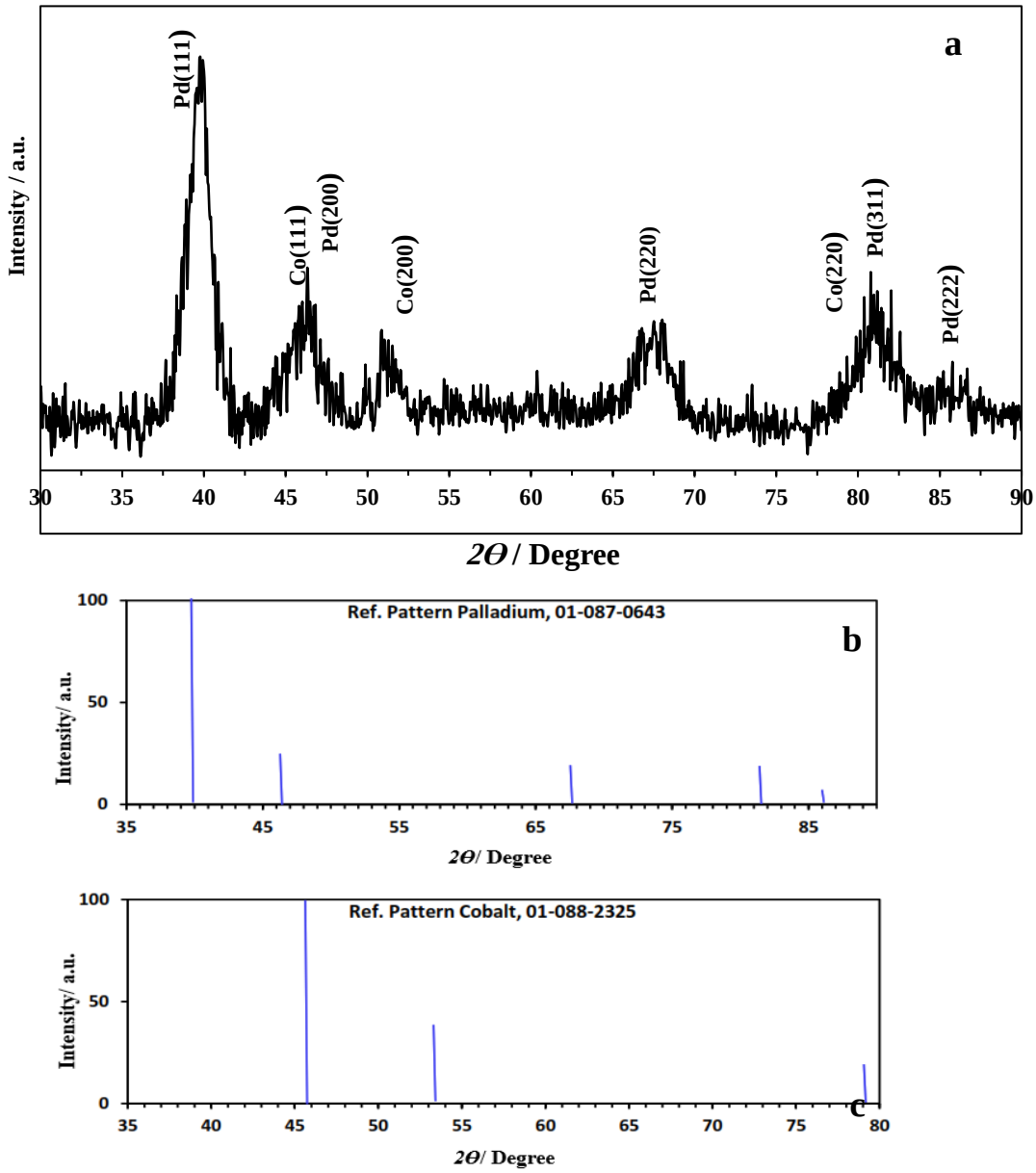

Fig. 3. XRD pattern of (a) Pd-CO/rGO, (b) Pd and (c) Co

As shown in Fig. 3, the characteristic peak was observed at 2θ of 51.18º, which is related to (200) crystal plane of Co cubic phase (JCPDS 01-087-0641, a=0.34 nm). It is expected that there are the Co (111) and Co (220) peaks at the range of 44º-48º and 79º-83º. According to the XRD pattern, the average nanoparticle crystallite size (D) was calculated by the Scherrer Eq. (1):

$$D = \frac{0.9\,\lambda}{\beta}\cos\theta \qquad (1)$$

where λ, β and θ are the wavelength of X-ray (λ for Cu Kα=0.154 nm), additional broadening and diffraction angle, respectively. β can be obtained by Eq. (2):

$$\beta = \mathrm{FWHM} \times \frac{3.1416}{180} \qquad (2)$$

where, FWHM is full width at half maximum reflection. By using Eq. (1) and Eq. (2), the average size of nano-particles was approximately 30 nm. Because of weak intensity belonging to carbon diffraction peaks, they were not observable in the XRD pattern of Pd-Co/rGO. The chemical composition of the synthesized electro-catalyst is determined by EDX analysis (Fig.4).

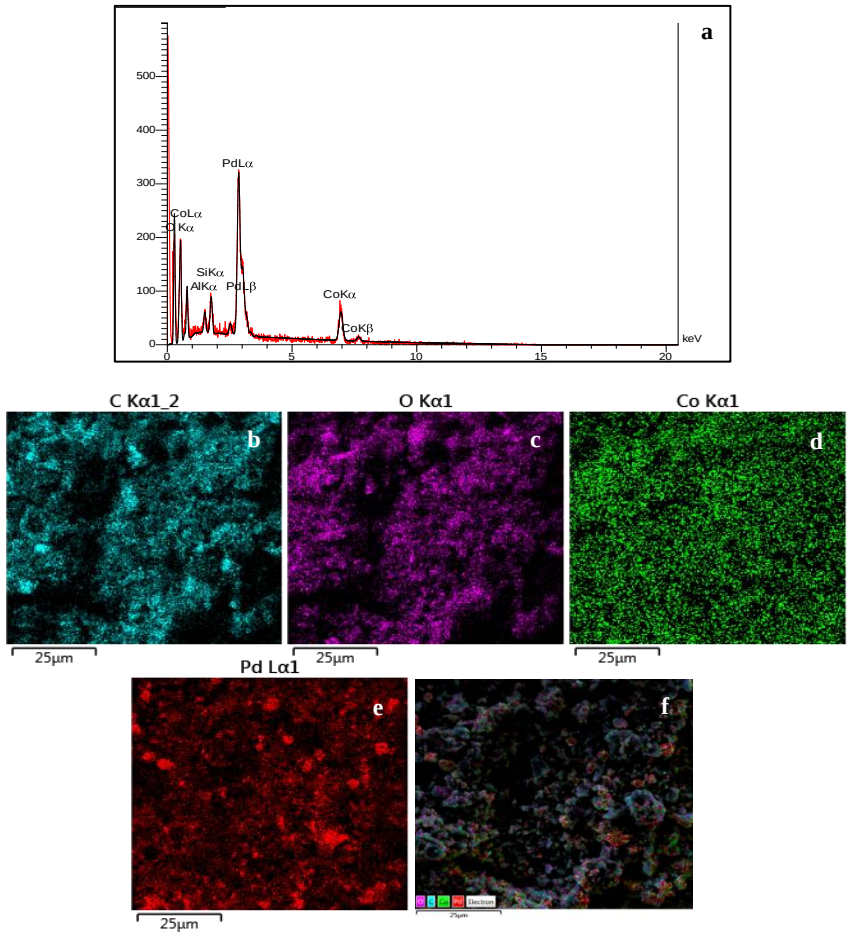

Fig. 4. a) EDX analysis, elemental mapping images of b) C, c) O, d) Co, e) Pd and f) all elements

Fig. 4(a) indicates the EDX spectrum of Pd-Co/rGO. Results indicate that the synthesized catalyst contains Pd, Co, O, and C elements. As shown in the inset of Fig. 4(a), C and Co have the most and less weight or atomic percentage compared to other elements, respectively. According to the weight percentage of Pd and Co, it is concluded that the molar ratio of Pd to Co is equal to 1.3. Fig. 4(b)-(d) shows the EDX mapping images of C, O, Pd, Co, and all these elements. The images confirmed the mentioned elements and showed their homogenous distribution. Fig. 5 shows FE-SEM images of synthesized catalysts in different scales. FE-SEM images indicate the 3D structure morphology of the electrocatalyst. Homogenous dispersion of electrocatalyst on rGO occurred without significant agglomeration. The average particle size was 30 nm, close to that estimated by XRD.

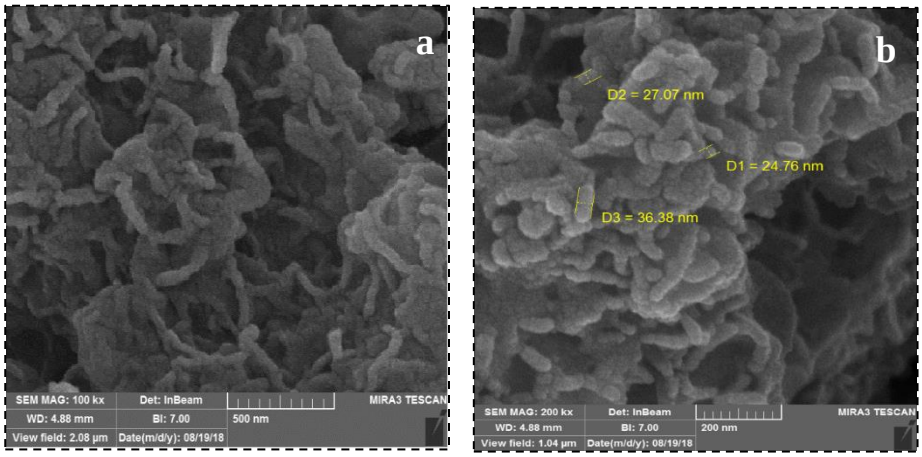

Fig. 5. FE-SEM images of Pd-CO/rGO electrocatalyst with different scales a) 500 nm and b) 200 nm

3.3. Electrochemical Characterization of Synthesized Pd-Co/rGO Electrocatalyst

The EG electro-oxidation reaction on the Pd-Co/rGO surface was investigated by the CV experiment. Fig. 6 shows the cyclic voltammogram of Pd-Co/rGO in the solution containing 1M KOH and 1M EG at room temperature. The EG oxidation peak can be clearly observed in Fig. 6. It can be concluded that EG oxidation on the Pd-Co/rGO surface is performed in the forward scan at -0.09V and reduction of not-oxidized carbonaceous species can be obviously observed with a peak position at around -0.35V in the reverse scan. Table 1 indicates the electrochemical parameters such as E_s, forward anodic peak potential (E_p), j_p and specific peak current density (Sa_p) of the EG oxidation reaction on the Pd-Co/rGo electrocatalyst compared to Pd-based and Pt-based electrocatalysts as reported in the literature, previously [12, 14, 20].

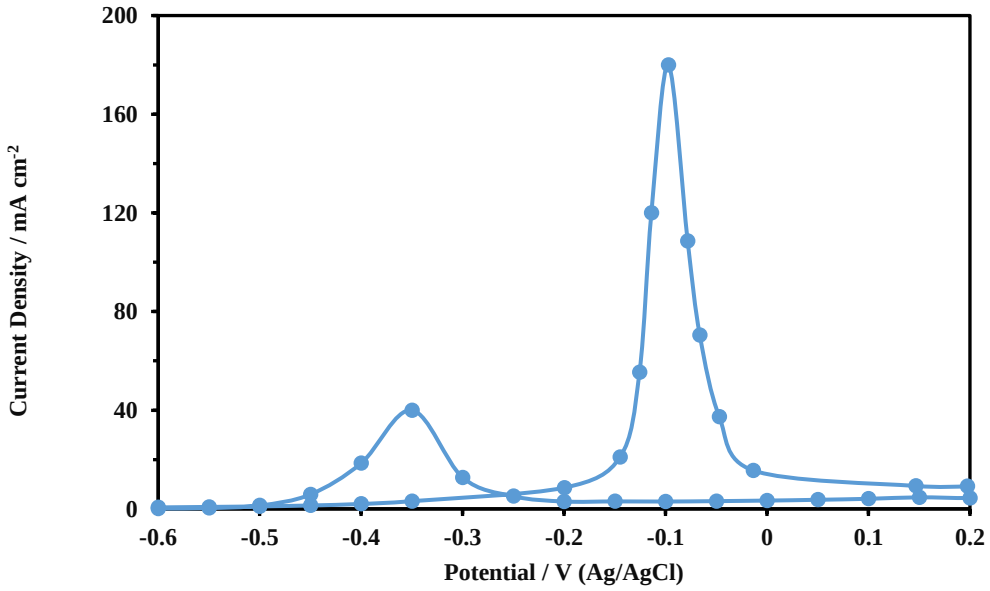

Fig. 6. Cyclic voltammogram of Pd-Co/rGO electrocatalyst in the solution containing 1M KOH and 1M EG at room temperature with the scan rate of 50 mV s^{-1}.

Results demonstrate that Pd-Co/rGO electrocatalyst has higher and lower performance compared to alloyed-based Pd and Pt electrocatalysts, respectively. High activity of Pd-Co/rGO toward EG oxidation reaction results from the strategic co-operation of Pd and Co by alloying. Pd is predicted to migrate from the core of the particle to the surface layer on Co. In other words, Pd and Co were found to occupy shell and core positions in a Pd-Co nano-alloy catalyst, respectively. The reason of this fact can be generally described by two independent factors: i) cohesive energy and ii) atomic size (quantified by Wigner-Seitz radius). A positive cohesive energy value ($\Delta E_{Pd(Co)}$ = 0.75 eV) means that the core-shell structure prefers Co in the core and Pd in the shell [36]. On the other hand, an element with a small atomic radius (1.39 Å of Co vs. 1.52 Å of Pd) tend to occupy the core to relieve the compressive strain [37].

The ratio of the forward peak current density (j_f) to the reverse peak current density (j_r), j_f/j_r, is employed to determine the tolerance of Pd-Co/rGO against poisoning intermediate carbonaceous species accumulated on the electrode surface. A higher ratio than one is related to the efficient oxidation of alcohol during the forward scan and less accumulation of carbonaceous residues on the electrode surface [31]. According to Fig. 6, j_f/j_r of EG oxidation is 4.5, indicating that the tolerance of Pd-Co/rGO toward poisoning is high in the EG oxidation reaction.

Table 1, Comparative electro-catalytic properties of the Pd-based and Pt-based nano-catalysts toward EG oxidation reaction in the alkaline medium

Catalyst	Catalyst loading (mg_{Pd} cm^{-2})	KOH (M)	EG (M)	E_s (V)	E_P (V)	j_P (mA cm^{-2})	Sa_p (mA mg^{-1}_{Pd})	Ref.
Pd-Sn/MWCNT	0.21	0.5	0.5	-0.44	0.23	51.9	247	[14]
Pd-Ni/MWCNT	0.21	0.5	0.5	-0.39	0.25	35.3	168	[14]
Pd-NiO/C	0.3	1	1	-0.48		104	347	[20]
Pd-Co_3O_4/C	0.3	1	1	-0.55		98	327	[20]
Pd/C	0.25	0.1	0.5	-0.45	0.08	88	352	[20]
Pd-CeO_2/C	0.3	1	1	-0.46		68	227	[20]
Pd-Mn_3O_4/C	0.3	1	1	-0.5		72	240	[20]
Pt-Pd/rGO	0.085	1	0.5	-0.46	-0.16	134.5	1582	[12]
Pt-Pd/C	0.085	1	0.5	-0.56	-0.11	59.8	703	[12]
Pt/C	0.085	1	0.5	-0.54	-0.01	60.3	709	[12]
Pt/rGO	0.085	1	0.5	-0.48	-0.16	53.2	623	[12]
Pd/rGO	0.085	1	0.5	-0.3	-0.16	10.7	125	[12]
Pd-Co/rGO	0.4	1	1	-0.3	-0.1	180	450	Current

Fig. 7 shows products obtained for electro-oxidation of EG in the alkaline medium [38, 39]. Results indicate that the oxidation of EG is mechanistically complicated and most EG oxidation intermediates can be produced and accumulated on the electrocatalyst surface, resulting in blocking the active sites and reducing the electrocatalyst stability.

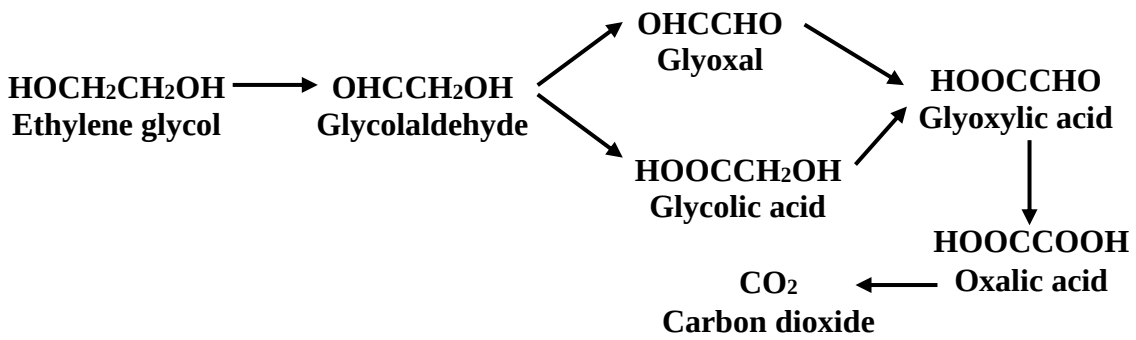

Fig. 7. Products obtained by electro-oxidation of EG [38, 39].

The stability of current density and electro-catalytic activity of the Pd-Co/rGO electrocatalyst was also investigated by CV experiment during 150 CV cycles. Fig. 8 shows consecutive CV patterns for EG electro-oxidation on the Pd-Co/rGO.

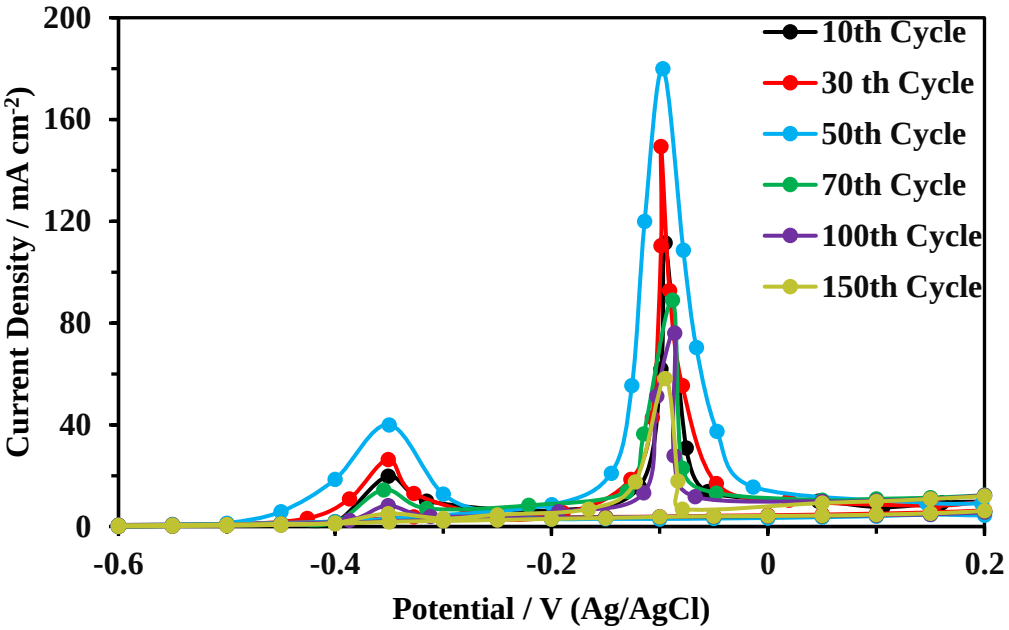

Fig. 8. Consecutive CVs of Pd-Co/rGO electrocatalyst in the solution containing 1M KOH and 1M EG at room temperature with the scan rate of 50 mV s^{-1}.

It can be seen in Fig. 8 that j_P value was increased during the time up to 50th CV cycle, exhibiting the Pd-Co/rGO activation period. After 50th CV cycle, as shown in Fig. 8, j_p value was decreased with increasing of the CV cycle number because EG was consumed and the electrocatalyst surface was poisoned by the produced intermediates. The j_p value of EG oxidation on the Pd-Co/rGO declined 68% under 150 CV cycle. However, Pd-Co/rGO catalyst still exhibits well-defined peaks for the EG oxidation reaction after 150 CV cycle. This result demonstrates that Pd-Co/rGO electrocatalyst is still active in EG oxidation reaction even after 150 CV cycles. It can be concluded that the poisoning toleration and stability of Pd-Co/rGO electrocatalyst is high in the EG oxidation reaction.

The long-term electro-catalytic activity of Pd-Co/rGO in the EG oxidation reaction has also been investigated by CA experiment in the solution containing 1M KOH and 1M EG, with an applied potential of -0.1V. The time period of CA testing was set 1000 s. Fig. 9 shows the chronoamperogram of Pd-Co/rGO in the EG oxidation reaction. CA curve displays the decay of current during the time, which would be related to the remaining of the adsorbed intermediate products of EG oxidation on the surface of the electrocatalyst.

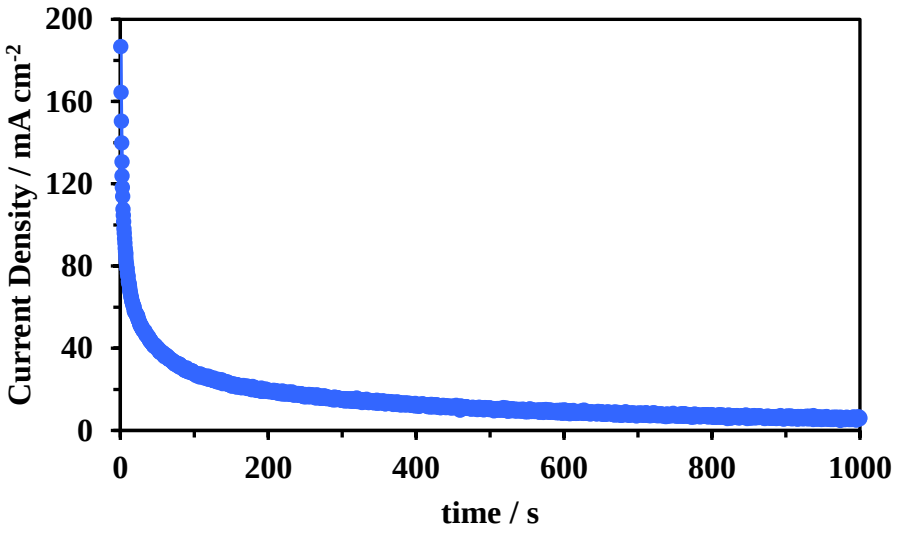

Fig. 9. Chronoamperometric curve for Pd-Co/rGO electrocatalyst in the solution containing 1 M KOH and 1M of EG with an applied potential of -0.1V.

4. Conclusions

In this work, Pd-Co/rGO nano-particles were synthesized with the simple one-step method. During the catalyst synthesis process, GO was reduced to rGO. Pd-Co/rGO electrocatalyst were characterized by XRD, EDX and FE-SEM and Raman spectra techniques. The electrochemical performance of the Pd-Co/rGO was investigated by CV technique. Pd-Co/rGO exhibited high j_p (180 mA cm^{-2}) and low E_s (-0.3V) in EG oxidation reaction. Results showed an excellent catalytic activity of Pd-Co/rGO in terms of Sa_p compared to the reported results in the literature for EG electro-oxidation in alkaline media. The j_p value of EG oxidation on the Pd-Co/rGO declined 68% under 150 CV cycle, suggesting that synthesized Pd-Co/rGO nanoparticles were durable for EG electro-oxidation.

Conflicts of interest

The authors declare that they have no known competing financial interests or personal relationships that could have appeared to influence the work reported in this paper. Also, there are not any conflicts of interest.

Acknowledgment

The support of the *Najafabad Branch, Islamic Azad University* is acknowledged. The authors would also like to special thanks to Dr. Saeedeh Kamali Ph.D of chemistry department of Isfahan University of Technology for her corporation.

References:

[1] K. Tran, T. Q. Nguyen, A. M. Bartrom, A. Sadiki, J. L. Haan, "A Fuel-Flexible Alkaline Direct Liquid Fuel Cell", Fuel Cells, Vol. 14, 2014, pp. 834-841.

[2] Z. Y. Li, Y. J. Liang, S. P. Jiang, X. D. Shan, M. L. Lin, C. W. Xu, "Electrooxidation of Methanol and Ethylene Glycol Mixture on Platinum and Palladium in Alkaline Medium", Fuel Cells, Vol. 12, 2012, pp. 677-682.

[3] M. Zhiani, S. Majidi, H. Rostami, M.M.Taghiabadi, "Comparative study of aliphatic alcohols electrooxidation on zero-valent palladium complex for direct alcohol fuel cells", Int. J. Hydrogen Energy, Vol. 40, 2015, pp. 568-576.

[4] T. Asset, A. Serov, M. Padilla, A.J. Roy, I. Matanovic, M. Chatenet, et al., "Design of Pd-Pb catalysts for glycerol and ethylene glycol electrooxidation in alkaline medium", Electrocatalysis, Vol. 9, 2018, pp. 480-485.

[5] F. Gomes, V.L. Oliveira, P.M.P. Pratta, G.T. Filho, "Reactivity of alcohols with three-carbon atom chain on Pt in acidic medium", Electrocatalysis, Vol. 6, 2015, pp.7-19.

[6] G. Cui, P.K. Shen, H. Meng, J. Zhao, G. Wu, "Tungsten carbide as supports for Pt electrocatalysts with improved CO tolerance in methanol oxidation", J. Power Sources, Vol. 196, 2011, pp. 6125-6130.

[7] Y. Xia, X. Yang, "Toward cost-effective and sustainable use of precious metals in heterogeneous catalysts", Acc. Chem. Res., Vol. 50, 2017, pp. 450-454.

[8] Y. Kim, H. Kim, W.B. Kim, "PtAg nanotubes for electrooxidation of ethylene glycol and glycerol in alkaline media", Electrochem. Commun. Vol. 46, 2014, pp. 36-39.

[9] C. Xu, P.K. Shen, "Novel Pt/CeO2/C catalysts for electrooxidation of alcohols in alkaline media", Chem. Commun., Vol. 19, 2004, pp. 2238-2239.

[10] C. Xu, R. Zeng, P.K. Shen, Z. Wei, "Synergistic effect of CeO2 modified Pt/C catalysts on the alcohols oxidation", Electrochim. Acta, Vol. 51, 2005, pp. 1031-1035.

[11] R. Baronia, J. Goel, V. Kataria, S. Basu, S.K. Singhal, "Electro-oxidation of ethylene glycol on Pt-Co metal synergy for direct ethylene glycol fuel cells: Reduced graphene oxide imparting a notable surface of action", Int. J. Hydrogen Energy, Vol. 44, 2019, pp. 10023-10032.

[12] K.J. Ju, L. Liu, J.J. Feng, Q.L. Zhang, J. Wei, A.J. Wang, "Bio-directed one-pot synthesis of Pt-Pd alloyed nanoflowers supported on reduced graphene oxide with enhanced catalytic activity for ethylene glycol oxidation", Electrochim. Acta, Vol. 188, 2016, pp. 696-703.

[13] N. Cai, J. Wu, R. Dong, C. Jin, "High performance of AuPt deposited on Ni nanoparticles in ethylene glycol oxidation", J. Power Sources, Vol. 412, 2019, pp. 37-43.

[14] T. Ramulifho, K.I. Ozoemena, R.M. Modibedi, C.J. Jafta, M.K. Mathe, "Electrocatalytic oxidation of ethylene glycol at palladium-bimetallic nanocatalysts (PdSn and PdNi) supported on sulfonate-functionalised multi-walled carbon nanotubes", J Electroanal. Chem., Vol. 692, 2013, pp. 26-30.

[15] A. Serov, U. Martinez, P. Atanassov, "Novel Pd–In catalysts for alcohols

electrooxidation in alkaline media", Electrochem. Commun., Vol. 34, 2013, pp. 185-188.
[16] R. Kannan, K. Karunakaran, S. Vasanthkumar, "PdNi-decorated manganite nanocatalyst for electrooxidation of ethylene glycol in alkaline media", Ionics, Vol. 18, 2012, pp. 803-809.
[17] V. Bambagioni, M. Bevilacqua, C. Bianchini, J. Filippi, A. Marchionni, F. Vizza, et al., "Ethylene glycol electrooxidation on smooth and nanostructured Pd electrodes in alkaline media", Fuel Cells, Vol. 10, 2010, pp. 582-590.
[18] O.O. Fashedemi, K.I. Ozoemena, "Comparative electrocatalytic oxidation of ethanol, ethylene glycol and glycerol in alkaline medium at Pd-decorated FeCo@ Fe/C core-shell nanocatalysts", Electrochim. Acta, Vol. 128, 2014, pp. 279-286.
[19] P.K. Shen, C. Xu, "Alcohol oxidation on nanocrystalline oxide Pd/C promoted electrocatalysts", Electrochem. Commun., Vol. 8, 2006, pp. 184-188.
[20] C. Xu, Z. Tian, P. Shen, S.P. Jiang, "Oxide (CeO2, NiO, Co3O4 and Mn3O4)-promoted Pd/C electrocatalysts for alcohol electrooxidation in alkaline media", Electrochim. Acta, Vol. 53, 2008, pp. 2610-2618.
[21] S. Yongprapat, A. Therdthianwong, S. Therdthianwong, "Au/C catalysts promoted with metal oxides for ethylene glycol electro-oxidation in alkaline solution", J Electroanal. Chem., Vol. 697, 2013, pp. 46-52.
[22] C. Jin, Y. Song, Z.Chen, "A comparative study of the electrocatalytic oxidation of ethylene glycol on PtAu nanocomposite catalysts in alkaline, neutral and acidic media", Electrochim. Acta, Vol. 54, 2009, pp. 4136-4140.
[23] M. Brandalise, M.M. Tusi, R.M. Piasentin, M. Santos, E.V. Spinace, A.O. Neto, "Synthesis of PdAu/C and PdAuBi/C electrocatalysts by borohydride reduction method for ethylene glycol electro-oxidation in alkaline medium", Int. J. Electrochem. Sci., Vol. 7, 2012, pp. 9609-9621.
[24] K.I. Ozoemena, "Nanostructured platinum-free electrocatalysts in alkaline direct alcohol fuel cells: catalyst design, principles and applications", RSC Adv., Vol. 6, 2016, pp. 89523-89550.
[25] R. Ferrando, J. Jellinek, R.L. Johnston, "Nanoalloys: from theory to applications of alloy clusters and nanoparticles", Chem. Rev., Vol. 108, 2008, pp. 845-910.
[26] A. Ambrosi, C.K. Chua, N.M. Latiff, A.H. Loo, C.H.A. Wong, A.Y.S. Eng, et al., "Graphene and its electrochemistry–an update", Chem. Soc. Rev., Vol. 45, 2016, pp. 2458-2493.
[27] A.A. Elzatahry, A.M. Abdullah, T.A.S. El-Din, A.M. Al-Enizi, A.A. Maarouf, A. Galal, et al., "Nanocomposite graphene-based material for fuel cell applications", Int. J. Electrochem. Soc., Vol. 7, 2012, pp. 3115-3126.
[28] H. Rostami, A.A. Rostami, A. Omrani, "Investigation on ethanol electrooxidation via electrodeposited Pd–Co nanostructures supported on graphene oxide", Int. J. Hydrogen Energy, Vol. 40, 2015, pp. 10596-10604.
[29] A.S. Douk, H. Saravani, M. Noroozifar, "A fast method to prepare Pd-Co nanostructures decorated on graphene as excellent electrocatalyst toward formic acid oxidation", J. Alloys Compd, Vol. 739, 2018, pp. 882-891.
[30] D. Wang, H.L. Xin, H. Wang, Y. Yu, E. Rus, D.A. Muller, et al., "Facile synthesis of carbon-supported Pd–Co core–shell nanoparticles as oxygen reduction electrocatalysts and their enhanced activity and stability with monolayer Pt decoration", Chem. Mate., Vol. 24, 2012, pp. 2274-2281.
[31] Y. Wang, Y. Zhao, J. Yin, M. Liu, Q. Dong, Y. Su, "Synthesis and electrocatalytic alcohol oxidation performance of Pd–Co bimetallic nanoparticles supported on graphene", Int. J. Hydrogen Energy, Vol. 39, 2014, pp. 1325-1335.
[32] S.N. Alam, N. Sharma, L. Kumar, "Synthesis of graphene oxide (GO) by modified hummers method and its thermal reduction to obtain reduced graphene oxide (rGO)", Graphene, Vol. 6, 2017, pp. 1-18.
[33] F.T. Johra, J.W. Lee, W.G. Jung. "Facile and safe graphene preparation on solution based platform", J. Ind. Eng. Chem., Vol. 20, 2014, pp. 2883-2887.
[34] A.C. Ferrari, J. Robertson, "Interpretation of Raman spectra of disordered and amorphous carbon", Phys. Rev., Vol. 61, 2000, pp.14095-14107.
[35] R. Krishna, D.M. Fernandes, J. Ventura, C. Freire, E. Titus, "Facile synthesis of reduced graphene oxide supported Pd@NixB/RGO nanocomposite: novel electrocatalyst for ethanol

oxidation in alkaline media", Int. J. Hydrogen Energy, Vol. 41, 2016, pp.11811-11822.
[36] L.L. Wang, D.D. Johnson, "Predicted trends of core− shell preferences for 132 late transition-metal binary-alloy nanoparticles", J. Ame. Chem. Soc., Vol. 131, 2009, pp. 14023-14029.
[37] H. Yamauchi, "Surface segregation in jellium binary solid solutions", Phys. Rev. *B*, Vol. 31, 1985, pp.7688-7694.
[38] M. Zhiani, A. Abedini. S. Majidi, "Comparison of electro-catalytic activity of Fe-Ni-Co/C and Pd/C nanoparticles for glucose electro-oxidation in alkaline half-cell and direct glucose fuel cell", Electrocatalysis, Vol. 9, 2019, pp.735-743.
[39] B. Wieland, J.P. Lancaster, C.S. Hoaglund, P. Holota, W.J. Tornquist, "Electrochemical and infrared spectroscopic quantitative determination of the platinum-catalyzed ethylene glycol oxidation mechanism at CO adsorption potentials", Langmuir, Vol. 12, 1996, pp.2594-2601.

JMATPRO	Journal of Advanced Materials and Processing 9 (3): 47-53, Summer 2021 http://jmatpro.iaun.ac.ir 20.1001.1.2322388.2021.9.3.4.4

Research Paper

Modelling Dependency of the Steady-State Grain Size on the Stacking Fault Energy in Severely Plastic Deformed Materials

Maryam Bahmanpour[1*], Majid Abdellahi[2]
1. Mathematics Departments, Isfahan Branch, Islamic Azad University, Isfahan, Iran
2. Advanced Materials Research Center, Faculty of Materials Engineering, Najafabad Branch, Islamic Azad University, Najafabad, Iran

ARTICLE INFO

Article history:

Received 24 April 2021
Accepted 28 July 2021
Available online 1 August 2021

Keywords:
GEP-Modelling
severe plastic deormation (SPD)
stacking fault energy (SFE)
Steady-state grain size

ABSTRACT

In the present work, a computer-based method is proposed to investigate the relationship between the steady-state grain size (ds) and stacking fault energy (SFE) in severely plastic deformed (SPDed) materials. The stacking fault energy, γ, plays an important role in determining the mechanical properties of face-centered cubic (fcc) metals. A number of models have been proposed to show this role. These models have several shortcomings, including complex computational variables, data constraints and small computational range constraints. The present model compatible with experimental results does not employ hard calculable variables. Besides, it is applicable not only for pure metals but also for alloys. The squared regression (R^2) and error sum of squares (SSE) for the training and testing data of the presented model are 0.93, 0.0006 and 0.98, 0.00018, respectively, which indicates the high accuracy of the proposed model. The slope of the $\log\frac{\gamma}{Gb}$ versus $\log\frac{d_s}{b}$ is about 0.6453 which is comparable to all the models offered in this field.

Citation: Bahmanpour, M., Abdellahi, M., (2021), Modelling Dependency of the Steady-State Grain Size on the Stacking Fault Energy in Severely Plastic Deformed Materials, 9 (3), 47-53. Dor: 20.1001.1.2322388.2021.9.3.4.4

[*] **Corresponding Author**
E-mail address: mbahmanpour@khuisf.ac.ir

1. Introduction

Severe plastic deformation (SPD) is a method to produce ultrafine bulk materials for industrial applications. In various systems such as Cu-Al, Cu-Zn, and Pd-Ag, it has been demonstrated that *d*s or dmin (minimum grain size) is dependent on stacking fault energy (SFE) [1]. Many models have been proposed to confirm this dependence [2-9].This dependence is represented by a parameter called *q* (the average parameter *q* is approximately 0.65.), which is essentially the slope of the $\log\frac{\gamma}{Gb}$ versus $\log\frac{d_s}{b}$, where *b* is the Burgers vector and *G* is the shear modulus. The proposed models are based on limited data and do not have a high computational theory. On the other hand, they cannot be used in alloys and are used only for pure metals, which confirms the lack of high potential in these models. In the present work, Gene Expression Programming (GEP) as one of the most important branches of artificial intelligence (AI) has been used for simulating the SPD process and providing a relation between the γ and d_s. According to the obtained results, the presented model overcomes the mentioned shortcomings (in other models) and then assesses its reliability and accuracy by experimental results.

2. The model

The exact functionality of this model has been explained in our previous work [10]. It is worth mentioning that prior to introducing the data to the model, they are divided into two groups, namely the training and the testing datasets. Testing data are randomly selected from all data and entered into the model to test the training data (see Table 1 and Table 2). This guarantees that the model output for the training data will not be false. Genetic programming (GP), one of the newest paradigms of evolutionary computations, can automatically learn the introduced problem by mimicking the Darwinian evolution process [10]. Gene expression programming (GEP) as an extension of GP, is used in this paper to develop the model. GEP method includes individuals referred to linear strings with fixed-size called genome or non-linear entities containing various sizes and shapes called expression trees (ETs). Generally, any individual contains one chromosome having one or more genes, divided into head and tail parts [10]. Moreover, there are two languages in GEP: the language of the genes and the language of ETs. A simple chromosome as a linear string with two genes is encoded, as shown in Fig. 1 as an example for ET language. Its ET and the corresponding mathematical formula are also shown in the same figure**.**

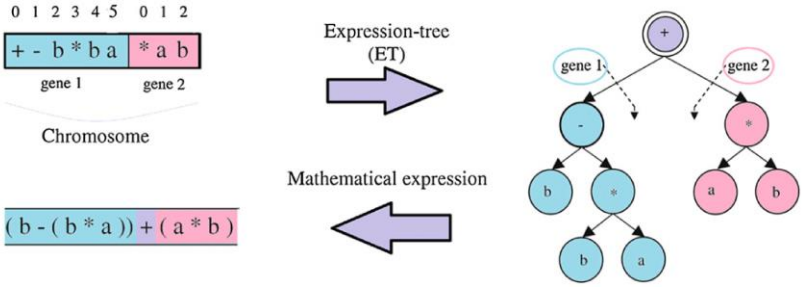

Fig. 1. A simple chromosome as a linear string with two genes

3. Results and discussion

Seven input parameters comprised of *b*, *D*, *G*, *H*, γ, *Q* and *T* were inserted to the GEP model as input layers, while the output layer was set on d_s. Fig. 2 shows an expression tree for the steady-state grain size values (d_s or d_{min}) of the SPDed materials as output layer in this research. It should be noted that the variables of d0, d1, d2, d3, d4, d5 and d6 are the values for the abovementioned input layers, which are b, *D*, *G*, *H*,γ, *Q* and *T*, respectively.

Table 1. Modeling database for various metals and alloys in training mode [6]

Materials used in SPD process	***T* (K)**	***G* (GPa)**	***b* (nm)**	**D (m^2s^{-1})**	***Q* (kJ/mol)**	**γ (mJm^{-2})**	***H*(GPa)**	**d_s(nm)**
Mg	922	17	0.3197	1.75	138	125	0.34	1000
Fe	1809	82	0.2482	1.9	240	180	3.02	200
Co	1768	82	0.2497	0.55	298	31	3.28	100
Ni	1728	75	0.2492	1.77	285	125	3.02	170
Pd	1825	46	0.2751	20.5	266	180	2.13	240
Ag	1234	27	0.2889	27.8	182	16	0.94	220
Al-Mg	906	26	0.2881	4.4	140	27	1.98	190
Al-Ag	928	26	0.2864	0.33	125	175	0.59	500
Al-Ag	920	26	0.2864	1.5	136	190	0.74	500
Al-Cu	923	26	0.2858	0.18	126	166	2.01	207
Cu-Al	1350	47	0.2565	0.287	188	37	2.1	65
Cu-Al	1335	46	0.2578	1.293	191	8	2.51	118
Cu-Zn	1283	41	0.2593	0.36	170	18	2.4	108
Cu-Zn	1223	37	0.261	1.7	172	14	2.49	74
Pd-Ag	1733	42	0.2779	17.6	126	125	2.92	150
Ni-Fe	1713	78	0.2537	41.5	316	79	3.92	120
Ni-Co	1733	76	0.2493	0.725	273	120	3.58	197
Ni-Co	1738	78	0.2497	0.166	258	90	4.06	115

Table 2. Modeling database for various metals and alloys in testing mode [6]

Materials used in SPD process	***T* (K)**	***G* (GPa)**	***b* (nm)**	**D (m^2s^{-1})**	***Q* (kJ/mol)**	**γ (mJm^{-2})**	***H*(GPa)**	**d_s(nm)**
Al	933	26	0.2864	17.6	126	166	0.31	1500
Cu	1357	48	0.2556	35	204	45	1.3	400
Al-Mg	930	26	0.2867	0.49	124	87	1.25	330
Al-Mg	916	26	0.2874	0.32	122	54	1.8	230
Al-Ag	906	26	0.2864	11	155	210	1.11	500
Cu-Zn	1330	45	0.2575	0.13	170	35	2.23	110
Pd-Ag	1774	44	0.2758	1.75	138	165	2.61	206
Pd-Ag	1648	38	0.28	1.9	240	119	3	144

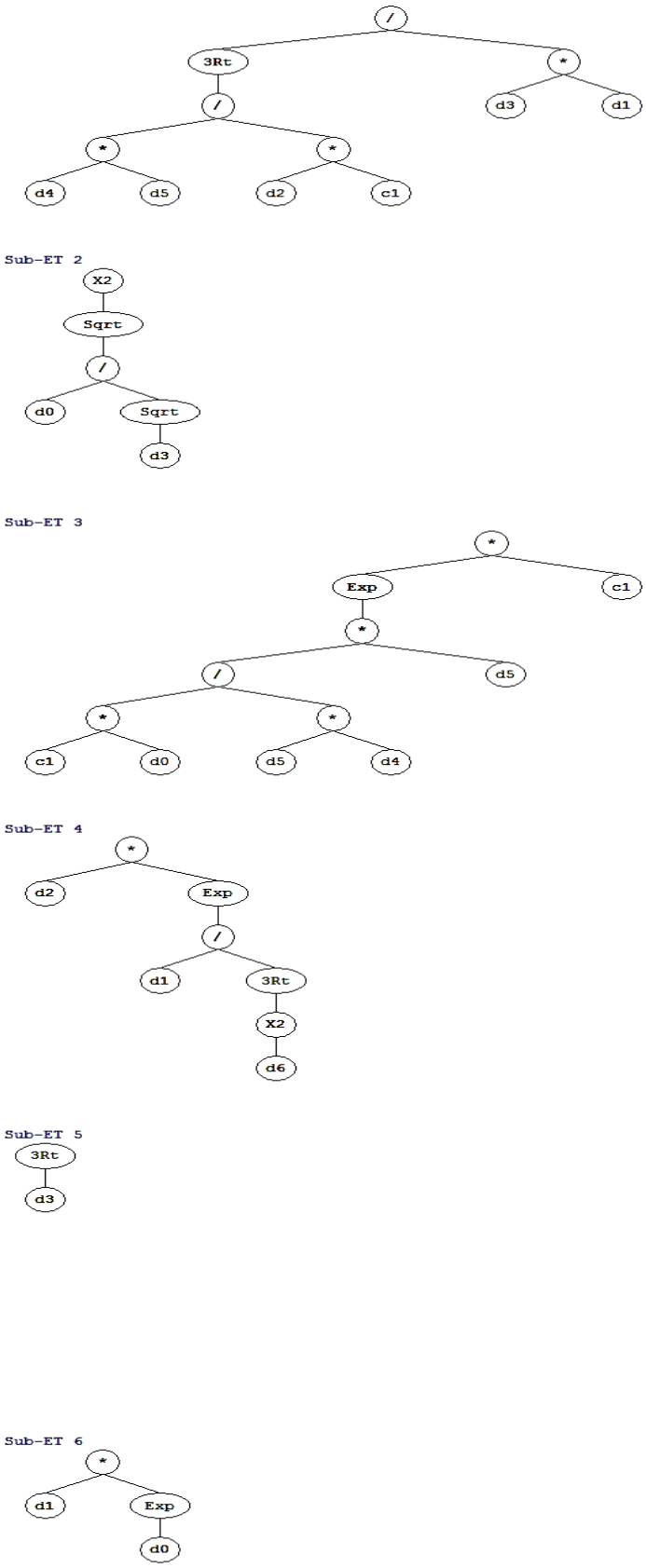

Fig. 2. The expression tree with 6 genes for predicting d_s

Table 1 and Table 2 show the experimental sets collected from the literature for the modelling process [5]. There are two sets of data in any simulating/modelling process, including training and testing which used for learning and generalizing model, upheaval buckling predictive models (for additional details, please refer to our previous work [10]). In this research 18 data were randomly chosen as the training and remained 8 data were used as testing. The model containing the best-predicted values of d_s in both of the training and testing data sets is adopted as the best model for simulating SPD process. The formula derived from the ETs presented in Fig. 2, with the procedure shown in Fig. 1, is in accordance with the following equation:

$$d_s = \left(\left(\frac{\gamma Q}{8.7\mathrm{G}}\right)^{1/3} / HD\right)\left(\frac{b}{H^{1/2}}\right)\left(7.3\exp\left(\frac{7.3b}{\gamma}\right)\right)\left(\mathrm{G}\exp\left(\frac{D}{T_m^{2/3}}\right)\right)(H)^{1/3}\left(D\exp(b)\right) \quad (1)$$

Or

$$\frac{d_s}{b} = 3.5\left(\frac{\gamma}{Gb}\right)^{1/3}\left(\frac{G\left(HbQ\right)^{1/3}}{H^{3/2}}\right)\exp\left(\frac{7.3b}{\gamma} + \frac{D}{T_m^{2/3}} + b\right) \quad (2)$$

Two points are extracted from Eq.2:

1- The Burgers vector, the frequency factor for pipe diffusion and the melting temperature play an exponential role, indicating they have a more important effect than the other mentioned parameters.

2- There is a linear relationship between $\frac{\gamma}{Gb}$ and $\frac{d_s}{b}$ or between $\log\frac{\gamma}{Gb}$ and $\log\frac{d_s}{b}$.

The latter has been also reported in previous works. To illustrate, Qu et al. [1] analyzed the dependency of the normalized steady-state grain size on the normalized SFE for SPDed materials. They reported a simple linear relationship between $\frac{\gamma}{Gb}$ and $\frac{d_s}{b}$.

Moreover, Mohamed et al. [2] presented a model in which $\log\frac{\gamma}{Gb}$ and $\log\frac{d_s}{b}$ have a linear connection as follows:

$$\frac{d_s}{b} = A\exp\left(\frac{-\beta Q}{4RT}\right)\left(\frac{DGb^2}{vkT}\right)^{1/4}\left(\frac{\gamma}{Gb}\right)^{1/2}\left(\frac{G}{H}\right)^{5/4} \quad (3)$$

where, A is a constant, β= 0.04, Q is the activation energy for self-diffusion, R is the gas constant, T is the absolute temperature, D is the frequency factor for pipe diffusion, v is the initial dislocation velocity, k is Boltzmann's constant, γ is the stacking fault energy, and H is the steady-state hardness.

Another model which has been expressed by using thermodynamic relations and almost confirms the results of our model is Kazeminezhad model [3], which is expressed as follows:

$$\frac{d_s}{b} = A\exp\left(\frac{-\alpha Q}{3RT}\right)\left(\frac{DGb^2}{vkT}\right)^{1/3}\left(\frac{\gamma}{Gb}\right)^{2/3} \quad (4)$$

where $\alpha = 0.037$.

In addition, there are many experimental works reporting a power-law relationship for the dependency of ds to SFE [2-9]. These models have great potential for simulating SFE. However, several major flaws are common to all of them:

a) The initial speed of dislocation to which these relations have referred is almost hardly calculable and, as a consequence, it reduces the precision of the models.

b) The amounts of α and β can only be measured by experimental data and no mathematical theory supports them. This also results in obscurity and the reduction of the precision of the models.

c) The number of experimental data for making a linear relationship is too small.

d) They are applicable only for pure metals but not for alloys

Our presented model (Eq.1) covers all the above flaws. Firstly, it does not need to calculate ambiguous variables (such as α or β); secondly, it covers a wide range of alloys and pure metals, and thirdly, it is very accurate.

In order to assess the precision of the presented model, we have to compare the slope of the straight line in Fig. 3a (which the slope of the $\log\frac{\gamma}{Gb}$ versus $\log\frac{d_s}{b}$) with that of the diagram obtained from the presented model (Fig. 3b). If we consider Fig.4a which has been drawn on the basis of experimental data [11-17], it can be observed that the slope of the straight line (q) is 0.63 (plotting the logarithm of the normalized steady-state grain size against the normalized stacking fault energy, gives a straight line), which is in agreement with the results obtained by previous studies [2-9]. In the latter diagram, which has been drawn based on the predicted d_s, it can be seen that the slope is q=0.6453. Mohammed et al. [2], and Kazeminejard et al. [3] reported a value of 0.65 and 0.66 for q, respectively. Other studies in this field have reported almost the same results for the value of q as 0.65 [7], 0.69 [8], 0.63 [9], 0.64 [19].

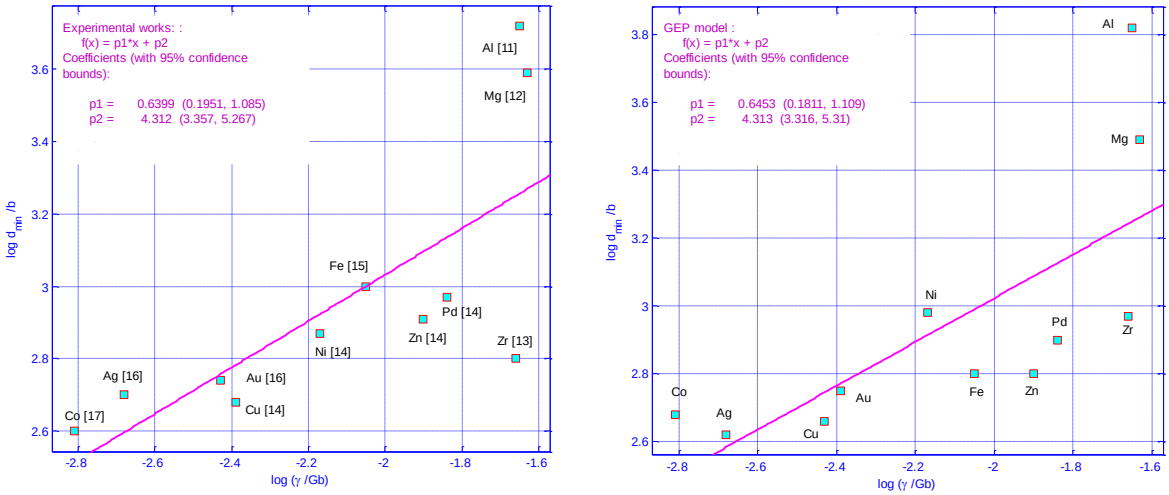

(a) (b)

Fig. 3. Normalized steady-state grain size (d_s / b) vs. the normalized stacking fault energy (γ/Gb) for a: experimental and b) modelling results

One of the significant advantages of this model over the other mentioned models is its rich database (Table 1 and Table 2). As can be seen in these Tables, the materials selected for modelling process are not only pure metals but also a variety of different alloys. This makes the model applicable for both pure metals and alloys.

To assess the ability of the GEP-based formulation (Eq. 1), the developed regression-based formulation R-square (R^2) was used as the measurements index between the experimental and predicted d_s values according to the following equation [18]:

$$R^2 = \frac{\left(n\sum t_i o_i - \sum t_i \sum o_i\right)^2}{\left(n\sum t_i^2 - \left(\sum t_i\right)^2\right)\left(\left(n\sum o_i^2 - \left(\sum o_i\right)^2\right)\right)} \quad (5)$$

where ‘‘t’’ is the experimental value, ‘‘o’’ is the predicted value, and ‘‘n’’ is total number of data.

Figure 4 shows the comparison between the experimental values of *d*s and the predicted ones obtained from the training and testing results of the GEP model. As can be seen, the R^2 and error sum of squares (SSE) values are shown in this figure for the training (Fig. 4a) and testing (Fig. 4b) datasets. There is no need to explain that the high amount of R^2 ensures that the values obtained for the training and testing datasets in the GEP model are very close to the experimental results. The R^2 values in the training and testing sets show that the proposed GEP is suitable and can predict *d*s very close to the experimental values.

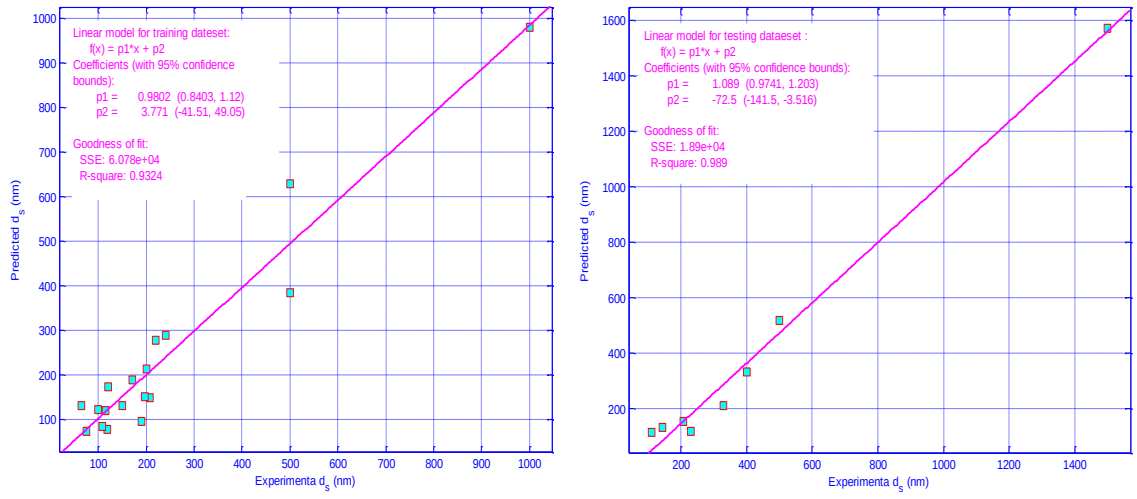

(a) (b)

Fig. 4. The correlation of the measured and predicted d_s in (a) the training and (b) the testing phase

4. Conclusion

In this study, a computer-based model was introduced for dependent of the steady-state grain size to stacking fault energy. The evaluation of model using experimental data showed that there is a perfect match between the current and previous models. However, there are several advantages to this model. First, it is applicable not only for pure metals but also for alloys, second, it does not employ hardly calculable variables and third, it is more accurate and more diverse. The slope of the $\log\frac{\gamma}{Gb}$ versus $\log\frac{d_s}{b}$ is about 0.6453 which is comparable to all the models offered in this field. In this research, 18 sets were randomly chosen as the training and remained 8 sets were used as testing. R^2 values for training and testing datasets of the proposed model are 0.93 and 0.98, respectively, which confirms the high accuracy of the model.

References

[1] S. Qu, X.H. An, H.J. Yang, C.X. Huang, G. Yang, Q.S. Zang, et al., Microstructural evolution and mechanical properties of Cu–Al alloys subjected to equalchannel angular pressing, Acta Mater. 57 (2009) 1586–1601.

[2] Mohamed FA. A dislocation model for the minimum grain size obtainable by milling. Acta Mater 2003;51:4107–19.

[3] Parvin H, Kazeminezhad M, Dependency Modeling of steady state grain size on the stacking fault energy through severe plastic deformation. Mater Let, http://dx.doi.org/10.1016/j.matlet.2015.07.041

[4] Mohamed FA. Correlation between the behavior of nanocrystalline HCP metals and the dislocation model for the minimum grain size obtainable by milling. Mater Sci Eng A 2010;527(9):2157-62.

[5] Edalati K, Akama D, Nishio A, Lee S, Yonenaga Y, Sesin JMC, Horita Z, Influence of dislocation–solute atom interactions and stacking fault energy on grain size of single-phase alloys after severe plastic deformation using high-pressure torsion. Acta Mater 2014;69:68-77.

[6] Lu S, Hu QM, Delczeg-Czirjak EK, Johansson B, Vitos L, Determining the minimum grain size in severe plastic deformation process via first-principles calculations. Acta Mater 2012;60:4506-13.

[7] Huang M, Rivera-Díaz-del-Castillo PEJ, Bouaziz O, Van Der Zwaag S. Irreversible thermodynamics modelling of plastic deformation of metals. Mater Sci Technol 2008;24:495-500.

[8] Cai B, Tao J, Wang W, Yang X, Gong Y, Cheng L, et al. The effect of stacking fault energy on equilibrium grain size and tensile properties of ultrafine-grained Cu-Al-Zn alloys processed by rolling. J Alloy Compd 2014;6:115-9.

[9] Zhao YH, Zhu YT, Liao XZ, Horita Z, Langdon TG. Influence of stacking fault energy on the minimum grain size achieved in severe plastic deformation. Mater Sci Eng A 2007;463(1):22-6

[10] Abdellahi M, A new predictive model for calculating the hardness of metal matrix nanocomposites produced by mechanical alloying. J Mater Res 2013;28:3270–78.

[11] Edalati K, Ito Y, Suehiro K, Horita Z. Softening of high purity aluminum and copper processed by high pressure torsion. Int J Mater Res 2009;100:1668-73.

[12] Edalati K, Yamamoto A, Horita Z, Ishihara T. High pressure torsion of pure magnesium. Scripta Mater 2011;64:880-3

[13] Edalati K, Horita Z, Yagi S, Matsubara E. Allotropic phase transformation of pure zirconium by high-pressure torsion. Mater Sci Eng A 2009;523:277.

[14] Edalati K, Horita Z. Significance of homologous temperature in softening behavior. Mater Sci Eng A 2011;528:7514-23.

[15] Edalati K, Fujioka T, Horita Z. Mater Trans. Evolution of Mechanical Properties and Microstructures with Equivalent Strain in Pure Fe Processed by High Pressure Torsion. 2009;50:44-50.

[16] Matsunaga H, Horita Z. Mater Trans. Softening and Microstructural Coarsening without Twin Formation in FCC Metals with Low Stacking Fault Energy after Processing by High-Pressure Torsion. 2009;50:1633-37.

[17] Edalati K, Toh S, Arita M, Watanabe M, Horita Z. Appl Phys Lett. High-pressure torsion of pure cobalt: hcp-fcc phase transformations and twinning during severe plastic deformation.2013;102:181902.

[18] Ferreira C, Gene expression programming: a new adaptive algorithm for solving problems, Complex Syst. 2001;13:87–129

JMATPRO	Journal of Advanced Materials and Processing 9 (3): 55-66, Summer 2021 http://jmatpro.iaun.ac.ir 20.1001.1.2322388.2021.9.3.5.5

Research Paper

Fabrication of Al7075-MWCNT Composite Powder by Recycling Aluminum Alloy Chips Via High Energy Milling and Alloying

Parisa Fekri Dolatabad[1], Vahid Pouyafar[2*], Ramin Meshkabadi[3]

1. Msc Student, Manufacturing Engineering Department, University of Tabriz, Tabriz, Iran

2. Assistant Professor, Manufacturing Engineering Department, University of Tabriz, Tabriz, Iran

3. Assistant Professor, Department of Engineering Sciences, Faculty of Advanced Technologies, University of Mohaghegh Ardabili, Namin, Iran

ARTICLE INFO

Article history:

Received 6 April 2021
Accepted 25 July 2021
Available online 1 August 2021

Keywords:
Metal Matrix Composite
Mechanical milling and alloying
Al7075-MWCNT composite
Particle size
Particle distribution

ABSTRACT

In this study, aluminum chips were milled in a planetary ball mill at different times and ball-to-powder weight ratios (BPRs). The resulting optimum powder was reinforced with 1 wt% and 2 wt% of multi-walled carbon nanotubes (MWCNTs). The effects of alloying time, BPR, and MWCNTs percentage on the morphology, distribution, and composition of the Al7075-MWCNT powder were investigated. The results showed that smaller particles with a limited size distribution can be obtainable by increasing BPR and decreasing mechanical milling time. A uniform dispersion of reinforcement (2 wt%) was achieved at lower alloying times (15 and 30 min) and a higher BPR (20:1). Using XRD analysis, it was revealed that the carbon peaks are more clearly in 2%-MWCNT powders than 1%-MWCNT ones. The addition of MWCNTs led to reducing the particle size; this is confirmed by the data obtained from the XRD patterns and their analysis with the Williamson-Hall model. Machining chips were converted into composite powder by cost-effective mechanical milling and alloying method with a uniform distribution of MWCNTs, which is unique.

Citation: Fekri Dolatabad, P., Pouyafar, V., Meshkabadi, R., (2021), Fabrication of Al7075-MWCNT Composite Powder by Recycling Aluminum Alloy Chips Via High Energy Milling and Alloying, 9 (3), 55-66. Dor: 20.1001.1.2322388.2021.9.3.5.5

* **Corresponding Author**
E-mail address: pouyafar@tabrizu.ac.ir

1. Introduction

Composite materials have been at the center of interest for many researchers because they are high-performance and low-cost materials. Over the last few decades, Metal Matrix Composites (MMCs) have been replaced by conventional materials in various industries [1]. The presence of several reinforcements like alumina (Al_2O_3), silicon carbide (SiC), boron carbide (B_4C), graphite (Gr), silica (SiO_2), tungsten carbide (WC), and multi wall carbon nanotubes (MWCNTs) leads to producing nanocomposites with superior mechanical properties [2-6]. Due to their unique physical, chemical, electrical and mechanical properties, MWCNTs are usually used in various scientific fields. The extraordinary strength, lightweight, and nanoscale dimensions of the MWCNTs have made them a good candidate to reinforce composites [7]. Successful preparation of ferrous [8], aluminum [9] and copper-based [10] composites with carbon-based reinforcements have been reported in recent years in terms of their preparation and application methods. However, their agglomeration and poor dispersion ability in the metal matrix make using them problematic [11]. The uniform dispersion of the MWCNTs and the MWCNT-metal interface is the most critical research topic because of dealing with the strong Van der Waals forces [12]. The production method, matrix, and type of the reinforcements determine the defectless microstructure of the MMCs and uniform distribution of particles [13]. For powder-based production methods, mechanical alloying has been widely used to decompose MWCNTs' clusters, disperse them homogeneously in the metal field, and achieve a uniform distribution [14].

The mechanical alloying properties obtained strongly depend on the mixing parameters [15]. Alloying time is one of the most influential parameters that play an essential role in the composite morphology and its mechanical properties [16]. Several studies have indicated the role of milling time to achieve a homogeneous distribution of components, which is an advantage of the mechanical milling method compared to the other conventional synthesis routes [9, 14]. In recent studies, the effect of parameters, including ball size, BPR, milling time, and speed, were studied to determine the optimal conditions of better structural, mechanical, electrical, and magnetic properties [14, 16]. Although some studies reported the improvement of mechanical properties, numerous challenges concerning the MWCNT-reinforced composites should be resolved, of which MWCNTs uniform dispersion is a significant concern. In this research, mechanical milling and alloying were used as an effective tool to disperse MWCNTs better. A high-energy planetary ball mill was employed to make Al7075-MWCNT powder. An appropriate range of the process parameters which results in a uniform dispersion should be determined. After mechanical alloying, the effect of milling time, BPR, and weight percentage of MWCNTs on the morphology of the Al7075-MWCNT powder were investigated.

2. Materials and methods

The sample in the form of machining chips with the size of 1×3 mm was utilized. The chemical composition of the chips was determined by spectrometric analysis. It includes 5.89% Zn, 2.19% Mg, 1.53% Cu, and less than a half percent of silicon, iron, manganese, titanium, chromium, and other metals. A high-energy planetary ball mill (250 rpm) was used for mechanical milling (see Figure 1). The vial and ball materials were hardened steel and chrome steel, respectively. Argon was used to prevent the chips from oxidizing during milling; in addition, 1 wt% of stearic acid was used as a process control agent (PCA) to prevent agglomeration of the particles. The chips were milled at three milling times (1, 3, and 5 h) with three different BPRs (10:1, 15:1, and 20:1).

Fig. 1. The high-energy planetary ball mill.

Mechanical alloying was utilized to better disperse the MWCNTs in the aluminum alloy. MWCNTs agglomeration changes the composite properties. Therefore, there must be an optimization process to prepare an appropriate composite powder for the alloying process. The powder chips and MWCNTs (NANOSANY CORPORATION) with an inner diameter of 5-10 nm, an outer diameter of 20-30 nm, and a length of 1-5 μm were mixed in a high-energy planetary ball mill under an argon atmosphere. The mechanical alloying conditions are as follows: 1 and 2 wt% MWCNT, three BPRs of 10:1, 15:1, and 20:1, and three alloying times of 15, 30, and 60 min. Field Emission Scanning Electron Microscopy (FESEM) model MIRA3-FEG-SEM made by TESCAN Co. (Czech Republic) was used to analyze the morphology of the powders. The size distributions of the powders were quantified using a laser particle size analyzer (FRITSCH Co., model 'ANALYSETTE 22 Nano Tec'). X-ray diffraction spectroscope (XRD) model D5000 made by Siemens was used to study intermetallic compounds. The high density of crystal defects produced by mechanical milling increases the work hardening of the powder particles. Due to severe plastic deformation and continuous fracture, the crystal dimensions are reduced to be recognizable by the X-ray diffraction peaks [17]. Williamson and Hall identified the grain size and in-lattice strain as the reason for X-ray diffraction peaks. Hence, according to Eq. (1), the grain size was determined by Williamson and Hall's method.

$$\beta \cos\theta = 4\varepsilon \sin\theta + \frac{k\lambda}{D} \qquad (1)$$

where D is the grain size, β is the peak width (in radians), θ is the angle at which the radiant beam strikes the atomic plane (in radians), ε is the relative change in distance between the crystal plates or the lattice strain, k is the Scherr constant (usually between 0.9-1), and λ is the radiated X-ray wavelength (in angstroms).

3. Results and discussion

Figure 2 shows the morphological changes of the chip after milling for 3 h with a BPR of 10:1 and 20:1. As the BPR increases, the chip morphology turns into a plate-like morphology. The sharp edges become smoother, and more welded particles became to appear. The higher the BPR, the higher the number of collisions between the balls, the powders, and the container. It leads to breaking, cold-welding, agglomerating, and again breaking the particles. These collisions speed up the milling process. In conclusion, increasing the BPR causes more chips to be broken. Figure 2 also shows the curves of the particle size distribution. D_{50} represents the minimum diameter equivalent to 50% of the particles, and D_{90}-D_{10} indicates the particle size distribution range. By increasing the BPR, D_{50} decreases from 36 μm to 6 μm, and the range of D_{90}-D_{10} encloses from 25 μm to 17 μm. Therefore, a powder with smaller particle size and a more limited distribution range is achieved.

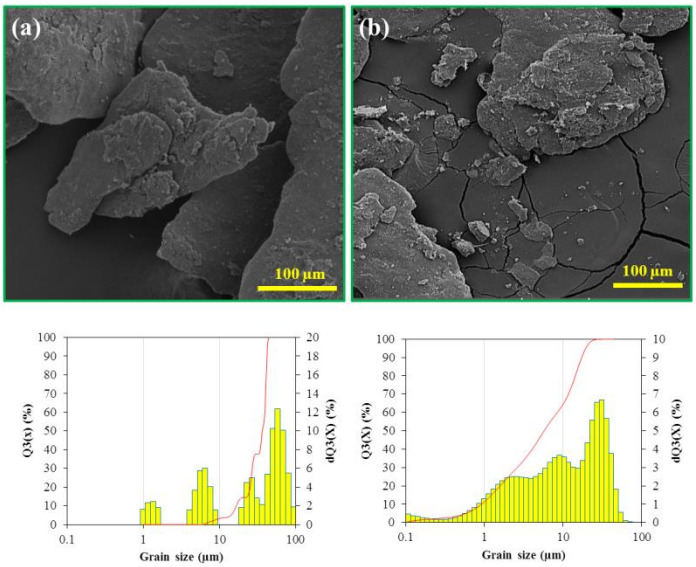

Fig. 2. The chips morphological changes and related distribution curves after milling for 3 h and a BPR of (a) 10:1 and (b) 20:1.

Figure 3 shows the morphological changes of the chip with a BPR of 15:1 after milling for 1 and 5 h. Changing the morphology of the chips in addition to agglomerating them is predicted by increasing milling time, both of which are mainly due to cold welding. At a short milling time, the particle agglomeration is not very noticeable, indicating the predominant role of the fracture and deformation process in the milling mechanism. According to the particle size distribution curves, the D_{50} increases

from 32 µm to 40 µm by increasing the milling time. It indicates that cold welding is predominant during mechanical milling. The lower D_{50} indicates the breakage of the particles. At the same time, the D_{90}-D_{10} increases from 21 to 30 µm. Therefore, at a short milling time, the finer particles with a limited size distribution are achieved because of the priority of the fracture process compared to the cold welding.

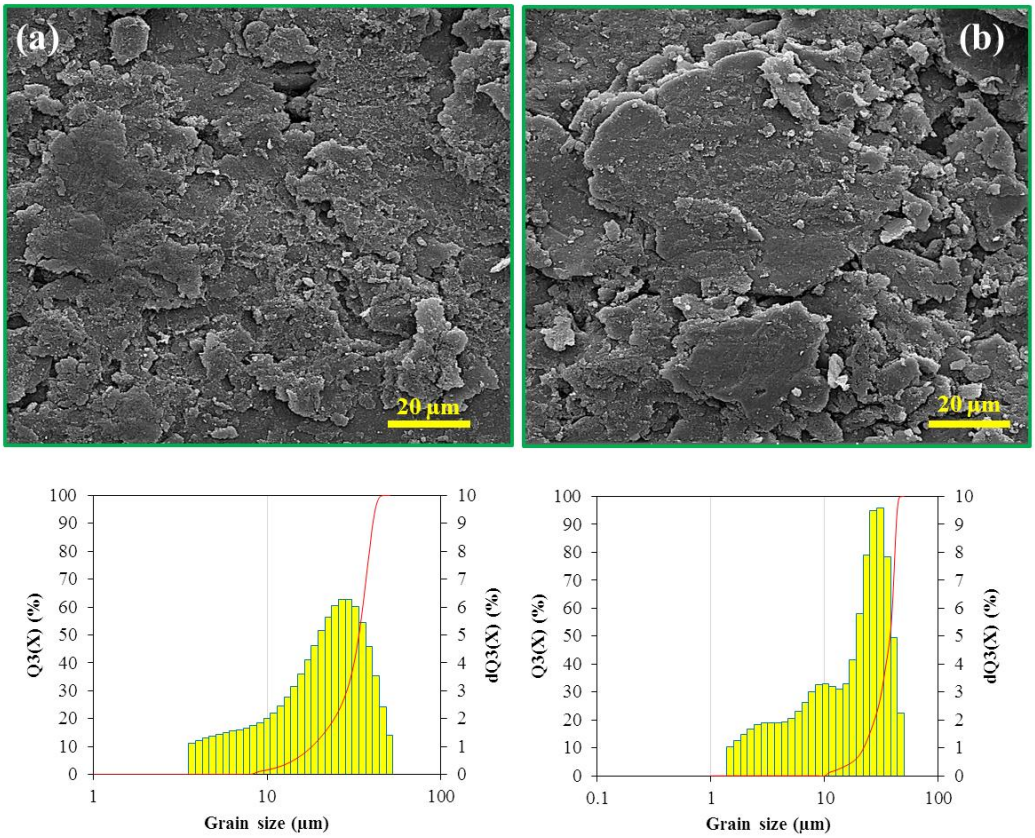

Fig. 3. The morphological changes of the chips and related distribution curves and a BPR of 15:1 after milling for (a) 1 h and (b) 5 h.

Figures 4a and b show the FESEM images of 5h-milled chips with a BPR of 10:1 and 1h-milled with a BPR of 20:1, respectively. A lower milling time with a higher BPR results in more broken chips. As the BPR increases and the milling time decreases, the D50-value decreases from 7 µm to 5.3 µm, and the particle size distribution encloses from 13.4 µm to 11.5 µm. Powders with a limited size distribution are less prone to segregation. The optimal particle size distribution can vary depending on the process conditions and the method used. There is a preference for powders with a limited size distribution over single-size or widely distributed ones due to their higher sintering potential and microstructural control [18]. These results have a good agreement with the research results conducted by Fogagnolo et al. [17].

Homogeneous distribution of the reinforcing phase in the metallic matrix is required to demonstrate the superior performance of the composite material so that the more uniform the dispersion, the better the composite properties. In this study, the alloying process and its duration determine the effective dispersion of the MWCNTs in the Al7075 alloy powder. The powder obtained from the mechanical milling for 1 h and with a BPR of 20:1 was used as an optimal combination for mechanical alloying.

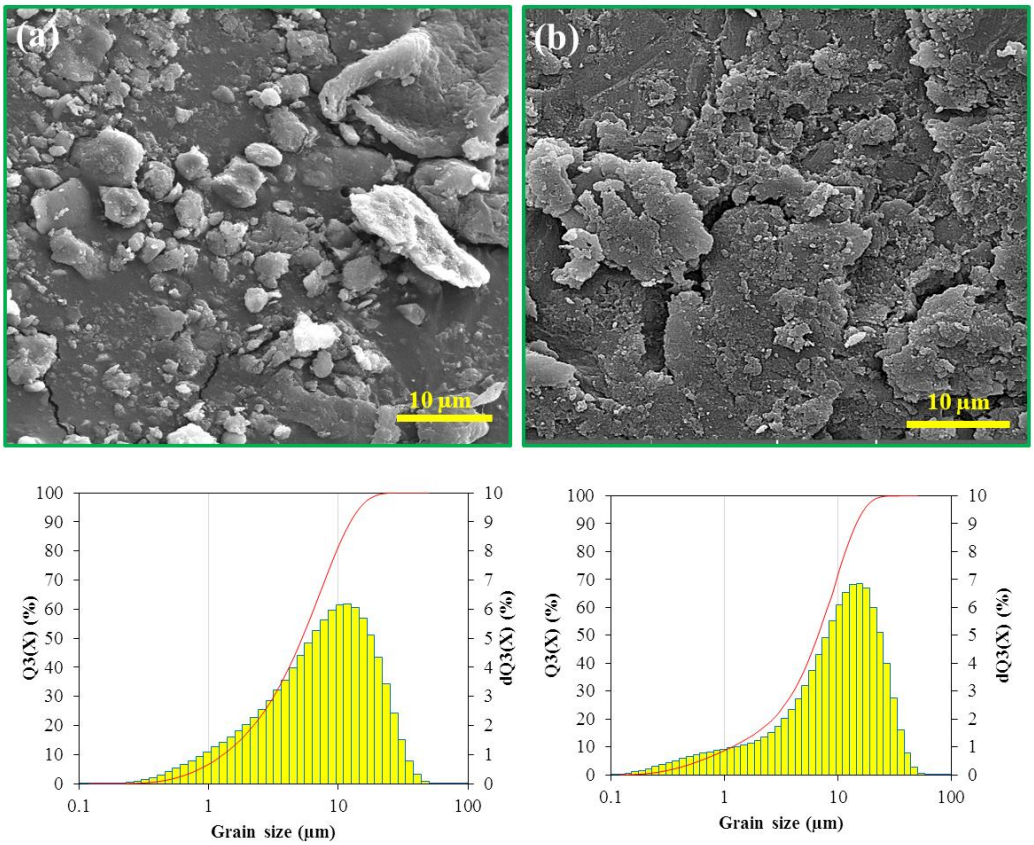

Fig. 4. The FESEM images and related distribution curves of the chips milled for (a) 5 h and a BPR of 10:1 and (b) 1 h and a BPR of 20:1.

Figure 5 shows the FESEM images of the Al7075-MWCNTs composite powders with 0, 1, and 2 wt% of reinforcing particles mechanically alloyed for 30 min with a BPR of 15:1. As we know, a mechanical mill affects particle size via two different mechanisms of cold welding and particle fracture. Figures 5a and b show that the particle size of the Al7075 containing 1wt% MWCNT composite powder is smaller than that of the Al7075 alloy powder simultaneously, i.e., the addition of the reinforcing particles reduces particle size. Furthermore, the size reduction rate is more distinguished in 2wt% MWCNT compared to 1wt% MWCNT. Therefore, it can be concluded that reinforcements have a significant impact on the morphology of the powders. The increase of the MWCNTs concentration accelerates the alloying process, causes fracture of more particles, and acts as a process control agent. The PCAs are ordinary organic compounds that act as surfactant agents. They are adsorbed onto the surface of the powder particles and minimize contact between particles, thereby inhibiting agglomeration. Here, the MWCNTs avoid cold welding and bonding between the powder particles and the balls and the agglomeration of powders during milling. So, they act as a process control agent. It also reduces cold welding during the alloying process, and smaller particles are obtained for the same alloying time. According to the results presented, adding reinforcements has a positive effect on the alloying process. The schematic of how the reinforcing particles of MWCNTs and the aluminum matrix combine in the mechanical alloying process is shown in Figure 6. Given the research results conducted by Wu et al., the particle size of the MWCNT-reinforced composite powder is smaller than the reference powder [18]. Uriza et al. [11] stated that increasing the reinforcing content is a way to reduce excessive particle welding during the milling process, which produces smaller particles at the same milling time. Increasing the MWCNT content and the collision of particles inside the mill leads to the formation of a hard surface on the particles, which increases their fragility and decreases the particle size. Therefore, in addition to the fracture-welding-fracture cycle in the mechanical milling process, this hard surface interferes with the cycle and becomes harder each time during combination with the aluminum particles. As the MWCNT content increases, this effect reaches a maximum value, and the fracture of the harder and smaller particles prevails. Figure 6 illustrates the mechanical alloying mechanism of the Al7075-MWCNT composite.

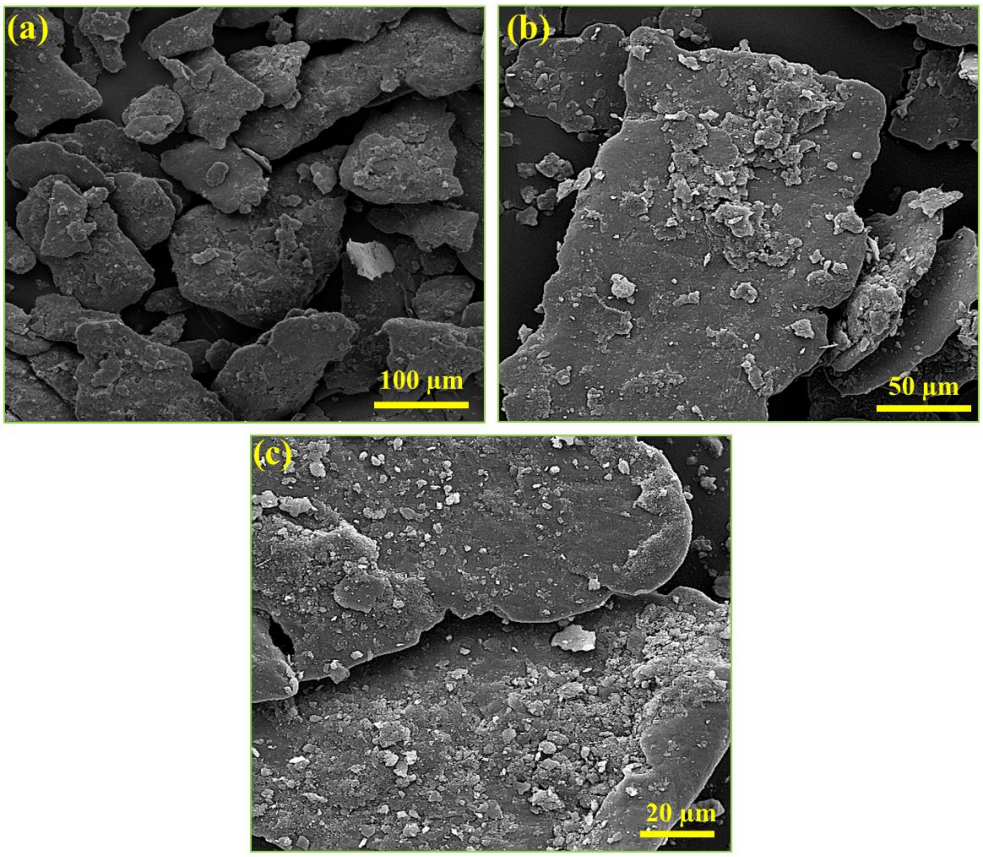

Fig. 5. The FESEM images of the Al7075-MWCNTs composite powders with (a) 0, (b) 1, and (c) 2 wt% reinforcement mechanically alloyed for 30 min and a BPR of 15:1.

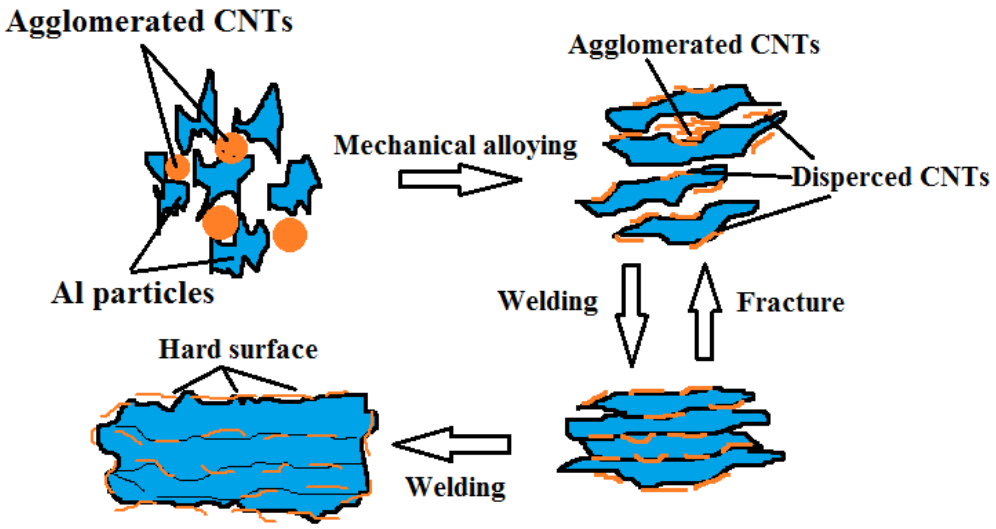

Fig. 6. Schematic of mechanical alloying mechanism of Al7075-MWCNT composite.

Figure 7 presents the FESEM images of Al7075-MWCNTs composite powder after alloying for 60 min and a BPR of 10:1. Figure 7a shows the morphology of a composite powder with 1 wt%-MWCNTs. A plate-to-globular change in the morphology of the particles and more fracture of particles are observable after mechanical alloying. MWCNTs were distributed in the matrix so that some of them are deeply embedded inside the alloy, and partial clusters are seen. By increasing the reinforcements up to 2 wt% (see Figure 7b), the MWCNTs observed on the composite surface gradually decrease and embed inside the aluminum alloy particles. The morphology of clusters of the MWCNTs is not changed.

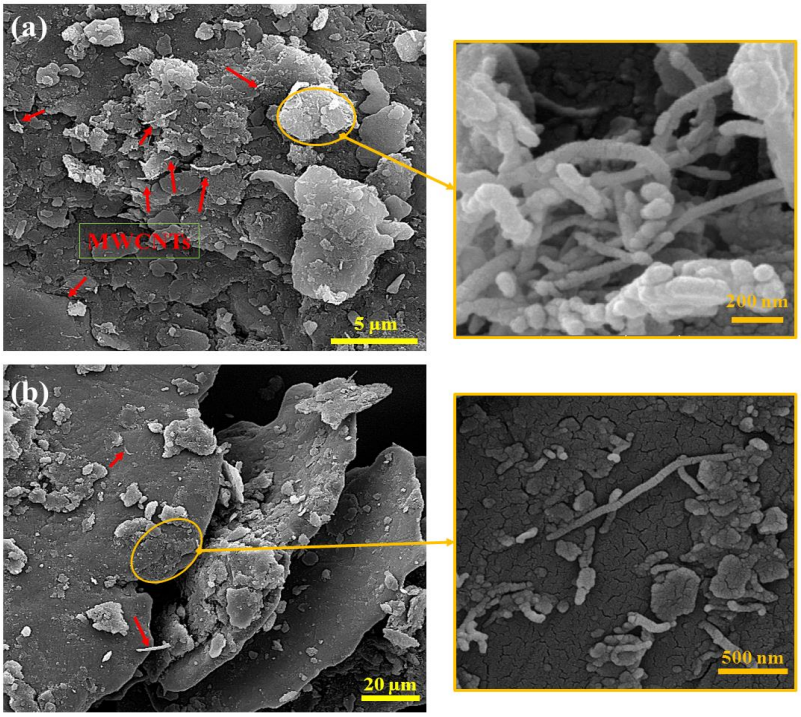

Fig. 7. The FESEM images of the Al7075-MWCNT composite powder mechanically alloyed for 60 min, a BPR of 10:1, and a reinforcement content of (a) 1% and (b) 2%.

Figure 8 shows the FESEM images of the Al7075-MWCNTs composite powder after an alloying time of 15 min and a BPR of 20:1. Based on Figure 8a, the MWCNTs are rarely found on the surface; this is attributable to the lower percentage of reinforcements or the higher BPR at a short alloying time. This condition leads to uniformly dispersing and deeply embedding the MWCNTs inside the alloy. Of course, by increasing the BPR during the mechanical alloying process, some breakage is observed in the MWCNTs due to the higher energy of the planetary ball mill. Figure 8b shows the uniform distribution of the MWCNTs on the surface of the composite powder in which their clusters are crushed and bonded to the surface of the aluminum particles. It is evident that uniform dispersion of reinforcements is achieved by increasing their content in a short alloying time.

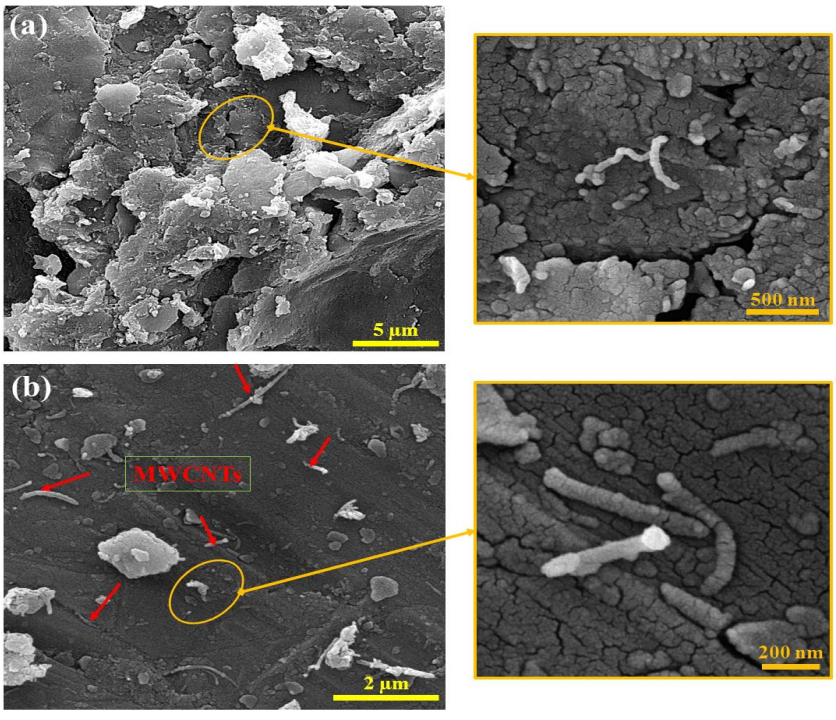

Fig. 8. The FESEM images of the Al7075-MWCNT composite powder mechanically alloyed for 15 min, a BPR of 20:1, and a reinforcement content of (a) 1% and (b) 2%.

Figure 9 presents the FESEM images of the Al7075-2%-MWCNTs composite powder with a BPR of 10:1 and an alloying time of 15 min. It can be seen that in MWCNTs-rich composite powder made with a low BPR and alloying time, the accumulation of nanotubes on the particle surface prevents the metal particles from bonding to each other. In this case, two types of bonds (1) Al7075 alloy with MWCNTs and (2) MWCNTs with MWCNTs are formed. The bond between the nanotubes is fragile and breakable under the load applied [19]. Further accumulation of the MWCNTs in a short alloying time leads to agglomerating the particles and adversely affects the homogeneity of the composite powders [20, 21]. In other investigations, the mechanical alloying process has successfully dispersed MWCNTs [19, 20]. In the research conducted by Al-Aqeeli [20], Yarahmadii et al. [19], increasing the content of reinforcements results in agglomeration when the milling time is short. In order to study the formation of the composite and the distribution of the reinforcement phase, EDS-map was prepared from Al7075-2% MWCNT powder with a BPR of 10:1 and alloying time of 15 minutes which is shown in Figure 9. To better understand the distribution of the reinforcements, a carbon element map was prepared as a representative of the MWCNT phase. It is observed that the carbon element is dispersed in the aluminum background, and a composite powder is formed.

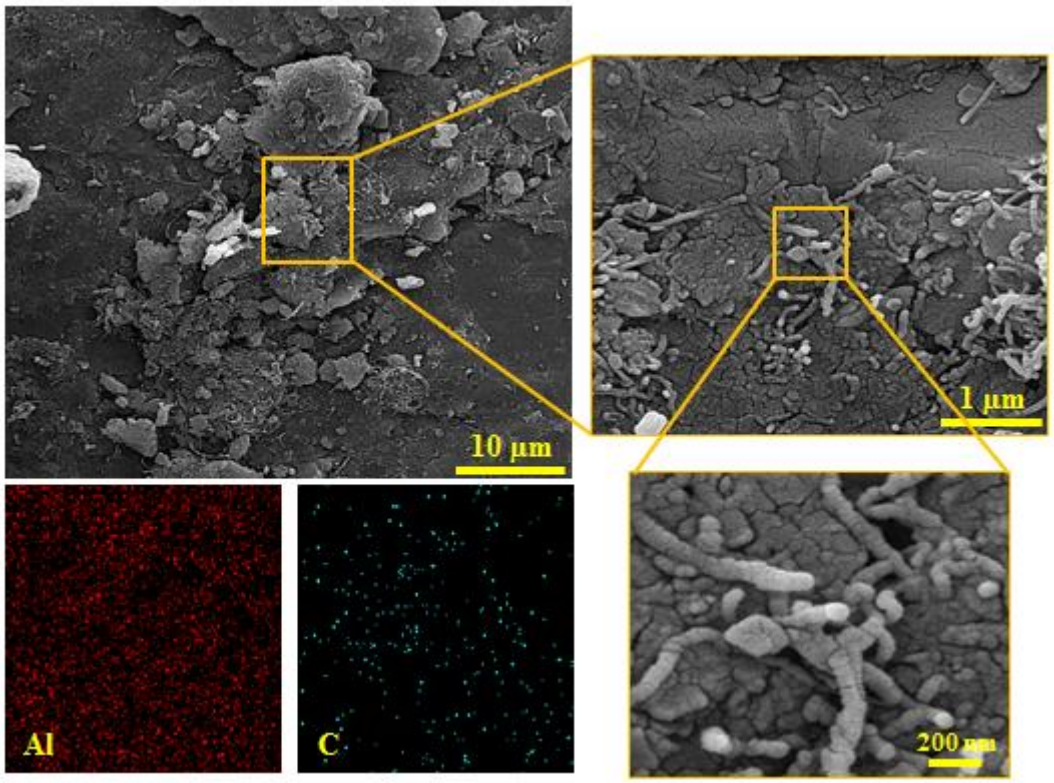

Fig. 9. The FESEM images of the Al7075-2% MWCNTs composite powder with a BPR of 10:1 and an alloying time of 15 min along with the EDS-map

Figure 10 shows the X-ray diffraction (XRD) spectroscopy analysis results for Al7075 alloy with 0, 1, and 2 wt% reinforcement. According to Figure 10b, the carbon-related peaks are tiny due to the low content of MWCNTs (1%), but these peaks can be seen by increasing the percentage of the MWCNTs, as shown in Figure 10c. Due to the large amount of Mg and Zn elements in the Al7075 alloy and the strong tendency of the alloy to combine with these elements, MgZn created during the alloying process is observed among all phases. In a study conducted by Zhang et al. [22], $MgZn_2$ was also observed during a tempering process in the hot pressing process of the Al7075 alloy. The difference in the thermal expansion coefficients between the MWCNTs and the background Al7075 alloy increases the deposition of $MgZn_2$ and the bonds between the MWCNTs and aluminum. The $MgZn_2$ phase has a good relationship with the aluminum matrix and helps to increase the surface bond. It should be noted that in Figs. 10b and c, the purpose is to show the appearance of the carbon peaks, and the peaks corresponding to the Al and MgZn phases are not shown for better comparison.

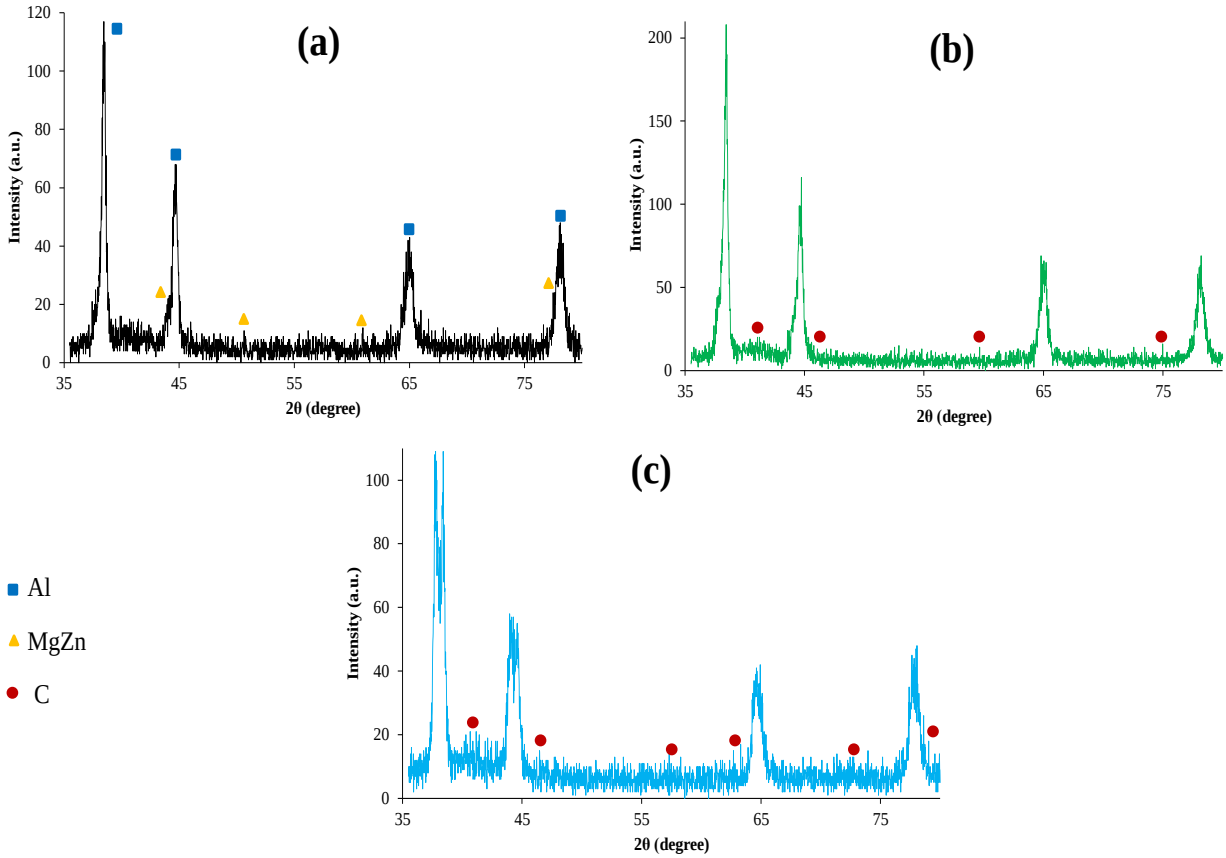

Fig. 10. The XRD analysis of the Al7075-MWCNT powder containing (a) 0, (b) 1, and (c) 2 wt% reinforcement (alloying time: 60 min, BPR: 10:1).

The morphological changes influence the intensity and width of the X-ray diffraction peaks. For example, when the grain size decreases, the width of the peak increases while its intensity decreases. Moreover, the intensity of some peaks increases and some others decreases by the preferential orientation of the grains. Using the data extracted from the XRD pattern and Xpert High Score software, the $\beta cos\theta$ diagram was plotted in terms of $sin\theta$ as shown in Figure 11a. According to the Williamson-Hall model, the grain size is calculated by the width obtained from the line's origin. The grain size is extracted from the intersection of the graph with the Y-axis shown in Figure 11a. Based on the results shown in Figure 11b, the grain size is reduced by adding the reinforcements to the Al7075 alloy. After alloying for 60 min, the grain size of the Al7075 alloy with 0, 1, and 2 wt% MWCNTs are equal to 37.4, 32.2, and 29.4 nm, respectively. By comparing the X-ray diffraction pattern of these samples, it is clear that by increasing MWCNTs, the peaks of the reinforcements become wider and have a larger peak width, indicating a decrease in the grain size. Compared to the Al7075 alloy powder without the reinforcements, the grain size of the Al7075 containing 2wt% MWCNTs powders at the same alloying time and BPR are reduced by about 22%. Therefore, based on the results obtained from the FESEM images, the reinforcements as a process agent accelerate the alloying process and reduce the grain size.

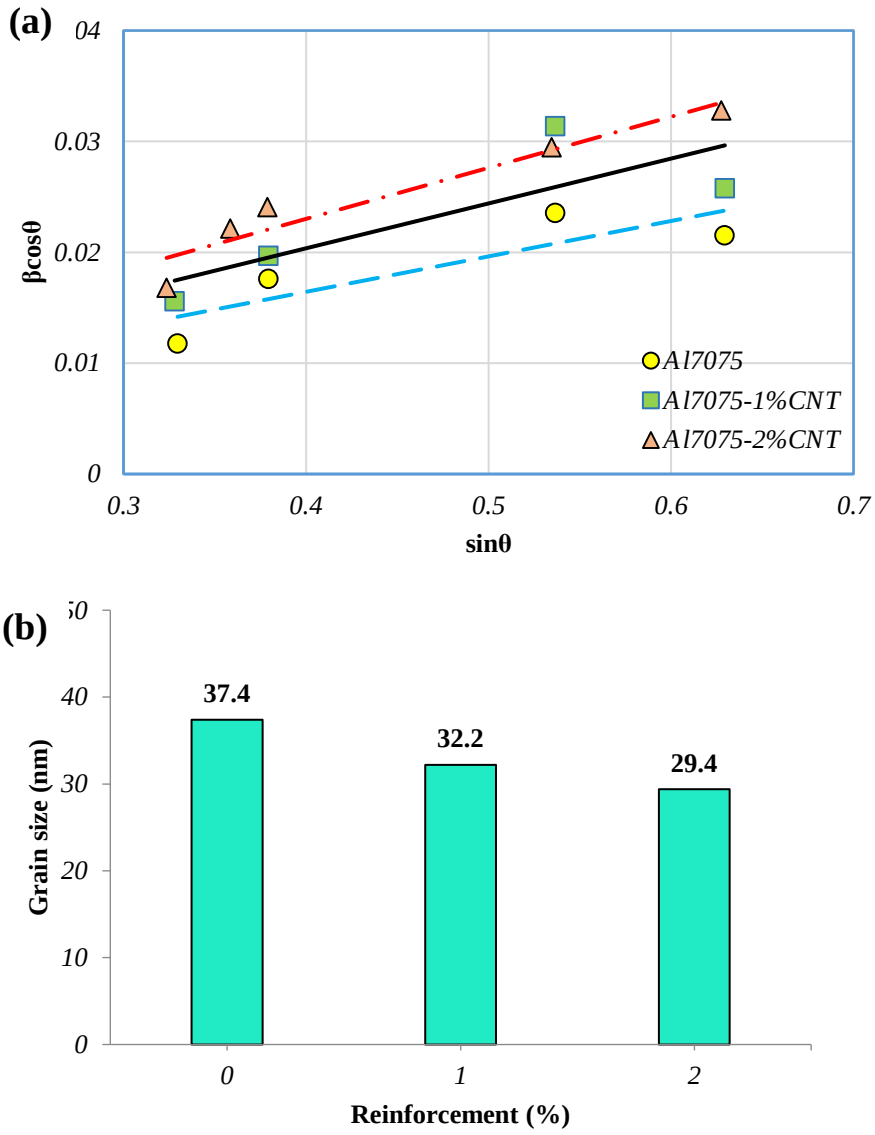

Fig. 11. (a) The Williamson-Hall diagram and (b) the obtained grain size (alloying time: 60 min, BPR: 10:1).

4. Conclusions

In this research, the Al7075-MWCNT composite powder was prepared by the mechanical alloying process in a high-energy planetary ball mill with different weight percentages of reinforcements, milling time, and BPR. The composites morphology was studied, and the following results were obtained:

- In mechanical milling, by decreasing the milling time in a constant BPR, the finer particles with a limited size distribution are achieved because of the priority of the fracture process compared to the cold welding one. As the BPR increases and the milling time decreases simultaneously, the powders with a limited size distribution are achieved.
- In the mechanical alloying process, the reinforcements had a significant impact on the morphology of the powders. By increasing the MWCNTs, the formation of harder surfaces on the particles accelerates; it should be mentioned that their fragility increases, the cold welding decreases, and smaller particles are obtained.
- A uniform dispersion of the reinforcement (2 wt%) inside the metallic background of the Al7075 alloy is achieved after alloying for 15 and 30 min and a BPR of 20:1. In addition, adding a large amount of the MWCNTs (2 wt%) at a short alloying time (15 min) and a lower BPR (10:1) adversely affect the homogeneity of the alloy and leads to agglomeration.
- There is no new peak in the XRD diffraction pattern for the Al7075 aluminum alloy powder. In the X-ray diffraction pattern of the Al7075 containing 1 wt% MWCNT, the carbon peaks are specified in small quantities. For Al7075 containing 2 wt% MWCNT, the carbon peak is more visible compared

to the 1 wt% MWCNT. The MgZn phase peaks are also evident in the X-ray diffraction patterns; this is due to the combination of the Mg and Zn elements present in the Al7075 alloy during the alloying process.

- The result concerning the reduced particle size, which is due to the addition of the MWCNTs, is confirmed based on the data obtained from the XRD pattern and their analysis with the Williamson-Hall model.

References

[1] Samal P., Vundavilli P.R., Meher A., Mahapatra M.M., 2020, "Recent progress in aluminum metal matrix composites: A review on processing, mechanical and wear properties," J Manuf Process, 59, pp. 131-152.

[2] Prajapati P., Chaira D., 2019, "Fabrication and characterization of Cu–B4C Metal matrix composite by powder metallurgy: effect of B 4 C on Microstructure, mechanical properties and electrical conductivity," Trans Indian Inst Met, 72(3), pp. 673-684.

[3] Bakkar S., Wall M., Ku N., Berman D., Aouadi S.M., Brennan R.E., et al., 2021, "Al/Al_2O_3 metal matrix composites produced using magnetic field-assisted freeze-casting of porous ceramic structures," J Mater Res, 36(10), pp. 2094-2106.

[4] Ashwath P., Xavior M.A., 2016, "Processing methods and property evaluation of Al_2O_3 and SiC reinforced metal matrix composites based on aluminium 2xxx alloys," J Mater Res, 31(9), pp. 1201-1219.

[5] shafqat Q.A., Rafi ud d., Shahzad M., Khan M., Mehmood S., Syed W.A., et al., 2019, "Mechanical, tribological, and electrochemical behavior of hybrid aluminum matrix composite containing boron carbide (B_4C) and graphene nanoplatelets," J Mater Res, 34(18), pp. 3116-3129.

[6] Liu G., Tao J., Li F., Bao R., Liu Y., Li C., et al., 2019, "Optimizing the interface bonding in Cu matrix composites by using functionalized carbon nanotubes and cold rolling," J Mater Res, 34(15), pp. 2600-2608.

[7] Kumar A., Banerjee U., Chowrasia M.K., Shekhar H., Banerjee M., 2019, "Effect of MWCNT Content on the structure and properties of spark plasma-sintered Iron-MWCNT composites synthesized by high-energy ball milling," J Mater Eng Perform, 28(5), pp. 2983-3000.

[8] Polat G., Canbolat I.E., Uzunoğlu A., Kotan H., 2021, "Effect of milling time, MWCNT content, and annealing temperature on microstructure and hardness of Fe/MWCNT nanocomposites synthesized by high-energy ball milling," Adv Powder Technol, 32(8), pp. 3107-3116.

[9] Bastwros M., Kim G.-Y., Zhu C., Zhang K., Wang S., Tang X., et al., 2014, "Effect of ball milling on graphene reinforced Al6061 composite fabricated by semi-solid sintering," Composites, Part B, 60(pp. 111-118.

[10] Shu R., Jiang X., Shao Z., Sun D., Zhu D., Luo Z., 2019, "Fabrication and mechanical properties of MWCNTs and graphene synergetically reinforced Cu–graphite matrix composites," Powder Technol, 349(pp. 59-69.

[11] Uriza-Vega E., Carreño-Gallardo C., López-Meléndez C., Cuadros-Lugo E., Pérez-Bustamante R., Ledezma-Sillas E., et al., 2019, "Mechanical Behavior of Multiwalled Carbon Nanotube Reinforced 7075 Aluminum Alloy Composites Prepared by Mechanical Milling and Hot Extrusion," Mater Res, 22(2), pp.

[12] Chen B., Kondoh K., Imai H., Umeda J., 2016, "Effect of initial state on dispersion evolution of carbon nanotubes in aluminium matrix composites during a high-energy ball milling process," Powder Metall, 59(3), pp. 216-222.

[13] Singh N., Shadangi Y., Goud G.S., Pandey V.K., Shivam V., Mukhopadhyay N.K., 2021, "Fabrication of MgAlSiCrFe Low-Density High-Entropy Alloy by Mechanical Alloying and Spark Plasma Sintering," Trans Indian Inst Met, pp.

[14] Aslibeiki B., Kameli P., 2020, "Structural and magnetic properties of Co/Al_2O_3 cermet synthesized by mechanical ball milling," Ceram Int, 46(12), pp. 20116-20121.

[15] Azimi A., Shokuhfar A., Nejadseyfi O., 2015, "Mechanically alloyed Al7075–TiC nanocomposite: Powder processing, consolidation and mechanical strength," Mater Des, 66(pp. 137-141.

[16] Wagih A., Fathy A., Kabeel A., 2018, "Optimum milling parameters for production of highly uniform metal-matrix nanocomposites with improved mechanical properties," Adv Powder Technol, 29(10), pp. 2527-2537.

[17] Fogagnolo J., Velasco F., Robert M., Torralba J., 2003, "Effect of mechanical alloying on the morphology, microstructure and properties of aluminium matrix composite powders," Mater Sci Eng, A, 342(1-2), pp. 131-143.

[18] Wu Y., Kim G.-Y., Russell A.M., 2012, "Effects of mechanical alloying on an Al6061–CNT composite fabricated by semi-solid powder processing," Mater Sci Eng, A, 538(pp. 164-172.

[19] Yarahmadii A., Rajabi M., Talafi Noghani M., Taghiabadi R., 2019, "Synthesis of aluminum-CNTs composites using double-pressing double-sintering method (DPDS)," J Nanostruct, 9(1), pp. 94-102.

[20] Al-Aqeeli N., 2013, "Processing of CNTs reinforced Al-based nanocomposites using different consolidation techniques," J Nanomater, 2013(pp.

[21] Wu Y., Kim G.-Y., Russell A.M., 2012, "Mechanical alloying of carbon nanotube and Al6061 powder for metal matrix composites," Mater Sci Eng, A, 532(pp. 558-566.

[22] Zhang H., Wang B., Zhang Y., Li Y., He J., Zhang Y., 2020, "Influence of aging treatment on the microstructure and mechanical properties of CNTs/7075 Al composites," J Alloys Compd, 814(pp. 152357.